3D reconstruction of the magnetic vector potential of magnetic nanoparticles using model based vector field electron tomography

Submitted in partial fulfillment of the requirements for

the degree of

Doctor of Philosophy

in

Materials Science and Engineering

Prabhat KC
B.A., Mathematics, Mercyhurst University

Carnegie Mellon University
Pittsburgh, PA

June, 2017

3D reconstruction of the magnetic vector potential of magnetic nanoparticles using model based vector field electron tomography

****

In the loving memory

of

बुवा ।

****

Acknowledgments

I would like to express my deep gratitude towards my advisor, Prof. De Graef. His support - financial and intellectual - and sheer passion to submerge in the crazy/mesmerizing/ bewildering/challenging/endless/... world of scientific research has been very instrumental in my very own pursuit of the doctoral degree.

I am also grateful to my muwa, my parents, my maternal uncle-aunt, and thulomom. I thank them for the unconditional love and affection they have bestowed me throughout my life. Their support and motivation throughout these past four years have been nothing short of amazing. At the same time, I feel indebted to sincerely apologize to them for long stretches of absence due to school work. Thanks to my longtime friend, Prakash.

My sincere thanks to the faculty, staff and students in MSE who have made this department a pleasant and a vibrant work place. Likewise, I would like to thank Aditya, Suhas, CD and Prof. Bauman whose guidance and suggestions have significantly shaped my research work. Furthermore, I would like to express my warm gratitude to my thesis committee members, Prof. Holm, Prof. Litster and Prof. Bouman. I thank them for their valuable feedbacks while formulating this thesis work.

This research work was funded through the U.S. Department of Energy grant (DE-FG02-01ER45893) for first three years which helped me develop the 2D MBIR approach. Likewise, NSF grant (DMR #1564550) supported the final development of the 3D MBIR approach in my fourth year.

My Ph.D. experience has been the most rewarding experience for me so far. Having said this, it would be a sheer injustice if I do not mention how indebted I feel to all my old and peripheral experiences that has led me to this point. It is a difficult task in itself to recount all those memories and show my gratitude all of you. Please forgive me if I forget to mention you name. However, do believe me, when I say that I wholeheartedly thank you. Nonetheless, here goes:

Babi di, I still vividly remember playing carom board with you in your old house. Thank you for being a role-model for rest of us in the family. Jyotsana di, the sheer love with which you used to put tika to me during the bhai-tika celebrations makes me smile whenever I think about Tihar. Rosna di, I am sure you will concur with me when I say

that we have lots and lots of memories together. But the one that will always standout, is the one when we accidentally damaged maiju's special flower and hid it in my backpack. Ankur dai, now that I am trying to write something about you, I cannot help but write about different phases you went through while we were growing-up. Some of which include Axel Rose phase, Hrithik roshan phase, Eminem phase. Ankush, what can I say about the breath of our friendship. All my memories of my stay in Nepal has you in it. It is hard to think of a weekend when we did not meet with each other or got scolded, together, by buwa. Pragal-Prayora, I love you guys from the bottom of my heart. For me, you two will forever be sweet little kids that I used to baby sit and take back and forth from school during my winter vacations.

My stay in the United States, thousands of miles away from friend and family in Nepal, would not have lasted this long without the support and acquaintance of teachers and friends at Mercyhurst. I want to take pause and want to acknowledge Dr. Griffiths for being an incredible advisor and constantly guiding me during my undergraduate days. I thank him for acquainting me about the world of mathematical research. I, truly, would have continued to remain in oblivion about research work had it not been for Dr. Griffiths and him recounting his own graduate life experiences.

Now then on a less serious note, let us move on to some of the fun part of Mercyhurst days. Su, you will agree with me when I say that the discourse of my life would not have been same, had it not been for your constant peer-pressure to play sand volleyball in the late mid-night hours. At times of despair, I recount the days when I used to indulge in the long tea conversations with Narayan, Karma, Irfan, and Satish. Also, I thank John and Ethan for being awesome roommates and inviting me to share meals during holidays. Likewise, thank you Prakash, Samantha, Laura, Tad for all of those late night excursions in Erie.

Moving on, I want to thank Vikram for helping me get situated in Pittsburgh and being a great friend over the years. Thank you Samikshya for giving me company through thick and thin times at CMU. I am sure we will have many more memories down the line. Furthermore, I am grateful to Paul and Matteus for allowing me to be part of their many eventful nights in Pittsburgh. A big thanks to Nepali community in Pittsburgh. This journey, truly, would not have been possible without the support of the Nepali clans.

6

Abstract

Lorentz TEM observations of magnetic nanoparticles contain information on the magnetic and electrostatic potentials of the sample. These potentials can be extracted from the electron wave phase shift by separating electrostatic and magnetic phase shifts, followed by 3D tomographic reconstructions. In past, Vector Field Electron Tomography (VFET) was utilized to perform the reconstruction. However, VFET is based on a conventional tomography method called filtered back-projection (FBP). Consequently, the VFET approach tends to produce inconsistencies that are prominent along the edges of the sample. We propose a model-based iterative reconstruction (MBIR) approach to improve the reconstruction of magnetic vector potential, $\mathbf{A}(\mathbf{r})$.

In the case of scalar tomography, the MBIR method is known to yield better reconstructions than the conventional FBP approach, due to the fact that MBIR can incorporate prior knowledge about the system to be reconstructed. For the same reason, we seek to use the MBIR approach to optimize vector field tomographic reconstructions via incorporation of prior knowledge. We combine a forward model for image formation in TEM experiments with a prior model to formulate the tomographic problem as a maximum a posteriori probability estimation problem (MAP). The MAP cost function is minimized iteratively to deduce the vector potential. A detailed study of reconstructions from simulated as well as experimental data sets is provided to establish the superiority of the MBIR approach over the VFET approach.

List of Publications Resulting from this Work

The following papers related to this thesis work have been submitted or are in preparation phase:

1. P. KC, K. A. Mohan, C. Phatak, C. A. Bouman, M. D. Graef. 3D Reconstruction of the Magnetic Vector Potential using Model Based Iterative Reconstruction. Ultramicroscopy, April 2017.

2. K. A. Mohan, P. KC, M. De Graef, C. A. Bouman, C. Phatak. Model-Based Iterative Reconstruction of Magnetization using Vector Field Electron Tomography. IEEE (2017, in preparation).

3. S. Singh, P. KC, M. De Graef. Model based iterative reconstruction for pole figure inversion. Acta Materialia (2017, in preparation).

4. P. KC, K. A. Mohan, C. A. Bouman, M. D. Graef. On Reconstruction of Magnetic Induction using Model Based Vector Tomography. Ultramicroscopy (2017, in preparation).

Contents

List of Figures

List of Acronyms

BP   Back Projection
FBP   Filtered Back Projection
SIRT   Simultaneous Iterative Reconstruction Technique
VFET   Vector Field Electron Tomography
MBIR   Model Based Iterative Reconstruction
RMSE   Root Mean Square Error
NRMSE   Normalized Root Mean Square Error
TIE   Transport-of-Intensity Equation (TIE)
FT   Fourier Transfer
FFT   Fast Fourier Transform
NP   Nanoparticle
MNP   Magnetic Nanoparticle
MAP   Maximum A posteriori Probability
MRF   Markov Random Field
ICD   Iterative Coordinate Descent
GGMRF   Generalized Gaussian Markov Random Field
q-GGMRF q-Generalized Gaussian Markov Random Field
ML   Maximum Likelihood
ANN   Artificial Neural Network
NN-FBP   Neural Network based Filtered Back Projection

Chapter 1

Introduction

1.1   Research motivation

The field of nanotechnology has garnered attention of scientists all over the world due to its ability to synthesize materials with control down to the atomistic size level. Most importantly, this attribute of nanotechnology has allowed researchers to manufacture devices far more superior than the ones synthesized from its bulk counterpart [4]. It has also allowed investigators to observe new phenomena and hence, develop devices with novel properties that could not have been envisioned a few of decades ago. LED TV (light-emitting diode television) is one particular example that stands out from our daily experience as a direct consequence of the nanotechnology. LED screens, employing the concept of quantum confinement, are brighter, clearer and more energy efficient than previously used LCD (liquid-crystal display) screens. In a similar manner, the principles of nanoscience have been incorporated in different types of materials resulting in application in diverse fields ranging from biomolecules, medicine, to electronics, and magnetic storage. One such class of nanomaterials that we are particularly interested in, is the magnetic nanoparticles (MNPs).

To begin with, nanomaterials have at-least one of its dimensions less than 100 nm [5]. At such ultra-small scale a whole host of new properties - such as superparamagnetism, high field reversibility, high saturation field, extra anisotropy contribution or shifted loops after cooling - are seen which are not shown in their bulk counterparts [6]. These novel

properties have carved out paths for the MNPs' applications in future technologies such as, localized drug delivery, optoelectronics, bit-patterned media etc. Also, there have been many "proof of principle" type studies where the MNPs have clearly been demonstrated as the alternative to materialize the aforementioned technologies [1]. However, there still remain a significant numbers of problems that need to be solved, in order to translate the theory based novel properties of the MNPs into fully functioning modern devices.

A particular field where the MNPs hold tremendous potential is in the area of biomedicine. For instance, researchers are looking to use MNPs coated with a lipid bilayer as a vehicle to deliver drugs to specific target cells or blood vessels. The transportation of the MNPs is induced by an external magnetic field [1]. A major advantage of this type of delivery medication over the conventional technique is that it can subdue the side effects of medical treatments by reducing the required dose [7]. Although there have been a significant number of successes of the MNPs driven drug treatments at the *in vitro* level (also bolstering the benefits of the localized medical treatment [8]), a successful *in vivo* targeted treatment using the MNPs still remains to be fully realized [1]. To this date the challenge has been the precise control of the motion of nanoparticles (NPs) such that the particles can overcome the opposing bodily fluid motions without forming toxic aggregates [9]. A similar type of complications surfaced when researchers were trying to locally kill tumorous cells by inducing hyperthermia with the aid of MNPs. In such applications, the investigators exploit the superparamagnetic property of MNPs and pass current around the vicinity of the NPs to induce heat, and thereby killing the cancerous cells [10, 11]. However, the magnetic field conditions that could be safely used with the human patient do not produce the desired heat effects so far [1].

The difficulty in translating the novel theoretical properties of NPs into fully functioning modern devices resides in the fact that a great deal of work still remains to be uncovered in terms of the techniques to characterize the ultra-small MNPs. For instance, the magnetic structure at the surface layer is different from the core of the NP that has strong effect in its properties [12, 13, 14]. Consequently, our calculations based on the prevalent techniques like Magnetic field Microscopy (MFM), which provides only the out of plane magnetic component analysis corresponding to the surface of NPs [15], may not provide a precise degree of external magnetic field needed to overcome the barriers

for domain wall motion in aforementioned applications like hyperthermia induced cancer treatment [1].

Likewise, the current technology of hard disk drive (HDD) based on granular media with perpendicular magnetic anisotropy is on the brink of reaching its limit, around 1000 Gbit/in^2 [15, 16]. Therefore, alternative technology such as bit patterned media (BPM) is being considered that is predicted to enable areal densities up to $20 - 300$ Tb/in^2 [17]. In this technology, nanopillars (nanodots) are proposed to store the information. These pillars have been shown to exhibit either vortex or flower state magnetic configuration. In addition, there have been evidences from measurements as well as micro-magnetic simulations that magnetization state changes from in-plane to out-of-plane and vice-versa as a function of the nanopillar's aspect ratio, how these pillars are arranged in an array and presence of external field. If we recall the history, the areal density increased from 1 Gbit/in^2 (IBM, December 1989) to 35.3 Gbit/in^2 (IBM, October 1999) to 610 Gbit/in^2 (Hitachi, July 2008) only because we were able to increase our understanding of the relation between thin film growth and processing the resulting microstructure via characterizing the microstructural properties of magnetic particles [18]. In a similar manner, decisive to the advent of bit-patterned media and other important nanotechnologies based application such as field emission guns, quantitative MFM, and photovoltaic devices is our ability to understand magneto-static interactions at nanoscale length [19, 20, 21, 22]. More specific, there is a necessity to spatially resolve 3D electromagnetic potentials in and around the NPs which will provide us valuable information on the chemical composition, electronic structure, magnetic field distribution and field emission process [23, 24]. Subsequently, with the aid of these information we will be able to pinpoint the cause of failure in the aforementioned applications. Now, if we glance over the prevalent techniques used for the magnetic characterization of the MNPs, we will find that it comprises of Vibrating Sample Magnetometry (VSM), Superconducting Quantum Interference Device (SQUID) magnetometry, Magnetic Force Microscopy (MFM), X-ray spectroscopy, Magneto-Optical Kerr Effect (MOKE), Spin-Polarized Scanning Tunneling Microscopy (SP-STM), X-ray Magnetic Circular Dichroism (XMCD) and Transmission Electron Microscopy (TEM). An important point to note here is that when it comes to 3D electromagnetic characterization, almost all have limitations of one form or the other. First, VSM and SQUID

magnetometry measure only the sample's net magnetization in the presence of an external magnetic field [25]. Second, even when some of the microscopy techniques provide the vectorial map of the magnetic field, the characterization pertains only to the spatial regions near the sample surface as in the case of the MFM technique. Third, some have limited spatial resolution. For instance, MOKE has a resolution close to 100 nm. Additionally, MOKE microscopy method gives either in-plane or out-of plane component of the magnetic field corresponding to the surface of the MNP [26]. In the remaining cases, like X-ray microspectroscopy method, the data acquired can only resolve the in-plane components of magnetization directly as the out-of-plane component is invisible in its experiments [27]. Finally, some also exhibit instrumentation and experimental difficulties. For instance, tip preparation and the separation of artifacts from the measurements in SP-STM continue to be great challenges [28]. In case of XMCD based characterization of non-uniform magnetic states, one needs to record contrast in several projection axes. In addition, the spatial resolution of magnetization texture deduced from the XMCD technique is limited by the fact that the lateral shift between two subsequent projections must not exceed the domain size. Accordingly, one can reconstruct feature size of only 40 nm with projection step size of 4° [29, 30].

An exception to the limitations of all the aforementioned characterization techniques is the TEM analysis. TEM in combination with computational and numerical reconstruction procedure is capable of quantitatively characterizing the magnetic vector potential in and around the MNPs [31]. Moreover, the resolution can be as high as 1 nm [32]. Having said this, an important point to note here is that there are different modes to operate a TEM experiment. Two such modes, which are specifically suitable for the purpose of reconstruction, are electron holography and Lorentz modes [18]. Electron holography requires extra instrumentation in terms of incorporation of bi-prism in the path of the electron beam [33]. The micrographs acquired from the holography experiment can be used to reconstruct highly resolved electromagnetic potentials. However, such quantification corresponds mostly to the regions near to the edges and outside the sample [24]. On the contrary, Lorentz TEM offers information that can be used to reconstruct a highly resolved electromagnetic potentials in and around the sample with measurements obtained in just two tilt series (instead of several as in the case of XMCD). Consequently, we will

be using the Lorentz based TEM to deduce the magnetic vector potential for our research purpose.

As highlighted before, determination of the electromagnetic potentials consists of not only the TEM experimental protocol but also the numerical reconstruction procedure. In particular, tomography underpins the basis of our reconstruction technique. Initially, TEM based tomography was limited to just scalar reconstruction. The first example of TEM based reconstruction was published in 1968 to determine the structure of a biological macromolecule [32]. In subsequent years, tomographic methods for vectorial reconstruction of 2D and 3D fields were formalized. Accordingly, it became feasible to retrieve electromagnetic potentials of MNPs from the Lorentz TEM micrographs.

In a TEM experiment, the propagating electron deflects due to the electrostatic and the magnetic fields of the sample. The degree of the electron deflection is recorded in terms of phase shift information in each of the micrographs. Then the vectorial tomographic reconstruction allows us to map the phase shift information to the sample's electromagnetic potentials. This application of tomography to reconstruct the electromagnetic potentials in and around the nanoparticles is known as Vector Field Electron Tomography (VFET) [31]. Phatak et al. [34] employed the VFET framework to reconstruct magnetic vector potential of simulated as well as experimental MNPs. In case of simulated dataset, it was found that the reconstructed vector potential, quantitatively and quantitatively, diverged from its corresponding true values near the edge of NP sample. Similarly, the application of VFET approach on phase shift measurements, acquired from TEM experiments, determined vector potential that was plagued by ring artifacts, protrusions, blurriness and streak artifacts. The authors attributed to incomplete measurement set as the primary source of error in reconstruction. In addition, the VFET approach incorporates a mere filter based methodology called filtered back projection to perform reconstruction. Therefore, we propose to investigate further on the realms of the TEM based vector field reconstruction. The research will try to find ways to optimize the current VFET framework such that the new framework will compensate for the VFET method's limitations and subsequently, subdue the errors observed in the reconstruction. A successful completion of this research work will allow us to accurately quantify three dimensional field distribution in and around NPs; and so, this study can be pivotal to materialize the

aforementioned nanotechnologies.

1.2   Hypothesis

We hypothesize that the model based iterative VFET approach reconstructs magnetic vector potential in and around the edges of magnetic nanoparticles that agree more closely with the theoretical potential of the sample. The claim is made on the basis of the fact that the new model based method is centered on a statistical framework. The framework allows us to incorporate valuable prior information about the imaging system and the object being imaged. Similarly, it permits us to model experimental measurement in accordance to its true statistical distribution. Most importantly, the entire framework has an overhead of iterative procedure such that each iteration minimizes the error (until a convergence is met) to deduce an estimate that is far more superior (supported by root-mean-square type analysis) than the one derived from the old VFET approach.

1.3   Document Organization

Our discourse of magnetic vector characterization begins by laying out experimental protocols in Chapter 2. Here, we elucidate on how Lorentz based TEM micrographs capture information on electrostatic potential and magnetic vector potential of a NP sample. We show that the electromagnetic information is recorded in terms of the phase shift of the wave function of the exiting electron from the sample. Accordingly, the chapter describes on how the Transport-of-Intensity Equation (TIE) formalism is utilized to deduce the phase shift information from the modulus of the electron's wave function. Thus derived phase shift is the total phase shift and so, it has magnetic as well as electrostatic contributions. Hence, the chapter concludes with how time reversal symmetry is employed to separate the two phases.

In order to deduce the magnetic vector potential one has to perform tomographic reconstruction of the separated magnetic phase shift. For this reason, Chapter 3 is devoted to introduce the concept of tomography to the readers. We begin by delineating the basic underlying principles of tomography. Next, we show a computational implementation

of how a 2D scalar density can be resolved from its 1D projections. Subsequently, we conclude the chapter by extending the 2D tomographic reconstruction analysis to a case of 3D reconstruction and illustrate some of the results obtained from the 3D computational implementations.

Having established the principles underpinning the technique of tomography, we then move on to vector tomography in Chapter 4. We begin by outlining the theoretical framework of 2D vector reconstruction. Subsequently, we make use of the VFET approach to reconstruct the 3D magnetic vector potential in and around the sample. We, then, discuss on different shortcomings of the VFET approach in terms of how certain experimental restrictions such as, incomplete tilt range, protrusion of the reconstruction from two tilt series result in the impediment of proper reconstruction along the edges of the sample.

From Chapter 5 onwards, we investigate our initial claim of using the model based iterative reconstruction (MBIR) technique to ameliorate the underdetermined magnetic vector potential reconstructions obtained from the VFET approach. In particular, chapter 5 introduces Bayesian statistic that forms the basics of the MBIR method. The chapter begins by delineating the Bayes' theorem and its important aspects such as, prior modeling and likelihood modeling. Subsequently, we illustrate how a posterior probability is maximized to minimize a cost function. The advantage of minimization of the cost function is demonstrated by iteratively de-noising/de-blurring a corrupted image.

Adhering to the Bayesian framework established in chapter 5, we proceed to employ the same concept for the purpose of tomographic reconstruction in chapter 6. First, we formulate the Bayesian framework catered towards the tomographic reconstruction i.e. the MBIR approach. Again, the framework functions by minimizing a cost function, which translates into a reconstruction that is quantitatively a close approximation of the ground truth. Second, we illustrate some of the implementations using the MBIR methodology by reconstructing a 2D scalar object as well as the solenoid part of a 2D vector field. Here, we make direct comparisons of the results acquired from the new MBIR approach with the ones obtained from the conventional technique as described in chapters 3 and 4. We also quantify the level of improvements. Finally, employ the MBIR approach to reconstruct the vector potential of the simulated as well as the experimental datasets. We compare the results between the MBIR approach and the VFET approach to make a

final assessment of our starting hypothesis.

In the final Chapter 7, we give a brief account of how we seek to extend our MBIR approach for the future works. In particular, it provides an outline of how we can determine other important electromagnetism quantities such as the magnetic induction, $\mathbf{B}$, the magnetization, $\mathbf{M}$, and the demagnetization field, $\mathbf{H}$, of magnetic nanoparticles.

Chapter 2

Lorentz Microscopy and Electromagnetic Characterization

In the previous chapter, we established that the Transmission Electron Microscopy (TEM) technique is the best alternative among a vast array of microscopy tools to ascertain the electromagnetic information in and around magnetic nanoparticles (MNPs). Accordingly, we have devoted this chapter to elucidate how electromagnetic information can be deduced from Lorentz based TEM micrographs. Our methodology to determine electromagnetic potentials is, basically, based on the theory of image formation in the TEM. The details on this methodology are chronologically provided under headings below. But, before divulging any further, it has to be noted that our interpretation of the TEM analysis, here, primarily serves the purpose of deducing electromagnetic potentials and skips several key aspects of the TEM. Thus, for an in-depth understanding of the TEM technique, as a whole, we suggest readers to look into references [18], [35], [36] and [37].

2.1 Image formation in Lorentz microscopy

The first step in the process of computing electromagnetic potentials of MNPs consists of taking TEM images of the magnetic sample. TEM is a microscopy technique in which a beam of electrons is transmitted through an ultra-thin specimen of about $30 - 50$ nm
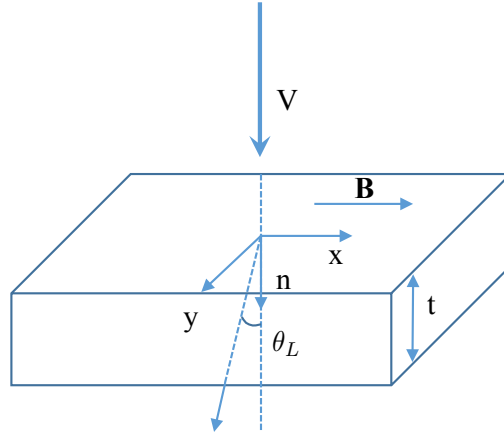
Figure 2.1: Schematic of the deflection of an incident electron beam [1].

thickness. The electron beam passing through the thin specimen experiences a Lorentz force, $\mathbf{F}_L$, due to the electrostatic field, $\mathbf{E}$, and the magnetic field, $\mathbf{B}$ of the magnetic specimen [33]. This force contributes to the deflection of the electron and is given by [38]:

$$\mathbf{F}_L = -e(\mathbf{E} + \mathbf{v} \times \mathbf{B}), \tag{2.1}$$

where $\mathbf{v}$ is the velocity of the propagating electron, e. An illustration of the effect of the Lorentz force on a propagating electron, with charge $-e$, is shown in figure 2.1. However, this description of Lorentz based TEM is classical in nature. A more robust explanation of beam-specimen interaction, useful for electromagnetic characterization, is provided in the realms of quantum mechanics. It states that the sample modifies both the amplitude and phase of the incident electron wave, and the resulting wave function becomes [18]:

$$\psi(\mathbf{r}_\perp) = a(\mathbf{r}_\perp)e^{i\varphi(\mathbf{r}_\perp)}, \tag{2.2}$$

where, $a(\mathbf{r}_\perp)$ is the amplitude and $\varphi(\mathbf{r}_\perp)$ is the phase of the wave function at the in plane position, $\mathbf{r}_\perp$. Phase across the plane will change (Phase shift) with respect to the change in magnetic induction of the sample across the plane. These phase shifts give rise to the contrast features in TEM images, and hence it becomes possible to discern magnetic domains across a plane.

Now, in order to define the phase term, $\varphi(\mathbf{r}_\perp)$, in eq. 2.2 we resort to a ground breaking

paper published in 1959 by Aharonov and Bohm [39]. In the paper, Aharonov and Bohm uncovered a profound result (commonly known as A-B effect) in the quantum domain that was not observed, earlier, in the realms of classical mechanics. In particular, they showed that the potentials of charged particles change even in the region where all fields (e.g.. electric, magnetic field) vanish. Thus alluring that the vector potential is even more fundamental than the magnetic field. They argued the phase shift imparted on an electron with relativistic wavelength, λ, in presence of the electrostatic potential, V, and the magnetic vector potential, $\mathbf{A}$, can be expressed as [18, 39]:

$$\varphi(\mathbf{r}_\perp) = \frac{\pi}{\lambda E_t} \int_L V(\mathbf{r}_\perp, z) dz - \frac{e}{\hbar} \int_L \mathbf{A}(\mathbf{r}_\perp, z) \cdot d\mathbf{r}, \tag{2.3}$$

where $\hbar = h/2\pi$, E_t is the total beam energy that depends on the acceleration voltage, and integrals are carried out in the beam direction, L. In eq. 2.3 the two terms, one encompassing the electrostatic potential and the other incorporating the magnetic potential, independently form electrostatic phase, φ_e, and magnetic phase, φ_m, such that:

$$\varphi_e(\mathbf{r}_\perp) = \frac{\pi}{\lambda E_t} \int_L V(\mathbf{r}_\perp, z) dz, \tag{2.4}$$

$$\varphi_m(\mathbf{r}_\perp) = -\frac{e}{\hbar} \int_L \mathbf{A}(\mathbf{r}_\perp, z) \cdot d\mathbf{r}. \tag{2.5}$$

Aside from the electron wave function, another important factor contributing to the image acquired from a TEM experiment is the microscope transfer function, $\mathcal{T}$. It modifies the electron wave in the back focal plane of the objective lens such that [33]:

$$\psi(\mathbf{q}_\perp) = \mathcal{F}[\psi(\mathbf{r}_\perp)]\mathcal{T}(\mathbf{q}_\perp), \tag{2.6}$$

where $\mathcal{F}$ denotes the Fourier transform operator and $\mathbf{q}_\perp$ represents the in-plane reciprocal space frequency vector. The microscope transfer function takes an account of various aspects of the microscope build. Overall, the transfer function is composed of three important factors, aperture function, $A(\mathbf{q}_\perp)$, phase transfer function, $e^{-i\chi(\mathbf{q}_\perp)}$, and damping envelope, $e^{-g(\mathbf{q}_\perp)}$, such that [33, 40]:

$$\mathcal{T}(\mathbf{q}_\perp) = A(\mathbf{q}_\perp)e^{-i\chi(\mathbf{q}_\perp)}e^{-g(\mathbf{q}_\perp)}. \tag{2.7}$$

Let us take a closer look at each of the variables used to define the transfer function: first, aperture function is used to describe the hole for the aperture. It is considered to be equal to 1 inside the aperture and 0 outside. Second, the phase transfer function modifies the phase of the electron wave and depends on the microscope defocus Δf. For a Lorentz based TEM analysis, phase transfer function's main contributing factor, $\chi(\mathbf{q}_\perp)$, can be expressed as [33]:

$$\chi(\mathbf{q}_\perp) \approx \pi\lambda\Delta f. \tag{2.8}$$

Third, the damping envelope is determined mostly by the stability of the lens current and the accelerating voltage. Still, the main contributing factor in the damping envelope is the beam divergence, θ_c, such that [33]:

$$g(\mathbf{q}_\perp) \approx \frac{(\pi\theta_c\Delta f)}{\ln 2}|\mathbf{q}|^2. \tag{2.9}$$

Hence from eqs. 2.7, 2.8, and 2.9, microscope transfer function for the Lorentz microscopy can be written as:

$$\mathcal{T}_L(\mathbf{q}_\perp) = A(|\mathbf{q}_\perp|)e^{-i\pi\lambda\Delta f}e^{-\left[\frac{(\pi\theta_c\Delta f)}{\ln 2}|\mathbf{q}|^2\right]}. \tag{2.10}$$

Finally, the intensity seen in the Lorentz images is the modulus-squared of the aberrated wave in the image plane such that:

$$I(\mathbf{r}_\perp) = |\mathcal{F}^{-1}[\psi(\mathbf{q}_\perp)]|^2 = |\psi(\mathbf{r}_\perp) \otimes \mathcal{T}_L(\mathbf{r}_\perp)|^2, \tag{2.11}$$

where $\otimes$ denotes convolution operation and $\mathcal{T}_L(\mathbf{r}_\perp)$ is the point spread function.

A schematic of the image formation from a Lorentz Microscopy experiment is depicted in figure 2.2. Based on the same figure as well as on eq. 2.2, it can be noted that phase is not a directly observable quantity in the Lorentz image. However, our electromagnetic characterization hinges upon the deduction of the phase to, ultimately, determine the sample's electromagnetic potentials. Consequently, we proceed to determine phase from the Lorentz image in next section.
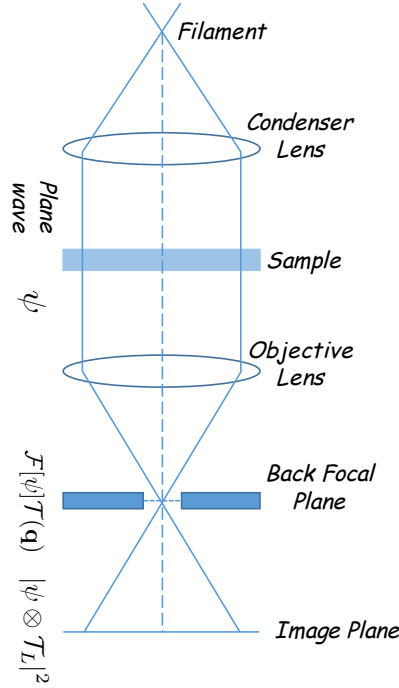
Figure 2.2: Schematic showing the formation of an image in a Lorentz based TEM [1].

2.2 Acquisition and separation of phase shift

The previous section establishes that the information on electromagnetic potentials of MNPs is encoded in the form of phase shifts in their Lorentz images. Now, we proceed to retrieve the phase information from the image intensity. This task is accomplished with the aid of the Transport-of-Intensity Equation (TIE) formalism. Paganin and Nugent [41] have defined the TIE as:

$$\nabla \cdot [I_\circ \nabla \varphi] = -\frac{2\pi}{\lambda} \frac{\partial I}{\partial z}. \tag{2.12}$$

The TIE formalism in eq. 2.12 relates the change in intensity of the image with defocus $\left(\frac{\partial I}{\partial z}\right)$ to the derivative of the phase shift, φ, of the sample. Here, $I_\circ$ denotes the intensity of the in-focus image, $\frac{2\pi}{\lambda}$ is the wave number and the z direction is parallel to the direction of electron propagation. Likewise, ∇ is the two dimensional differential operator that operates in the plane normal to the z axis. Then the phase shift can be written as [42]:

$$\varphi(\mathbf{r}_\perp, 0) = -\frac{2\pi}{\lambda}\nabla^{-1} \cdot \left(\frac{1}{I(\mathbf{r}_\perp, 0)}\left\{\nabla^{-1}\left[\frac{\partial I(\mathbf{r}_\perp, 0)}{\partial z}\right]\right\}\right). \tag{2.13}$$

The phase in eq. 2.13 is the total phase shift, φ, that consists of contributions from the magnetic phase, φ_m, as well as from the electrostatic phase, φ_e. Hence, in order to deduce the electrostatic potential and the magnetic potential separately, one must separate φ_m and φ_e. One of the approaches to separate the components of the total phase shift is to employ time symmetry property. Here, time reversal is accomplished by physically flipping the sample inside the microscope. More specifically, the technique comprises of taking two sets of Fresnel images of the sample; one in the upright configuration $[\varphi(t) = \varphi_m + \varphi_e]$ and the other in the flipped configuration $[\varphi(-t) = -\varphi_m + \varphi_e]$. Subsequently, the components of the phase shift can be separated as:

$$\varphi_e = \frac{1}{2}(\varphi(t) + \varphi(-t)), \tag{2.14}$$

$$\varphi_m = \frac{1}{2}(\varphi(t) - \varphi(-t)). \tag{2.15}$$

2.3 Determination of the electromagnetic potentials

Separation of the total phase in terms of its electrostatic phase and magnetic phase completes the experimental part and some of the pre-processing steps required to determine electromagnetic potentials. Henceforth, we assume that these pre-processing step to extract φ_m and φ_e from the TEM images have already been performed. This leads us to the second part of the characterization process i.e. numerical reconstruction. The tomographic reconstruction of the electrostatic phase yields the electrostatic potential and that of the magnetic phase yields the magnetic potential. Electrostatic potential is a scalar quantity and hence, it is determine by employing scalar tomography. On the contrary, determination of the magnetic vector potential requires implementation of vector tomography. A flow chart summarizing the entire process of the deduction of electromagnetic potentials is provided in figure 2.3.

sample

$\downarrow$ TEM

Image (I)

$\downarrow$ TIE

$\varphi = \varphi_e + \varphi_m$

phase / separation

φ_m φ_e

vector tomography $\downarrow$ $\downarrow$ scalar tomography

$\mathbf{A(r)}$ $V(\mathbf{r})$
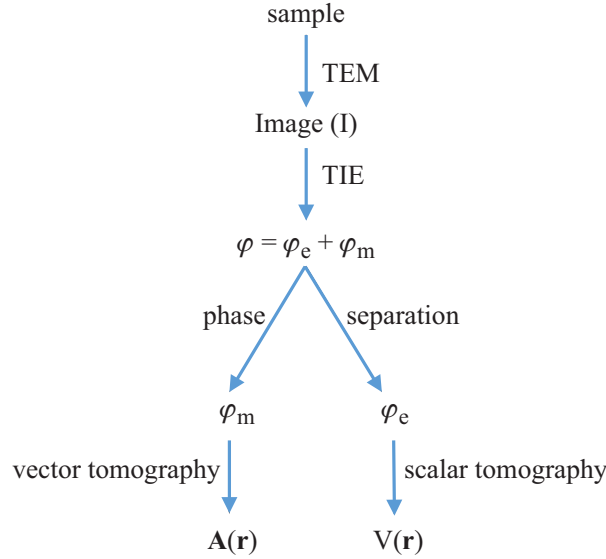
Figure 2.3: A flow chart illustrating the methodology to determine electromagnetic potentials of a magnetic nanoparticle sample.

Our research interest primarily lies on the numerical reconstruction. Accordingly, the rest of the documentation is devoted to decipher various aspects of reconstruction procedures to determine magnetic vector potential. It has to be pointed out that a great deal of work has been done in the field of scalar tomography due to its immense application in the medical CT technology. However, there have not been many attempts in the literature to reconstruct the 3D vector potential in and around the sample [34]. Consequently, we provide a detail outline on the formulation and implementation of vector tomography.

Just to give a quick outlook of the rest of the document, we begin by briefly introducing the general concept behind tomography. Then we proceed to the vector tomography and the current state-of-art to determine the magnetic vector potential i.e. Vector Field Electron Tomography (VFET) approach. Subsequently, we elucidate on how to seek to optimize the VFET approach by incorporating the Model Based Iterative Reconstruction (MBIR) methodology.

Chapter 3

Tomography

As per Webster's dictionary, the word "tomography" is composed of ancient greek words – *tomos*, meaning slice/section, and *graphio*, meaning to write. Likewise, Wikipedia defines tomography to be imaging by sections or sectioning through the use of penetrating wave. Conventionally speaking, one invariably associates the word tomography with the medical technique called CT - scan (computerized tomographic). The CT – scan methodology allows medical investigators to visualize the internal parts of human body such as, brain matters, skull, lungs or kidney without performing any invasive surgical operations. In the simplest possible manner of description of this procedure, it begins with a patient lying down in a CT - scanner. Next, X-rays are passed across a selected section of his/her body (under investigation) with the aid of a radiating source. Subsequently, detector, which lies opposite to the radiating source, detects the final intensity of the radiation after having penetrated through the human organelles. The process of emission and detection of the radiation is repeated at different angles of inclination. Finally, based on the change in the intensity of the radiation at various inclinations a map of the internal body parts is deduced.

In addition to the field of medicine, researchers from areas such as atmosphere science, plasma physics, archeology, etc have also extensively used the concept of tomography to perform 3D reconstruction from 2D projections. Similarly, our research work - Vector Field Electron Tomography (VFET) approach - aims to make use of tomography to reconstruct magnetic vector potential using 2D micrographs obtained from TEM experi-

ments. However, before divulging further into the matters pertaining to VFET in detail, the next few sections will, first, delineate the theoretical framework underpinning the notion of tomography. In the due course, a first hand glimpse of the computational implementations of tomography for 2D and 3D platforms will be depicted using algorithms such as, Back Projection (BP), Filter Back Projection (FBP), and Simultaneous Iterative Reconstruction Technique(SIRT).

3.1   2D Tomography

The tomography method, in true essence, was introduced to solve 3D problems using measurements that were 2D in nature [43]. In other words, tomography solves higher dimension problem. Exploiting this fundamental understanding of tomography, we, first, establish its mathematical framework for 2D reconstruction using 1D measurements. Subsequently, we extend the concepts of 2D tomographic reconstruction to resolve 3D tomographic problems.

3.1.1   Forward Projection

As mentioned earlier, the tomography technique hinges upon the acquisition of projections. Mathematically, for a 2D case (like images), projection is just the line integral across the plane. These line integrals can be obtained in a parallel beam fashion or in a cone beam pattern. However, for all practical purposes during the discourse of this tomography research work, it suffices that the projections are measured in parallel beam fashion. Henceforth, anytime acquisition of projection is mentioned, it is actually referring to parallel beam style of integration method. The projection profile, P_θ of an object, $f(x, y)$, across the $x - y$ plane at an inclination angle, θ, is depicted in figure 3.1a and can be expressed mathematically as:

$$P_\theta(t) = \int\limits_{-\infty}^{\infty} f(x, y)ds. \tag{3.1}$$

Note that, (t, s) is a new coordinate system that is inclined at an angle, θ, from the initial coordinate system, (x, y). Moreover, if R_θ represents counter-clockwise rotation
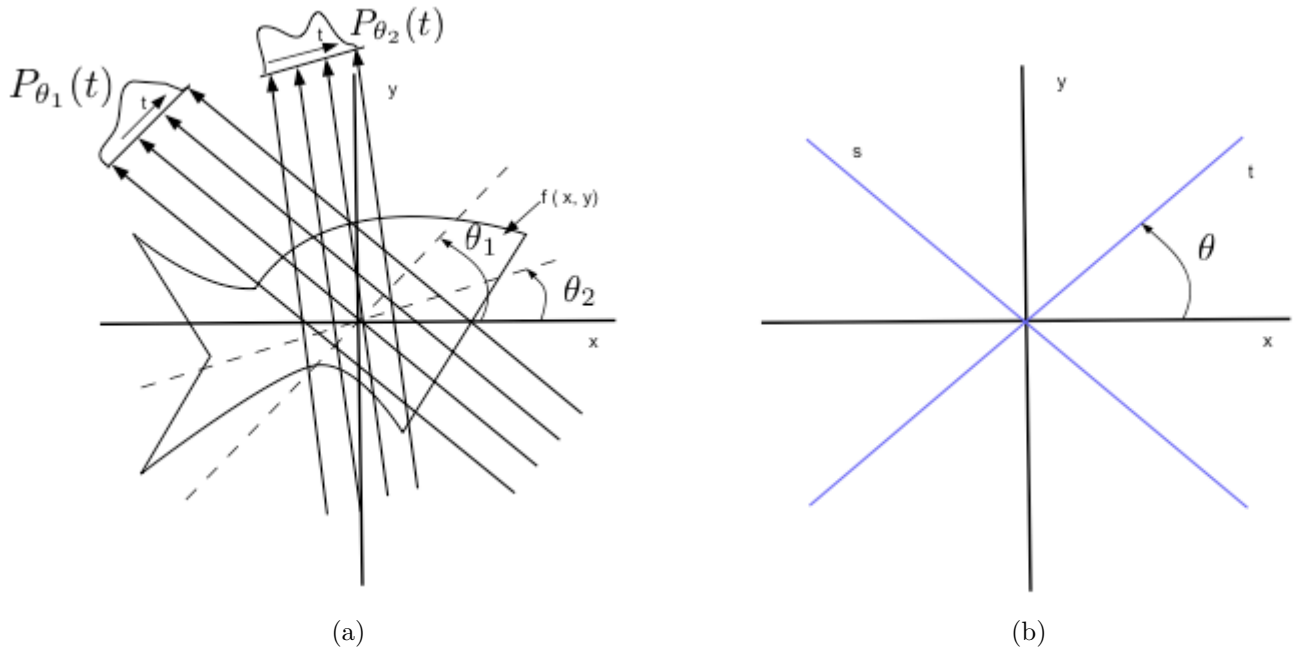
Figure 3.1: (a) Projection profiles at different inclination angles as the result of line integration across the $x-y$ plane. (b) New coordinate system (t, s) obtained after rotating the old coordinate system (x, y) by an angle θ.

matrix then the old coordinate system can be written in terms of the new coordinate system as follow:

$$\left[\begin{array}{c} x \\ y \end{array} \right] = R_\theta \left[\begin{array}{c} t \\ s \end{array} \right], \tag{3.2}$$

where, $R_\theta = \left[\begin{array}{cc} \cos(\theta) & -\sin(\theta) \\ \sin(\theta) & \cos(\theta) \end{array} \right]$

Now, the projection integral in (3.1) can be re-written as:

$$\begin{aligned} P_\theta(t) & = P(t, \theta) \\ & = \int_{-\infty}^{\infty} f(R_\theta \left[\begin{array}{c} t \\ s \end{array} \right]) ds \tag{3.3} \\ & = \int_{-\infty}^{\infty} f(t\cos(\theta) - s\sin(\theta), t\sin(\theta) + s\sin(\theta)) ds. \tag{3.4} \end{aligned}$$

The line integral obtained in expression (3.4) is also known as the radon transform of the function $f(x, y)$ at an angle θ. Moreover, it is the radon transform that provides the mathematical basis to model the projections or measurement attenuations from the experiments to implement the forward projection part of tomography. The final result of the execution of multiple radon transforms on the 2D Shepp-Logan phantom [44], shown in figure 3.2a, is depicted in figure 3.2b. It shows stacking of the consecutive projection results, forming so-called *sinogram*.

On the whole, every tomography experiment results in the acquisition of multiple projection measurements or sinogram. More importantly, notice that the measurements are no longer in the form of Cartesian coordinates. Instead, they are now in the polar form, (t, θ). Thus, retrieving the initial object from the measurements also involves returning back to the Cartesian plane. All the details of reconstruction from the measurements are discussed in the next subsection.

3.1.2 Backprojection

Implementation of backprojection enables one to reconstruct the initial object density from the projections. Likewise, an important implication of the backprojection operator is that, it transforms a function from polar to Cartesian coordinate. At the heart of the backprojection algorithm lies the Fourier Slice Theorem. Therefore, it becomes imperative to familiarize oneself with Fourier Slice Theorem in order to grasp the theoretical basis of backprojection algorithm. Fourier Slice Theorem argues and simultaneously goes to prove that the following two calculations are equivalent [45]:

- Taking a 2D function $f(x, y)$, projecting it onto a line, and evaluating the Fourier transform of that projection.

- Take that same function, but evaluate 2D Fourier transform first, and then slice it through its origin, which is parallel to the projection line.

The proof of Fourier Slice Theorem can be found elsewhere in Appendix A. Making use of this theorem, backprojection alorigthm can be formalized in the following manner:

$$
\begin{aligned}
f(x, y) &= \int_{-\infty}^{\infty}\int_{-\infty}^{\infty} F(u, v)e^{2\pi i(xu+yv)}dudv \\
&= \int_{0}^{\infty}\int_{0}^{2\pi} P(\rho, \theta)e^{2\pi i(x\rho\cos(\theta)+y\rho\sin(\theta))}\rho d\theta d\rho \qquad\qquad \text{from } Appendix A \\
&= \int_{0}^{2\pi}\left[\int_{0}^{\infty} P(\rho, \theta)e^{2\pi i\rho(x\cos(\theta)+y\sin(\theta))}\rho d\rho\right] d\theta \\
&= \int_{0}^{\pi}\left[\int_{0}^{\infty} P(\rho, \theta)e^{2\pi i\rho(x\cos(\theta)+y\sin(\theta))}\rho d\rho\right] d\theta + \int_{0}^{\pi}\left[\int_{0}^{\infty} P(\rho, \theta+\pi)e^{2\pi i\rho(x\cos(\theta+\pi)+y\sin(\theta+\pi))}\rho d\rho\right] d\theta,
\end{aligned}
$$

then using the following property in Fourier space

$$
P(\rho, \theta+\pi) = P(-\rho, \theta),
$$

we get,

$$
\begin{aligned}
f(x,y) &= \int_0^\pi \left[\int_0^\infty P(\rho,\theta)e^{2\pi i\rho(x\cos(\theta)+y\sin(\theta))}\rho d\rho \right] d\theta + \int_0^\pi \left[\int_0^\infty P(-\rho,\theta)e^{-2\pi i\rho(x\cos(\theta)+y\sin(\theta))}\rho d\rho \right] d\theta \\
&= \int_0^\pi \left[\int_0^\infty P(\rho,\theta)e^{2\pi i\rho(x\cos(\theta)+y\sin(\theta))}\rho d\rho \right] d\theta + \int_0^\pi \left[\int_{-\infty}^0 P(\rho,\theta)e^{2\pi i\rho(x\cos(\theta)+y\sin(\theta))}(-\rho)d\rho \right] d\theta \\
&= \int_0^\pi \left[\int_{-\infty}^\infty P(\rho,\theta)e^{2\pi i\rho(x\cos(\theta)+y\sin(\theta))}|\rho|d\rho \right] d\theta \\
&= \int_0^\pi b_\theta(x\cos(\theta)+y\sin(\theta))d\theta, \quad\quad\quad (3.5)
\end{aligned}
$$

where,

$$
b_\theta(x\cos(\theta)+y\sin(\theta)) = \int_{-\infty}^\infty P_\theta(\rho)e^{2\pi i\rho(x\cos(\theta)+y\sin(\theta))}|\rho|d\rho. \quad\quad (3.6)
$$

Taking, $|\rho| = 1$

$$
b_\theta(x\cos(\theta)+y\sin(\theta)) = \int_{-\infty}^\infty P_\theta(\rho)e^{2\pi i\rho(x\cos(\theta)+y\sin(\theta))}d\rho. \quad\quad (3.7)
$$

Notice that $b_\theta(.)$ is just the inverse Fourier transform of $P_\theta(.)$. The outside integral in eq. 3.5, "smears" the value $b_\theta(t)$ as a function of a set of points (x, y) such that $t = x\cos(\theta) + y\sin(\theta)$. Finally, backprojection completes with the addition of each of the smeared images generated in the angular range from 1° to 180°. An implementation of the backprojection algorithm on the projections acquired from the Shepp-Logan phantom for angles ranging 1° to 180° at a step size of 1° is depicted in figure 3.2c.

To sum up this section, the process of tomographic reconstruction begins with the acquisition of projection measurements from the experimental setup. These projections are mathematically modeled via radon transform expression as depicted in eq. 3.4. With this, it becomes evident that the problem of reconstruction exhibits itself as, how can one re-design 2D $f(x,y)$ while being provided with 1D values of P_θ. The problem is tackled by making use of Fourier Slice Theorem. Given the polar nature of P_θ, Fourier Slice Theorem is used to backproject these polar 1D values to Cartesian plane. Theoretically, it is possible to exactly reconfigure $f(x,y)$ from P_θ, as show by the expression in eq. 3.5.

(a)

(b)

(c)
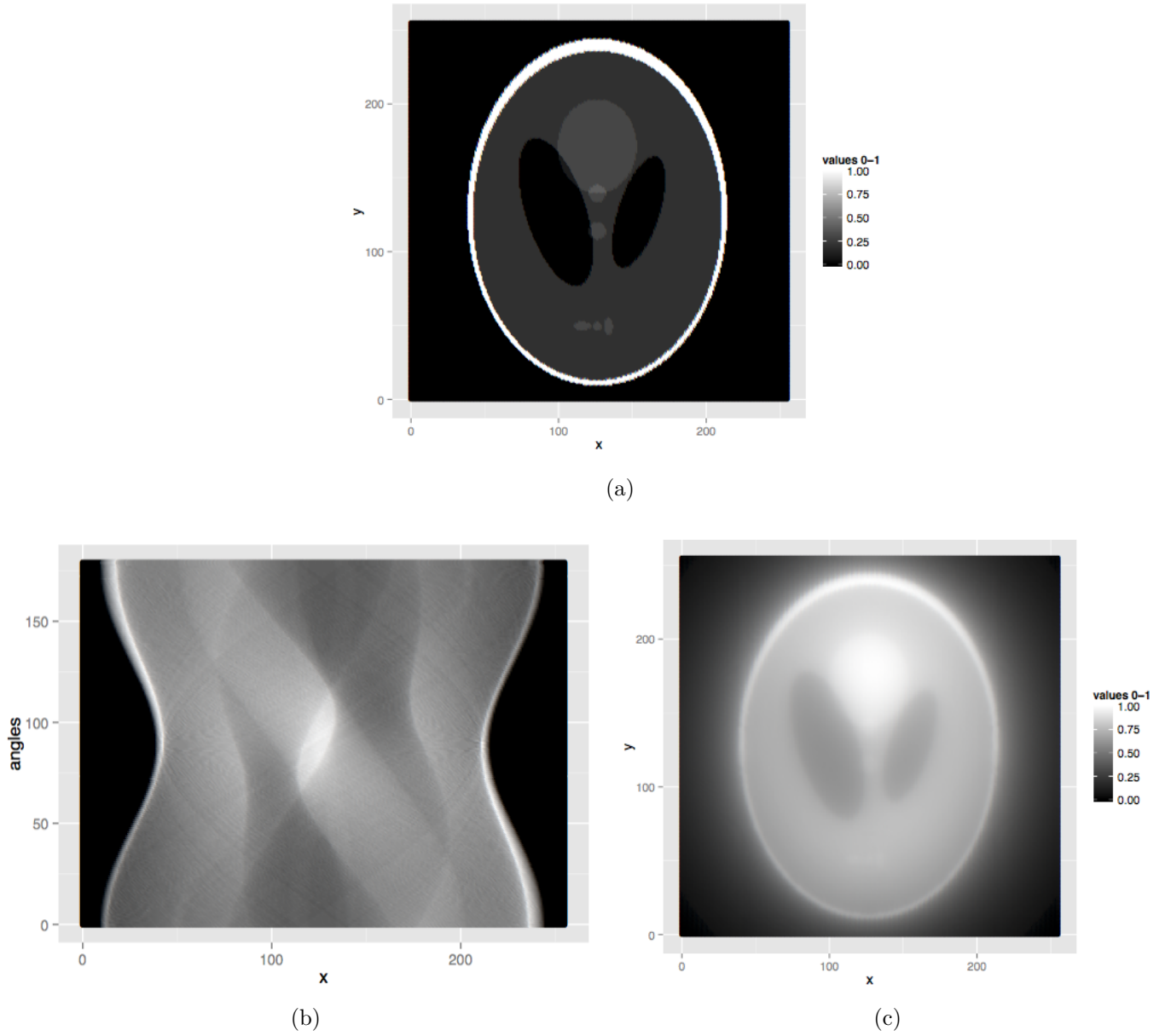
Figure 3.2: a) Image of a Shepp-Logan phantom. b) Sinogram of Shepp-Logan phantom acquired at a range from1° to 180° at a step size of 1°. c) Reconstruction obtained from the implementation of backprojection algorithm on the sinogram from (b).

However, in practice there is only a discrete set of projection data for a finite number of angles [46]. For the same reason, it become impossible to exactly reconstruct the initial $f(x, y)$. Nonetheless, if there are enough projections, one for each angular view, they can be inverted to arrive at an estimate of $f(x, y)$ [47]. The next two subsections will elucidate on the most commonly used methods of backprojection to acquire a good reconstruction with the discrete set of projections.

Algorithm 3.1 Sinogram for 2D tomography

- **for** θ in 1° to 180°

    (a) Rotate $f(x, y)$ at the angle θ.

    (b) Determine 1D projection for angle θ via summing $f(x, *)$.

    (c) Store the 1D projection at the angle θ in the sinogram matrix

- **end for**

3.1.3   Filtered Backprojection (FBP)

The reconstruction depicted in figure 3.2 is obtained by using the backprojection formula in eq. 3.7 where $|\rho| = 1$. However, this is not usually the case. $|\rho|$ represents a filtering operation and has values other than unity. A reconstruction obtained after using a filter, as suggested by eq. 3.6, is called filtered backprojection. $|\rho|$ is convoluted with the projection data. Hence, filtered backprojection is also called convolution backprojection. Filtering operation is carried out in the frequency domain. This is owing to that fact that the convolution in the real domain translates as a mere multiplicative operation in the frequency domain.

In tomographic reconstruction, filters are used to eliminate a specific range of frequency component of the projection data. As for instance, low-pass filter has cut-off frequency above which the frequencies are eliminated. Such removal can greatly improve the resolution and limit the degradation of the reconstructed image. However, one needs to be cautious while choosing the cut-off frequency. A high cut-off frequency will improve the spatial resolution and therefore much detail can be seen but the image will remain

noisy. Likewise, a low cut-off frequency will increase smoothing but will degrade image contrast in the final reconstruction [48]. Hence, depending upon the type of application the reconstruction serves the purpose, one ascertains the type of filter to be applied to the projection data. Some of the commonly used filters in medical tomography include Butterworth, cosine, Shepp-Logan, Hanning, Hamming, and Wiener filters. A detailed description about these filters can be found elsewhere in the references [48] and [49].

A particular filter that is used throughout the discourse of our research is the Ram-Lak filter [2]. Ram-Lak filter is a low-pass filter and has the dimension same as that of the projection data. The reason behind selecting this filter stems from the fact that it facilitates a reconstruction with a higher degree of spatial resolution, less blurriness and preserves the edges in final results as compared to the results acquired using other filters. Mathematically, Ram-Lak filter is an absolute value function in the Fourier domain. Suppose there are N data extensions for a projection, P_θ . Then the Ram-Lak filter extend from $-\frac{N}{2}$ to $(\frac{N}{2} - 1)$ and is defined in following ways:

Let,

$$k = -\frac{N}{2}, -\frac{N}{2} - 1, \ldots, -1, 0, 1, \ldots, \frac{N}{2} - 2, \frac{N}{2} - 1.$$

Then,

$$|\rho| = \frac{|k|}{N}. \tag{3.8}$$

A depiction of the Ram-Lak filter is presented in figure 3.3. Ram-Lak filter when convoluted with the projection data, results in a filtered sinogram as shown in figure 3.4a. When the filtered sinogram is backprojected, it gives a new reconstructed image as illustrated in figure 3.4b. Having used the filter, one can clearly observe that the blurriness and the white noise in the reconstruction have been subdued to a larger extent when compared to the corresponding filterless result in figure 3.2c. The superior nature of the reconstruction from filtered backprojection over backprojection is not just limited to the qualitative visualization. In fact, the level of improvement can be measured via a quantitative analysis tool called root mean square error (RMSE) analysis. Mathematically, RMSE is defined as:
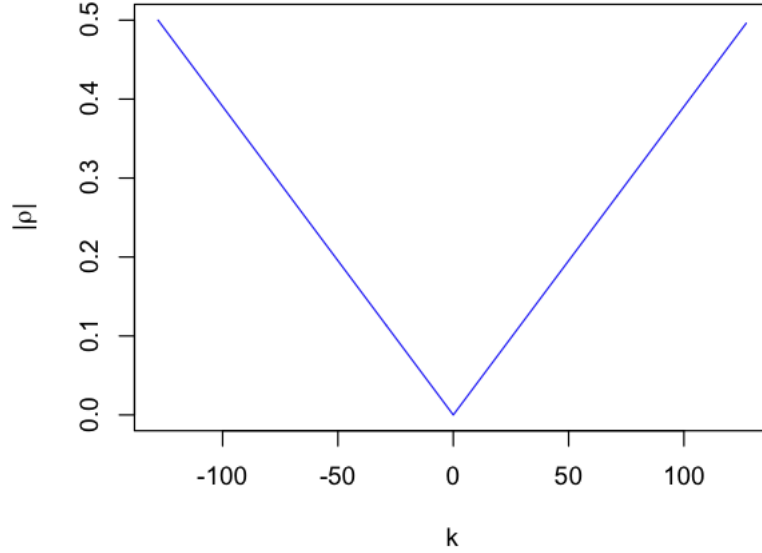
Figure 3.3: Ram-Lak filter (Ramachandran and Lakshminarayanan, 1971) [2]

$$RMSE = \sqrt{\frac{\sum\limits_{i=1}^{n} (\hat{y}_i - y_i)^2}{n}},$$

where,

$\hat{y}$ denotes theoretical values,

y denotes reconstructed values,

n is the total number of points.

Table 3.1 explicitly indicates a lower RMSE for the filtered backprojection result than the backprojection result. Thus, substantiating the fact that the filtering operation improves the tomographic reconstruction. Having said this, there is also a different class of reconstruction method called iterative method that can greatly improve the final results. In fact, in many cases it has been successfully demonstrated that iterative methods are capable of capturing the minute details in the reconstruction at a higher precision than the analytical methods like FBP [50, 51]. The only flaw with the iterative methods is that, these methods are computationally intensive for they adopt various numerical techniques in their algorithms. However, the advent of processors with higher computing power has made it possible to extensively use the iterative methods. For the same
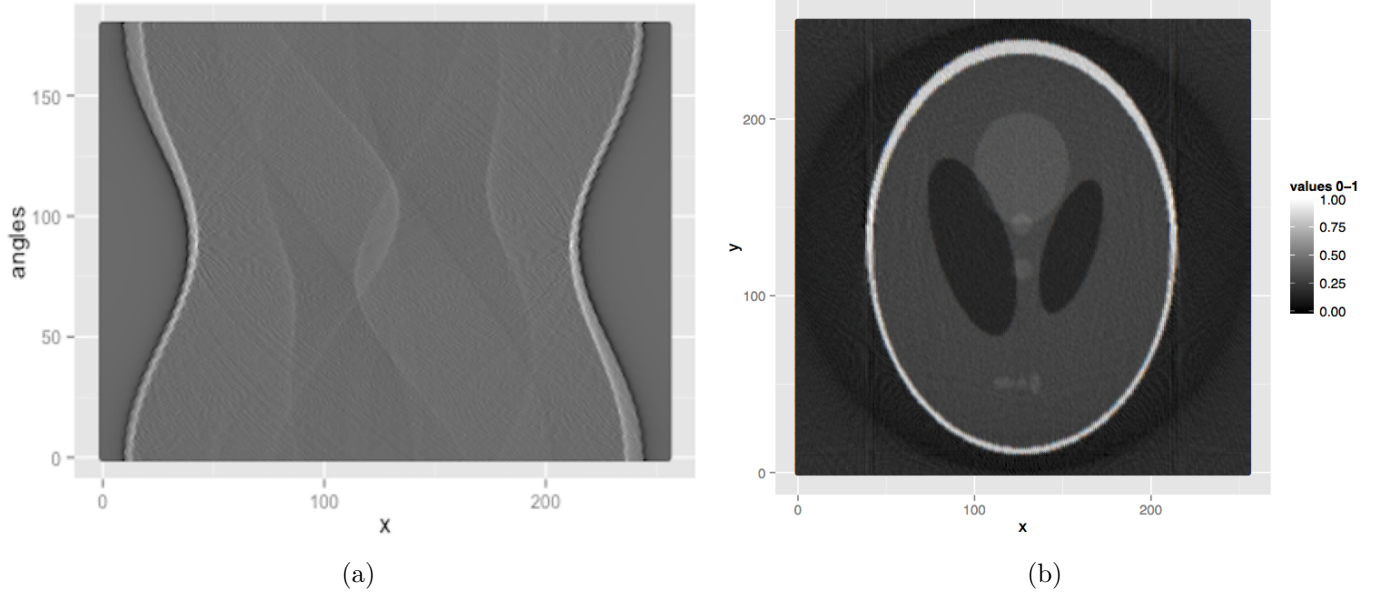
Figure 3.4: a) Filtered sinogram obtained by convoluting each projection with the Ram-Lak filter. b) Filter backprojected reconstruction of the Shepp-Logan phantom.

reasons, iterative methods have been slowly replacing the conventional FBP methods in various fields. This is also the very reason as to why we are looking to move forward from the vector field electron tomography (VFET), which is based on FBP, to Model Based Iterative Reconstruction (MBIR), which is based on iterative method, for our research work on electromagnetic characterization. An in-depth description of VFET and MBIR will be covered in chapters 4, 5, and 6. Nonetheless, in order to acquaint the readers about the tomographic iterative technique, one of the earliest forms of iterative methods called Simultaneous Iterative Reconstruction Technique (SIRT) is briefly explained in the next section.

3.1.4   Simultaneous Iterative Reconstruction Technique (SIRT)

SIRT is one of the commonly used iterative techniques to perform scalar tomography [52]. Using the SIRT algorithm, one generally obtains smoother and better-looking reconstructions at the expense of slower convergence. A pseudo code for the SIRT implementation is depicted in the algorithm 3.3. A thorough review of the SIRT algorithm will

---

Algorithm 3.2 Filtered Backprojection

- **for** θ in $1°$ to $180°$

    1. Perform the Fourier Transform of the 1D projection at the angle θ.

    2. Multiply Ram-Lak filter and 1D projection at the angle θ.

    3. Perform inverse Fourier Transform of the result from pervious step (say P_θ).

    4. Evaluate, $f(x,y) += P_\theta(x\cos\theta + y\sin\theta)$

- **end for**

    $f(x,y) = \frac{\pi}{180} f(x,y)$

---

reveal that it begins with filtered backprojection and iteratively updates the subsequent reconstruction. However, the most important step in this approach is where it determines the error sinogram, a difference between the weighted first sinogram measurement ($\lambda \times Pf^0$) and the subsequent sinogram (Pf^i), for each iterations. Here, the weighting factor/ relaxation parameter, λ, is chosen so as to attain the best possible reconstruction in a reasonable amount of time. A direct implication of this step is the minimization of the error sinogram. In particular, with the subsequent iteration, there will be less and less difference between the first sinogram measurement and the newly evaluated sinogram; thus, producing a better reconstruction.

A Shepp-Logan phantom reconstruction using the SIRT algorithm is illustrated in figure 3.5. Here, the λ value was chosen to be 0.25 and the result was obtained after 10 iterations. Other than the visual confirmation of a better reconstruction from the SIRT method, RMSE values in table 3.1 also corroborate the same conclusion from the quantitative point of view. All these results provide us with the incentive to adhere to iterative methods, like SIRT, to perform reconstruction instead of analytic method, like FBP.

Having said this, it has to be pointed out that there is no theoretical understanding as to what value of λ should be chosen for a particular reconstruction problem using the

---

Algorithm 3.3 SIRT

- Perform FBP on the sinogram measurement, Pf^0, to evaluate the first estimate f^0.

- **for** i in $1 : N$

  1. Compute new sinogram, Pf^i, for the object, f^{i-1}.

  2. Update the reconstruction as, $f^i \leftarrow f^{i-1} + FBP\ (Pf^i - \lambda \times Pf^0)$. Here, λ is a user input parameter and $\lambda \in (0, 1)$.

  3. Compute the average update as $\sum \frac{|f^i - f^{i-1}|}{N}$.

  4. If average update $<$ threshold, exit the loop.

- **end for**
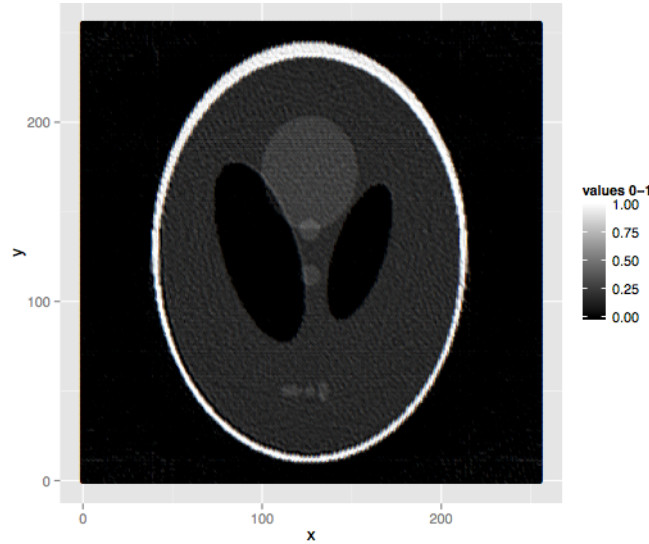
Figure 3.5: SIRT implemented reconstruction of Shepp-Logan phantom after 8 iterations using $\lambda = 0.25$.

SIRT method. This serious flaw in the SIRT approach arises from fact that it does not have a framework that ensures the minimization of the error sinogram in the successive iterations. Therefore, one needs to put flags at the different steps of each iteration to deduce a properly resolved reconstruction, $f(x, y)$. Moreover, it might be that there exists a different reconstruction result, $f'(x, y)$, even better than $f(x, y)$ for a distinct values of λ' and iteration number. These issues of the SIRT approach only get amplified in the problems dealing with the reconstruction of vector fields. The reasoning being that a vector reconstruction problem is much more complicated than a scalar reconstruction. The output of the vector reconstruction is comprised of continuously varying values instead of patches of fixed values as in the case of scalar reconstruction. Hence, it will be exceedingly difficult to guess a particular λ that successfully will be able to minimize the error sinogram for certain number of iterations to yield a reconstruction better than that from FBP approach.

Overall, the cumbersome nature of SIRT to meet the convergence criteria does not negate the fact that an iteratively converged reconstruction result is usually better than a simple FBP result. Accordingly, we seek to adopt a more robust iterative technique than SIRT whose algorithm incorporates a theoretical premise that ensures the minimization of error sinogram in the successive iterations. One such technique is the Model Based Iterative Reconstruction (MBIR). MBIR is based on the Bayesian interface. It encompasses prior knowledge of the system and the convergence criterion is met via implementing a theoretically proven recipe that minimizes the error sinogram in each iteration. An elaborate description on the MBIR method will be laid out in chapter 6. For now, we continue with the spirit of this chapter about the general tomography methods and move ahead with the 3D tomography.

Method	RMSE
Backprojection	0.46
Filtered Backprojection	0.16
SIRT	0.08

Table 3.1: RMSE

3.2 3D Tomography

As mentioned earlier, 3D tomography can in fact be extrapolated easily from the 2D tomography. The only difference in 3D tomography when compared with 2D tomography is that the projection measurements are 2D in nature. These 2D measurements are acquired via simultaneously rotating a 3D object along a fixed axis and passing the radiation along one of the other axes. For the purpose of computational implementation, we will demonstrate 3D tomography with the aid of the filtered backprojection. The object in concern is a cuboid that is defined to have a value of one everywhere within its boundary.

First, we determine the projection planes for the angles ranging from 1° to 180°. The cuboid is rotated along x axis. This rotation is depicted in the figure 3.6 for three angles namely, 0°, 45° and 90°. Next, radon transform of the rotated cuboid is evaluated along z direction. In other words, summation along the z direction of the tilted cuboid. Accumulation of projection planes from angles 1° to 180° yields a 3D sinogram.

Algorithm 3.4 3D Filtered Backprojection

---

for θ in 1° to 180°

- **for** x in $1:N$

  1. Perform the 2D Fourier Transform of the projection plane at the angle θ as $\hat{P}_\theta(k_y, k_z) = FFT(P_\theta(y, z))$.

  2. For k_y in 1:N

     – Perform the multiplication of Ram-Lak filter as $\hat{P}_\theta(k_y, *) \leftarrow \hat{P}_\theta(k_y, *) \times |\rho|$.

  3. Evaluate the 2D inverse Fourier Transform of the filtered planes as $P_\theta(y, z) = iFFT(\hat{P}_\theta(k_y, k_z))$.

  4. Evaluate, $f(x, y, z) += P_\theta(x, y\cos\theta + z\sin\theta)$.

- **end for**

- $f(x, y, z) \leftarrow \frac{\pi}{180} f(x, y, z)$

end for
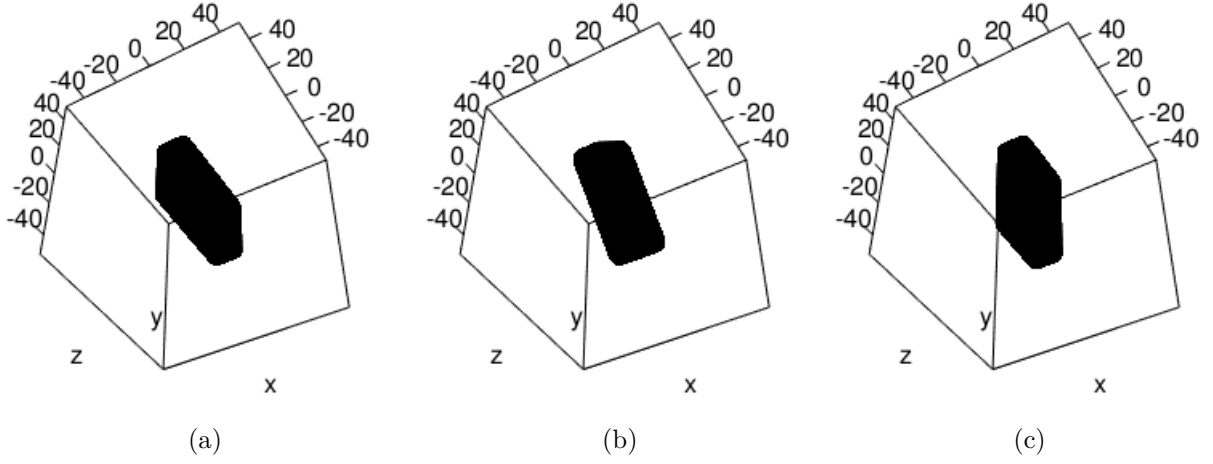
Figure 3.6: Illustration of x-tilted rotations of the cuboid for angles (a) 0° (b) 45° and (c) 90°.

The second step of the implementation comprises of retrieving the cuboid from the sinogram. Here, filtering operation will also be implemented to yield a more accurate reconstruction. As in the case of 2D tomography, we again make use of Ram-Lak filter. Ram-Lak filter is convoluted with each of the 1D - strip of each of the projection planes. Finally, each of the filtered projection planes is backprojected and summed in the 3D space. A pseudo code for the 3D filtered backprojection is illustrated in algorithm 3.4. Likewise, the results from the filtered backprojection of the 2d projection planes is depicted in figure 3.7. It shows some of the reconstructed planes of the cuboid. For the convenience of the reader, red color has been used to highlight the parts that deviate away from the true values, indicated by the black color. The more the red the further away is the reconstructed value from the true value. Additionally, the RMSE value below each of the planar plots provides a quantitative gauge over the reconstruction accuracy. A thorough review of the planer plots will reveal that the RMSE values across the x planes are basically the same; for the results were obtained via x tilt series. In contrast to this, planes in y and z directions demonstrate different levels of accuracy. Still, it is not difficult to realize that the y and z planes across the origin indicate higher levels of reconstruction accuracy that the ones along and around the edges of the cuboid. This particular observation that the level of reconstruction accuracy along/around edges is lesser than the accuracy of the

other parts of the object will be a constantly reoccurring theme throughout the discourse of our research work. We will provide more insight on this subject matter in chapter 4. For now, we proceed to discuss on the implication of limited tilt angles which is a fundamental source of errors in tomographic reconstruction in the next section.
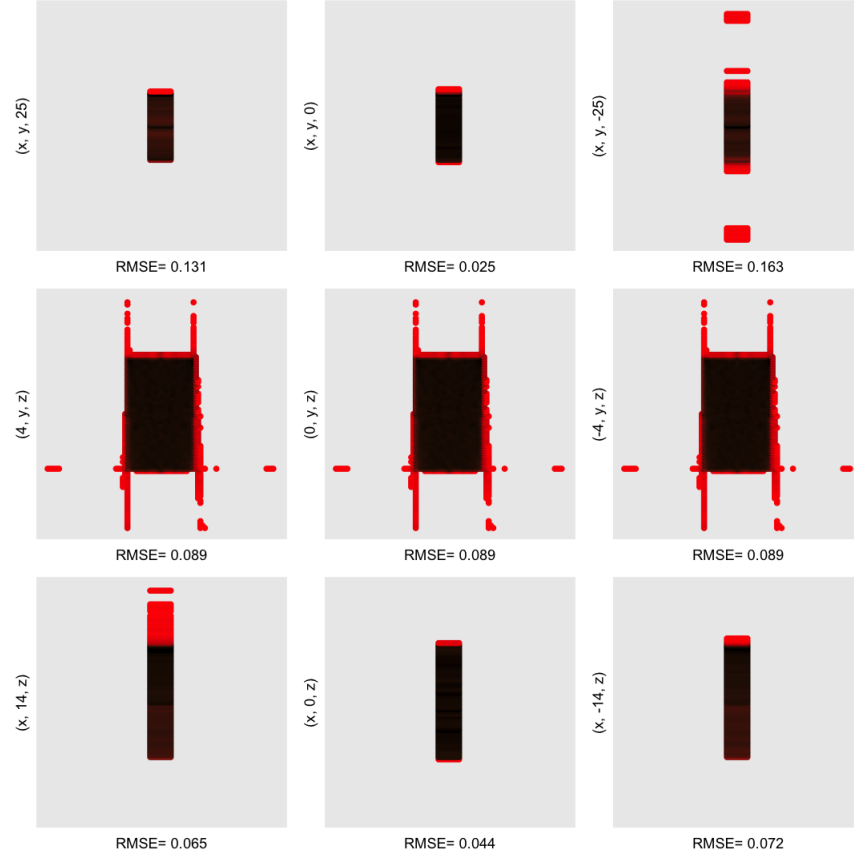
Figure 3.7: Some of the planes obtained from the 3D filtered backprojection of 2D projection planes of a cuboid (10, 30, 50) ranging from 0° to 179°.

3.3 Limited tilt angles

This particular section may, initially, seem to be an outlier in a chapter that is primarily devoted to the description of the basics of tomography. However, we will, regularly, come across the phenomenon of limited tilt angles throughout the discourse of our vectorial

tomography research. Hence, it was thought appropriate to discuss the effect of limited tilt series in this early stage along with rest of the basics about tomography.
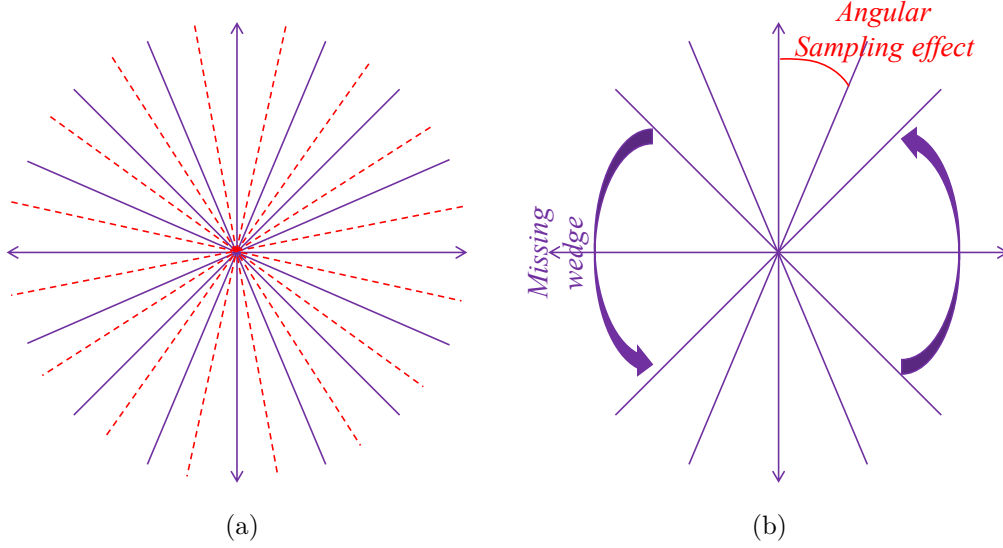
Figure 3.8: Schematics representing (a) full tilt, (b) missing wedge of information and effect of angular sampling in projection measurements for tomography.

Firstly, it has already been established that it not possible to exactly recover the initial function, $f(x, y)$, from the discrete set of projections, P_θ. Nonetheless, one can deduce a good approximation of $f(x, y)$ if there are enough projections. In particular, one for each angular view in the range of 180 degrees [46, 47]. For the same reason, it is not difficult to realize that the reconstruction becomes inaccurate when the tilt range is less than the theoretically required 180 degrees. The situation arising due to limited tilt series is technically termed as 'missing wedge' of information [32]. A schematic depicting the concept of missing wedge is provided in figure 3.8.

In many practical applications, instruments do not allow the users to acquire a full 180 degree tilt series. This experimental limitation is especially true in the case of our research. We rely on Transmission Electron Microscopy (TEM) to acquire the projection measurements. TEM holders built specifically for the purpose of tomography, allows a tilt series of $\pm 70°$. In addition, these measurements are taken at a step size of $2°$ to $5°$ to protect sample from beam damage [31] instead of $1°$ or $0.5°$ step size required for an ideal

reconstruction. Thus resulting limited tilt series is referred as effect of angular sampling [53] and it has a great implication in the quality of reconstruction. The diminishing reconstruction quality can be inferred from figures 3.9 and 3.10. The former depicts the angular sampling effect on tomographic reconstruction while the latter illustrates reconstruction from a measurement that exhibits a missing angular range.
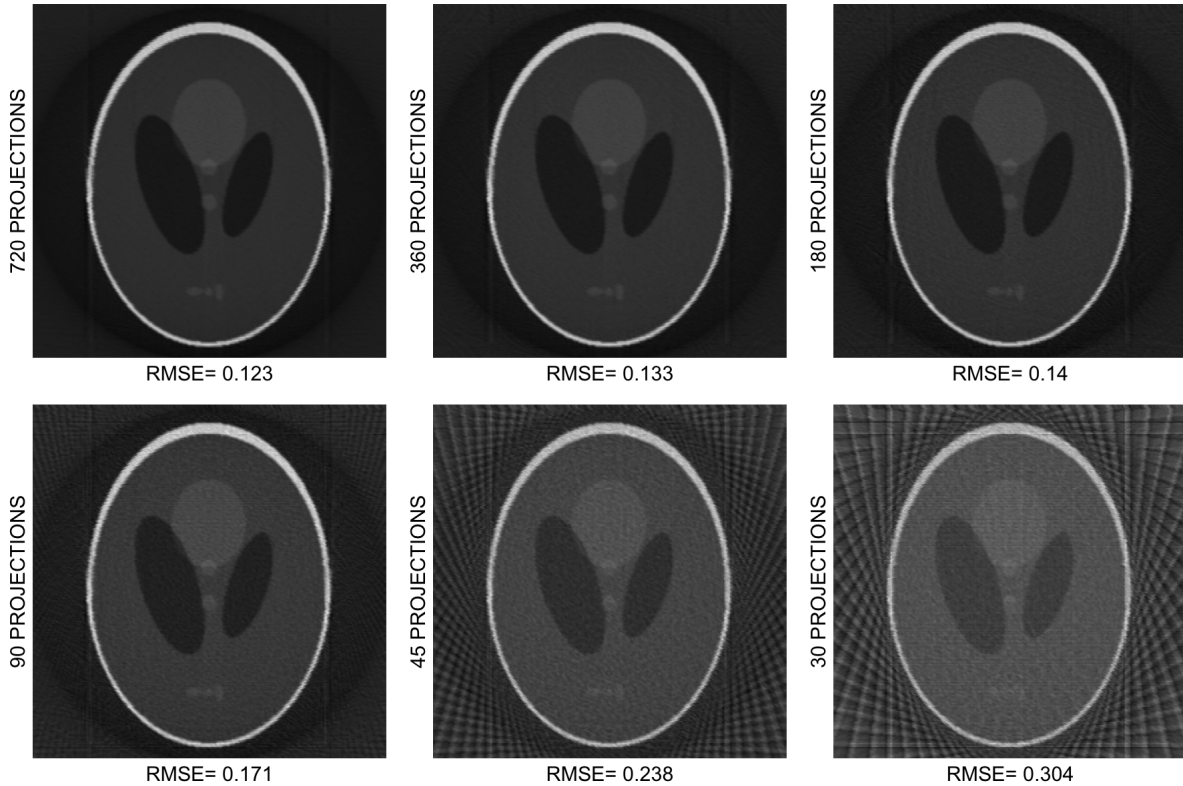
Figure 3.9: Shepp-Logan phantoms illustrating the increasing trend in the RMSE value with the decrease in the number of projections for the tilt range of $[0°, 180°)$. These phantoms have values in the range 0 (corresponding to black) to 1 (corresponding to white)

Accordingly, it becomes imperative to address the issue of missing wedge while constructing the model for electromagnetic characterization from tomographic measurements. Recognizing this concern, we surmise that statistically sound methods like MBIR approach will be able to mitigate the effects of missing wedge of information. The result of our claim will be provided in chapter 6 after we have laid down the fundamentals of the MBIR

approach and the thought process on why it might work for our problem.
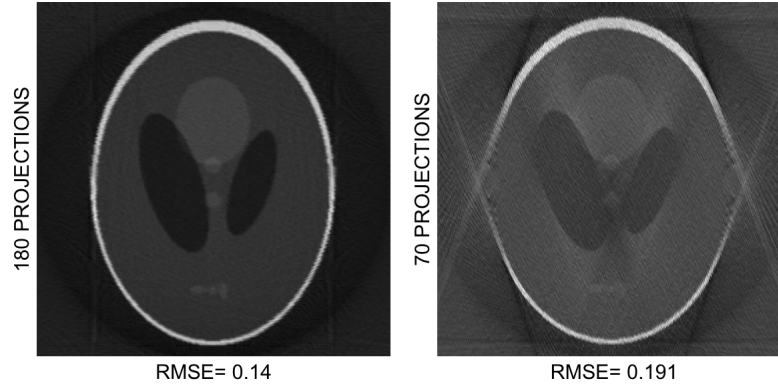
Figure 3.10: A computational implementation of missing wedge phenomenon where the left plot is deduced from a measurement with $\pm 90°$ angular range at $1°$ deg stepsize while the right plot is reconstructed from the one with $\pm 70°$ angular range at $2°$ stepsize. These phantoms have values in the range 0 (corresponding to black) to 1 (corresponding to white)

This concludes our explanation of scalar tomography. Summing up, we have thoroughly explained the fundamentals of 2D and 3D tomography in this chapter. Likewise, we have described some of the commonly used tomography methods like filtered back-projection and SIRT. We have provided pseudo codes for computation implementations, recognized sources of error in the reconstruction and have alluded to the techniques like MBIR that can be adopted for a better reconstruction. The acceptance or rejection of our initial claim to use the MBIR approach to deduce a good estimate of the object will be made after its implementation in later chapters. For now, we proceed to explain vectorial form of tomography.

Chapter 4

Vector Tomography

The seventies and eighties saw an immense success in the use tomographic techniques to reconstruct scalar objects, especially in the areas pertaining to clinical diagnosis. These successes at the scalar interference led researchers to investigate if the concept of tomography could be extended to reconstruct velocity vector fields. A proper incorporation of vector tomography would open door for breakthroughs in areas such as oceanography, photoelasticity, medical fluid flow imaging [54] where determining 3D fields from 2D measurements is of immense importance. Accordingly, Norton, for the first time, outlined a mathematical model to deduce the 2D fluid field from acoustic time travel measurements in 1988. In subsequent years, 2D vector tomography was extended to the 3D cases. In particular, Juhlin resolved the solenoidal part of a divergence free flow field using ultrasound Doppler measurements in 1992 [55]. Since then researchers in various areas have adopted vector tomography to reconstruct the 3D solenoidal part of a vector field. Similarly, we seek to make use of vector tomography to reconstruct magnetic vector potential (solenoidal field) of nanoparticles from TEM micrographs.

This chapter outlines 2D and 3D vector tomography frameworks to reconstruct vector fields. We begin with Norton's article [56] as an introduction to the 2D vector tomography by reconstructing solenoidal part of a field. Subsequently, we build upon the 2D vector tomography to elucidate the details of 3D Vector Field Electron Tomography (VFET).

4.1   2D Vector Tomography

In this section, we lay out the theoretical framework as well as the computation implementation to reconstruct the solenoidal part of a 2D vector field as detailed by Norton in his paper, "Tomographic reconstruction of 2D vector fields: application to flow imaging" [56].

4.1.1   Theoretical framework

The theoretical formulation of 2D vector tomography begins by considering a 2D vector field, $\mathbf{v}(x,y)$, defined as:

$$\mathbf{v}(x,y) = v_x(x,y)\hat{x} + v_y(x,y)\hat{y}. \tag{4.1}$$

Here, (x,y) is the initial reference frame. Define a counter-clockwise rotation matrix, R_θ, as:

$$R_\theta = \left[\begin{array}{cc} \cos(\theta) & -\sin(\theta) \\ \sin(\theta) & \cos(\theta) \end{array} \right]. \tag{4.2}$$

Now, consider a new reference frame (ρ, l) which is at an angle, θ, from the old reference frame, (x,y). Hence, every point in (ρ, l) is at an angle θ from the initial reference frame (x,y) such that:

$$\left[\begin{array}{c} x \\ y \end{array} \right] = R_\theta \left[\begin{array}{c} \rho \\ l \end{array} \right]. \tag{4.3}$$

One can utilize eq. 4.3 to deduce the radon transform of the field $\mathbf{v}(x,y)$ at different angles. As noted before in chapter 3, radon transform is required to model the projections for the tomographic reconstruction. Accordingly, the projection, $T_\theta(\rho)$, at an inclination, θ, for the 2D field can be defined as:

$$T_\theta(\rho) = \int\limits_{-\infty}^{\infty} \mathbf{v}(x,y) \cdot d\mathbf{l}, \tag{4.4}$$
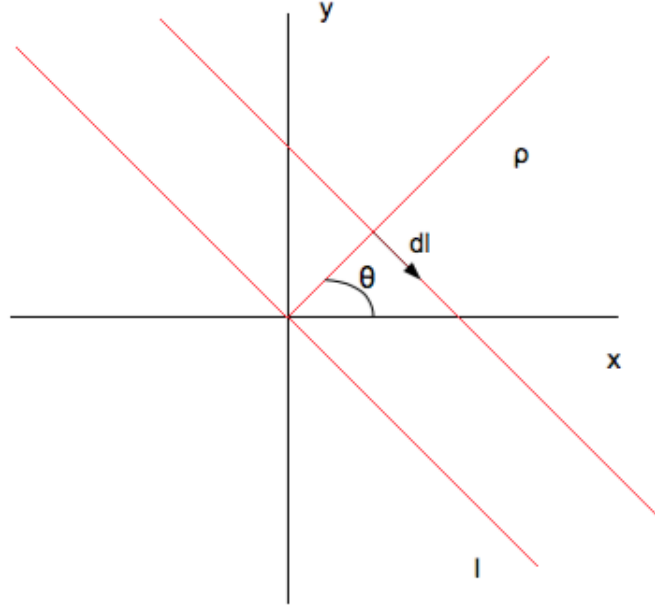
Figure 4.1: Old reference frame,(x, y), in-terms of new reference frame, (ρ, l).

where, $d\mathbf{l}$ is the element of the projection line $L(\rho, \theta)$ as shown in figure 4.1. Mathematically,

$$
\begin{aligned}
d\mathbf{l} &= \hat{x} dl \cos(90^{o} - \theta) + \{-\hat{y} dl \sin(90^{o} - \theta)\} \\
&= \hat{x} \sin(\theta) dl - \hat{y} \cos(\theta) dl.
\end{aligned}
\tag{4.5}
$$

Having defined a new reference frame and the line integrals for any given angle of inclination, the projection expression in eq. 4.4 can be generalized as:

$$
\begin{aligned}
T_\theta(\rho) &= \int_{-\infty}^{\infty} \mathbf{v}(x,y) \cdot d\mathbf{l} \\
&= \int_{-\infty}^{\infty} (\ v_x(x,y)\hat{x} + v_y(x,y)\hat{y}).(\hat{x}\sin(\theta)dl - \hat{y}\cos(\theta)dl) \\
&= \int_{-\infty}^{\infty} v_x(x,y)\sin(\theta)dl - \int_{-\infty}^{\infty} v_y(x,y)\cos(\theta)dl \\
&= \sin(\theta)\int_{-\infty}^{\infty} v_x(\{\rho\cos(\theta) - l\sin(\theta)\}, \{\rho\sin(\theta) + l\cos(\theta)\})dl \\
&\quad - \cos(\theta)\int_{-\infty}^{\infty} v_y(\{\rho\cos(\theta) - l\sin(\theta)\}, \{\rho\sin(\theta) + l\cos(\theta)\})dl.
\end{aligned}
\tag{4.6}
$$

To put eq. 4.6 in words, it turns out that determining the projections of a field is equivalent to rotating the field at the given angle, taking the line integrals of x and y components of the field, multiplying the line integrals in the x component sine of the angle and the y component by cosine of the angle, and taking the difference between the line integrals of the two field components.

One can also use Fourier analysis to determine the projection in the Fourier space as:

$$
\begin{aligned}
\tilde{T}_\theta(k) &= \int_{-\infty}^{\infty} T(\rho)e^{-2\pi i k\rho}d\rho \\
&= \sin(\theta)\int_{-\infty}^{\infty}\int_{-\infty}^{\infty} v_x(x,y)e^{-2\pi i(xk\cos(\theta) + yk\sin(\theta))}dxdy \\
&\quad - \cos(\theta)\int_{-\infty}^{\infty}\int_{-\infty}^{\infty} v_y(x,y)e^{-2\pi i(xk\cos(\theta) + yk\sin(\theta))}dxdy \\
&= \sin(\theta)\tilde{v}_x(k\cos(\theta), k\sin(\theta)) - \cos(\theta)\tilde{v}_y(k\cos(\theta), k\sin(\theta)).
\end{aligned}
\tag{4.7}
$$

Before divulging any further, the 2D fluid field, $\mathbf{v}(x,y)$, is decomposed into its irrotational, Φ, and solenoidal, $\boldsymbol{\Psi}$, part as follows:

$$
\mathbf{v} = -\nabla\Phi + \nabla\times\boldsymbol{\Psi},
\tag{4.8}
$$

where,

$$\nabla \Phi = -\hat{x}\frac{\partial \Phi}{\partial x} - \hat{y}\frac{\partial \Phi}{\partial y}, \tag{4.9}$$

$$\nabla \times \mathbf{\Psi} = \hat{x}\frac{\partial \mathbf{\Psi}}{\partial y} - \hat{y}\frac{\partial \mathbf{\Psi}}{\partial x}. \tag{4.10}$$

Again, from equations 4.1, 4.8, 4.9 and 4.10, each of the components of $\mathbf{v}$ can be written as the linear combination of their respective irrotational and solenoid components as:

$$v_x(x,y) = -\frac{\partial \Phi}{\partial x} + \frac{\partial \mathbf{\Psi}}{\partial y}, \tag{4.11}$$

$$v_y(x,y) = -\frac{\partial \Phi}{\partial y} - \frac{\partial \mathbf{\Psi}}{\partial x}. \tag{4.12}$$

Furthermore, performing the Fourier transforms of the expressions in eq. 4.11 and eq. 4.12, one gets:

$$\tilde{v}_x(x,y) = -2\pi i k_x \tilde{\Phi}(k_x, k_y) + 2\pi i k_y \tilde{\mathbf{\Psi}}(k_x, k_y), \tag{4.13}$$

$$\tilde{v}_y(x,y) = -2\pi i k_y \tilde{\Phi}(k_x, k_y) - 2\pi i k_x \tilde{\mathbf{\Psi}}(k_x, k_y). \tag{4.14}$$

With this, one can revisit the projection expression in eq. 4.7 and subsequently re-write it as:

$$
\begin{aligned}
\tilde{T}_\theta(k) &= \sin(\theta)\tilde{v}_x(k\cos(\theta), k\sin(\theta)) - \cos(\theta)\tilde{v}_y(k\cos(\theta), k\sin(\theta)) \\
&= \sin(\theta)\{-2\pi i k \cos(\theta)\tilde{\Phi}(k\cos(\theta), k\sin(\theta)) + 2\pi i k \sin(\theta)\tilde{\mathbf{\Psi}}(k\cos(\theta), k\sin(\theta))\} \\
&\quad - \cos(\theta)\{-2\pi i k \sin(\theta)\tilde{\Phi}(k\cos(\theta), k\sin(\theta)) - 2\pi i k \cos(\theta)\tilde{\mathbf{\Psi}}(k\cos(\theta), k\sin(\theta))\} \\
&= -2\pi i k \sin(\theta)\cos(\theta)\tilde{\Phi}(k\cos(\theta), k\sin(\theta)) + 2\pi i k \sin^2(\theta)\tilde{\mathbf{\Psi}}(k\cos(\theta), k\sin(\theta)) \\
&\quad + 2\pi i k \sin(\theta)\cos(\theta)\tilde{\Phi}(k\cos(\theta), k\sin(\theta)) + 2\pi i k \cos^2(\theta)\tilde{\mathbf{\Psi}}(k\cos(\theta), k\sin(\theta)) \\
&= 2\pi i k \tilde{\mathbf{\Psi}}(k\cos(\theta), k\sin(\theta)). \tag{4.15}
\end{aligned}
$$

$$
\begin{aligned}
\implies \tilde{\mathbf{\Psi}}_\theta(k) &= \frac{\tilde{T}_\theta(k)}{2\pi i k} \\
&= \frac{\sin(\theta)\tilde{v}_x(k\cos(\theta), k\sin(\theta))}{2\pi i k} - \frac{\cos(\theta)\tilde{v}_y(k\cos(\theta), k\sin(\theta))}{2\pi i k} \tag{4.16} \\
&= \tilde{\Psi}_{\theta,x} + \tilde{\Psi}_{\theta,y}.
\end{aligned}
$$

From eq. 4.15 it is clear that the irrotational part vanishes and does not contribute to the projection measurements acquired from any of the components of the field, $\mathbf{v}$. Moreover, eq. 4.16 suggests that the central slice of the rotated field's x component (in the Fourier space) scaled by the factor $\frac{\sin(\theta)}{2\pi i k}$ yields solenoid projection for the x component, $\tilde{\Psi}_{\theta,x}$. Likewise, the central slice of the inclined y component scaled by the factor $\frac{\cos(\theta)}{2\pi i k}$ yields the solenoid projection for the y component, $\tilde{\Psi}_{\theta,y}$.

Having formulated the forward model for the 2D vector field, we make use of the Fourier Slice theorem to derive a backprojection recipe. Accordingly, the backprojection formula to reconstruct each of the components of the solenoidal part of $\mathbf{v}$ is determined to be:

$$
\begin{aligned}
\Psi_*(x,y) &= \int_{-\infty}^{\infty}\int_{-\infty}^{\infty} \tilde{\Psi}_*(k_x,k_y)e^{2\pi i(xk_x+yk_y)}dk_x dk_y \\
&= \int_{-\infty}^{\infty}\int_{0}^{\pi} \tilde{\Psi}_{\theta,*}(k)e^{2\pi i(xk\cos(\theta)+yk\sin(\theta))}d\theta dk \\
&= \int_{0}^{\pi}\left[\int_{-\infty}^{\infty} \tilde{\Psi}_{\theta,*}(k)e^{2\pi i k(x\cos(\theta)+y\sin(\theta))}dk\right]d\theta \\
&= \int_{0}^{\pi} \Psi_{\theta,*}(x\cos(\theta)+y\sin(\theta))d\theta.
\end{aligned}
\tag{4.17}
$$

$\Psi_*(x,y)$ denotes any of the two components (x or y) of the solenoid.

With this, we conclude the theoretical formulation of the reconstruction of the solenoid part of the 2D vector field using tomographic reconstruction. In the next subsection, we will elucidate on the computational aspects of the reconstruction of the solenoidal part of the vector field, $\mathbf{v}$, using its projections.

4.1.2 Computational Implementation

Consider a flow field, $\mathbf{v}$, in x direction inside a circle of radius, $R = 20$, such that:

$$
\mathbf{v}(x,y) = v_o\hat{x}, \qquad\qquad \text{where,}\ \ v_o = 1.
$$

(a)   (b)
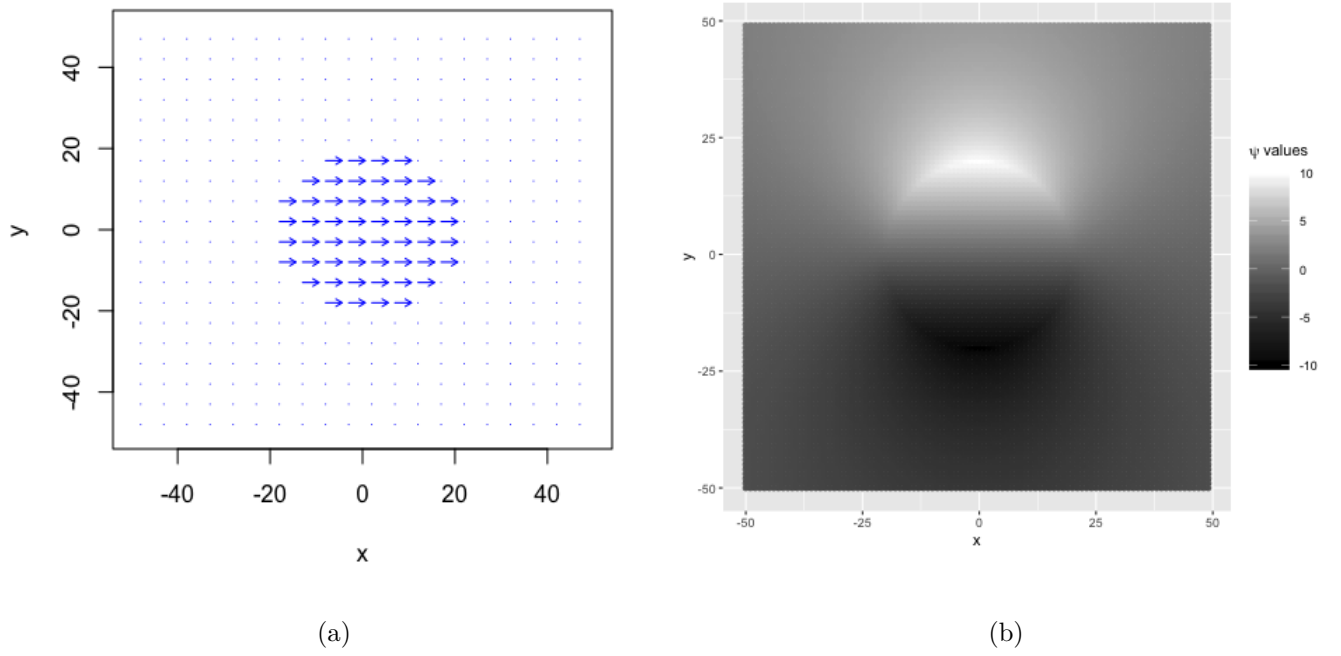
Figure 4.2: (a) 2d fluid flow within a circle with $\mathbf{v}(x, y) = v_o\hat{x}$. (b) Theoretical solenoid (Ψ) of the field, $\mathbf{v}$.

The field's solenoidal part is theoretically calculated [56] to be:

$$\boldsymbol{\Psi}(x,y) = \begin{cases} \frac{v_o y}{2}, & \text{for } r \leq R, \\ \frac{v_o R^2 y}{2r^2}, & \text{for } r > R. \end{cases}$$

Next, the solenoidal part of the field, $\mathbf{v}$, is reconstructed from its projections using filtered back projection (FBP). Each of the 1d solenoidal projection is convoluted with a filter. As in the case of scalar reconstruction, we again use Ram-Lak as our filter [2] such that:

$$\begin{aligned}
\boldsymbol{\Psi}_\theta(r) &= h(t) \otimes \boldsymbol{\Psi}_\theta(r) \\
&= \mathcal{F}^{-1}(|\rho|\tilde{\boldsymbol{\Psi}}_\theta(k)).
\end{aligned}$$
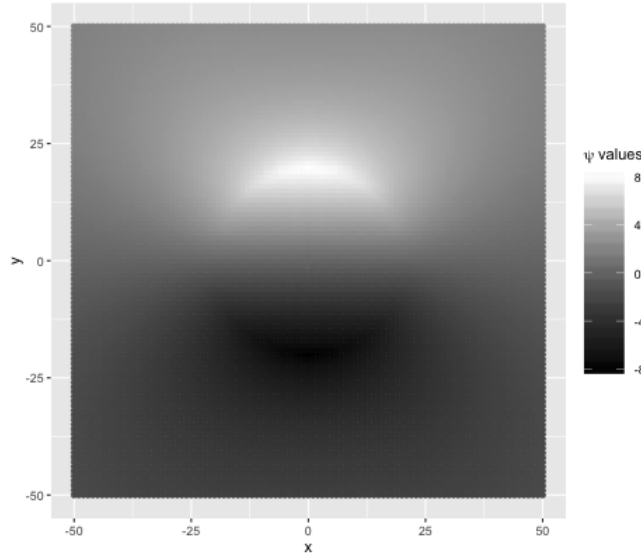
Figure 4.3: Reconstructed solenoid (Ψ) of the field, $\mathbf{v}$, using filter backprojection approach.

Note that the projection acquired from the 2D field has contributions from only the solenoidal part of the field, $\mathbf{v}$, as indicated by eq. 4.15. Hence, the reconstruction from the sinogram of $\mathbf{v}$ only yields the solenoidal part. However, one can make use of Green's

function as suggested by Norton to recover the irrotational part of the field. But in the case of 3D vector reconstruction the irrotational part or the electrostatic potential is recovered by simply performing a scalar tomography of the electrostatic phase. For the same reason, the recovery of the irrotational part of the 2D field, **v**, is out of scope here. Interested readers can follow Norton's paper to deduce the irrotational part of **v**.

This concludes a basic review of 2D vector tomography. We now proceed to the 3D vector tomography in the next section.

4.2   Vector Field Electron Tomography (VFET)

This subsection gives a thorough overview on the current state-of-art of tomographic reconstruction of magnetic vector potential from a series of Lorentz TEM images. We use the work of Phatak et al. [34] and Lade et al. [57, 58] to formulate a theoretical framework for the magnetic vector potential, $\mathbf{A}(\mathbf{r})$, reconstruction. Based on the framework, we outline pseudo codes to reconstruct $\mathbf{A}(\mathbf{r})$. We conclude this section with some of the results from the VFET approach.

To begin with, the application of tomography to reconstruct the magnetic vector potential of the nanoparticles using Lorentz TEM images is known as vector field electron tomography (VFET) [59]. The basic premise of the VFET is analogous to that of the scalar tomography, because the VFET approach, too, makes use of forward projection, Fourier Slice Theorem and backprojection. Moreover, it incorporates the filtered backprojection approach to perform the reconstruction. A major point of difference between vector tomography and scalar tomography is the tilt acquisition aspect. The VFET approach requires sinograms from at least two different tilt series to reconstruct all the components of the magnetic vector potential. A more detailed analysis on the VFET approach is provided in the following subsections:

4.2.1   Forward projection to determine the magnetic phase shift

Recall from scalar tomography that the forward projection approach enables us to formulate mathematical model of projection measurements acquired from an experiment.

This is true even in the case of vector tomography. In particular, the forward projection methodology is utilized in the vector tomography to model the measurements acquired from a Lorentz TEM experiment. However, there is a caveat. It has already been discussed in chapter 2 that the Lorentz TEM experiment does not directly output the magnetic phase information. Rather it provides the modulus of the electron wave that exits the sample or, simply, the image intensity. For this reason, the Transport of Intensity Equation (TIE) [41] formalism is used to retrieve phase shift from the TEM image. Thus deduced phase shift has contributions from the electrostatic as well as the magnetic potential of the sample. Time reversal symmetry [42] is, then, used to separate the magnetic phase from the electrostatic phase. We assume that the pre-processing steps - the TIE operation and the phase separation - have already been performed. Consequently, we begin with the derivation of magnetic phase shift from a sample's vector potential.

An important point to note here is that an electron propagates in the z direction in a TEM experiment and images are obtained in the x–y plane. Therefore, integrals will be taken along the z direction and tilts will be performed around the x and the y axes.

The forward projection of the vector potential, $\mathbf{A}(\mathbf{r})$, to yield the magnetic phase shift measurements, $\varphi_m(\mathbf{r}_\perp)$, begins by considering the second term of the A-B phase shift, as expressed in eq. 2.3 :

$$\varphi_m(\mathbf{r}_\perp) = -\int_{-\infty}^{\infty} \mathbf{A}(\mathbf{r}) \cdot d\mathbf{l}. \tag{4.18}$$

Unlike scalar tomography, the VFET approach requires projections from two tilt series to reconstruct all the components of the vector potential. This statement will become apparent in next subsection where we discuss on backprojection technique. Nonetheless, acquisition of the projections in two different directions means that one obtains two sets of magnetic phase shift sinogram. One for the x tilt series, $\varphi_{m,x}$, and the other for the y tilt series, $\varphi_{m,y}$. Let us begin by determining $\varphi_{m,x}$. Derivation of $\varphi_{m,x}$ is analogous to the derivation of T_θ in the 2D vector tomography. The only difference is that each $\varphi_{m,x}$ is a plane whereas each T_θ is a line.

First, define the counter-clockwise rotation matrix, $R_{\theta,x}$, for x tilt as :

$$R_{\theta,x} = \begin{bmatrix} 1 & 0 & 0 \\ 0 & \cos(\theta) & -\sin(\theta) \\ 0 & \sin(\theta) & \cos(\theta) \end{bmatrix}.$$

Also, define a new co-ordinate system $t = (u, v, w)$ such that:

$$r = \begin{bmatrix} x \\ y \\ z \end{bmatrix} = R_{\theta,x} \begin{bmatrix} u \\ v \\ w \end{bmatrix} = R_{\theta,x} t. \tag{4.19}$$

(a)   (b)
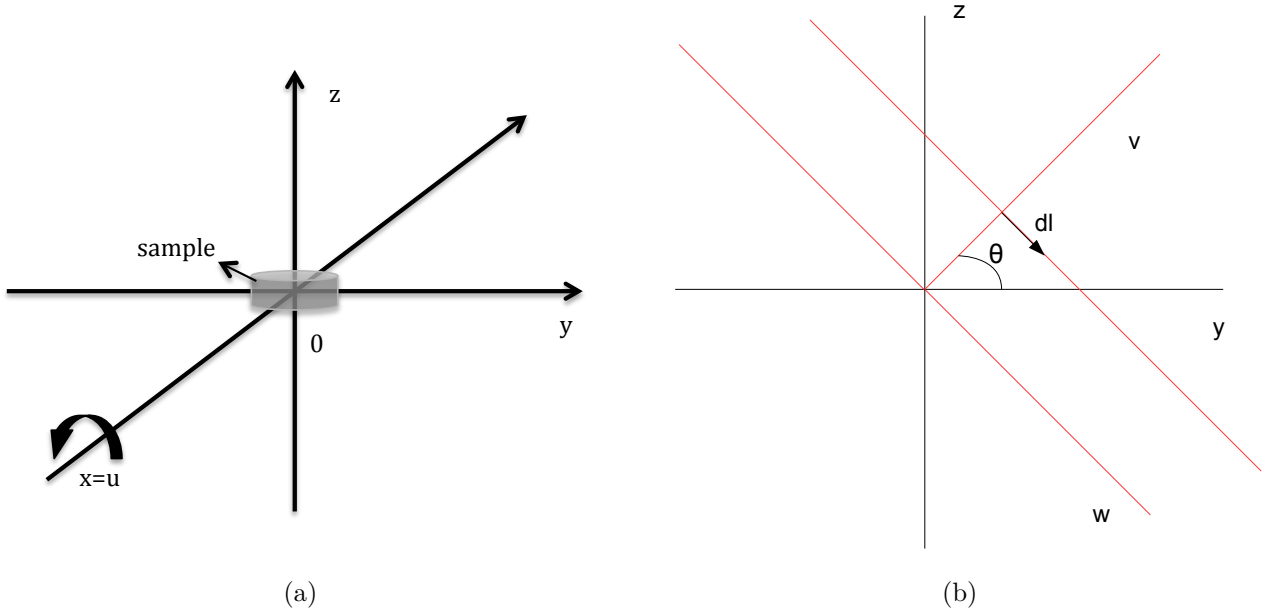
Figure 4.4: (a) Initial reference frame for the acquisition of $\varphi_{m,x}$ with the curved arrow denoting the x tilt direction. (b) Old reference frame, $(*, y, z)$, in terms of the new reference frame, $(*, v, w)$, for each plane in the x direction.

Here, $d\mathbf{l}$ is the vectorial element of the projection line $L(v, \theta)$ as shown in figure 4.4b. Mathematically, $d\mathbf{l}$ can be written as:

$$d\mathbf{l} = \hat{y} \sin(\theta) dl - \hat{z} \cos(\theta) dl.$$

Now, the projection integral for each (x, v) and θ is given by:

$$\varphi_{m,x}(x,v) \;=\; -\int_{-\infty}^{\infty} \mathbf{A}(\mathbf{r}) \cdot d\mathbf{l}$$

$$= \; -\sin(\theta)\int_{-\infty}^{\infty} A_y(r)dl + \cos(\theta)\int_{-\infty}^{\infty} A_z(r)dl$$

$$= \; -\sin(\theta)\int_{-\infty}^{\infty} A_y(R_{\theta,x}t)dl + \cos(\theta)\int_{-\infty}^{\infty} A_z(R_{\theta,x}t)dl$$

$$= \; -\sin(\theta)\int_{-\infty}^{\infty} A_y(\cos(\theta)v - \sin(\theta)w, \sin(\theta)v + \cos(\theta)w)dl$$

$$+\cos(\theta)\int_{-\infty}^{\infty} A_z(\cos(\theta)v - \sin(\theta)w, \sin(\theta)v + \cos(\theta)w))dl. \quad (4.20)$$

Eq. 4.20 represents the radon transform of the magnetic vector potential for the x tilt series. It can also be expressed in the Fourier space by extending the Fourier Slice Theorem in Appendix A to the 3D case in the following manner [60]:

$$\tilde{\varphi}_{m,x}(k_x, k_v) \;=\; \tilde{\varphi}_{m,x}(k_u, k_v)$$

$$= \int_{-\infty}^{\infty} \varphi_{m,x,\theta}(u,v)e^{-2\pi i(k_u u + k_v v)}dudv$$

$$= \; -\int_{-\infty}^{\infty}\sin(\theta)\int_{-\infty}^{\infty} A_y(R_{\theta,x}t)e^{-2\pi i(k_u u + k_v v)}dudvdl$$

$$+\int_{-\infty}^{\infty}\cos(\theta)\int_{-\infty}^{\infty} A_z(R_{\theta,x}t)e^{-2\pi i(k_u u + k_v v)}dudvdl$$

$$= \; -\int_{-\infty}^{\infty}\sin(\theta)\int_{-\infty}^{\infty} A_y(x,y,z)e^{-2\pi i(xk_u + yk_v\cos(\theta) + zk_v\sin(\theta))}dxdydz$$

$$+\int_{-\infty}^{\infty}\cos(\theta)\int_{-\infty}^{\infty} A_x(x,y,z)e^{-2\pi i(xk_u + yk_v\cos(\theta) + zk_v\sin(\theta))}dxdydz$$

$$= \; -\sin(\theta)\tilde{A}_y(k_u, k_v\cos(\theta), k_v\sin(\theta)) + \cos(\theta)\tilde{A}_z(k_u, k_v\cos(\theta), k_v\sin(\theta)). \quad (4.21)$$

A similar analysis for the sample tilt in y direction, as shown in figure 4.5, will deduce the magnetic phase shift, $\varphi_{m,y}$, in the Fourier space to be:

(a)   (b)
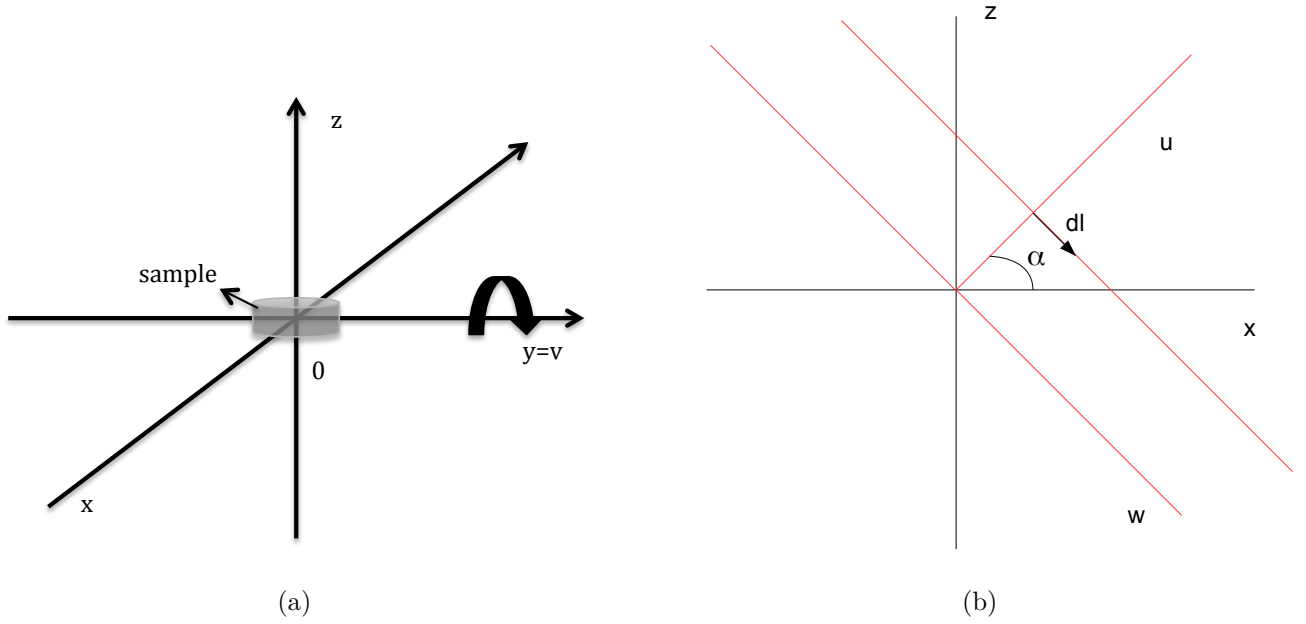
Figure 4.5: (a) Initial reference frame for the acquisition of $\varphi_{m,y}$ with the curved arrow denoting the y tilt direction. (b) Old reference frame, $(x, *, z)$, in terms of the new reference frame, $(u, *, w)$, for each plane in the y direction.

$$\tilde{\varphi}_{m,y}(k_u, k_v) = -\sin(\alpha)\tilde{A}_x(k_u\cos(\alpha), k_v, k_u\sin(\alpha)) + \cos(\alpha)\tilde{A}_z(k_u\cos(\alpha), k_v, k_u\sin(\alpha)).$$
$$(4.22)$$

In order to show an implementation using the forward projection model of the magnetic vector potential, we considered a spherical magnetic nanoparticle of radius, $R = 30$ nm. It has magnetization direction, $\hat{\mathbf{m}} = (\cos(\frac{\pi}{6}), \sin(\frac{\pi}{6}), 0)$ and saturation induction, $B_o = 1$T. Its theoretical magnetic vector potential in Fourier Space is given by [61]:

$$\tilde{\mathbf{A}}(\mathbf{k}) = \frac{iB_o}{k^2}\tilde{D}(\mathbf{k})(\hat{\mathbf{m}} \times \mathbf{k}),$$

where $\tilde{D}(\mathbf{k})$ denotes the shape amplitude of the sphere and $k^2 = k_x^2 + k_y^2 + k_z^2$.

The magnetic phase shift values of the spherical nanoparticle (NP) for the two tilts are calculated using eqs. 4.21 and 4.22. Some of the results from the forward projection of the spherical NP are depicted in figure 4.6.

This completes the forward projection of the vector potential to deduce the projection measurements, $\varphi_{m,x}$ and $\varphi_{m,y}$. Now, our objective will be to reconstruct all three components of the magnetic vector potential with the aid of $\varphi_{m,x}$ and $\varphi_{m,y}$. This will be completed by performing tomographic inversion which is covered in the next subsection.

4.2.2 Filtered Backprojection to reconstruct magnetic vector potential

Similar to the cases of the reconstructions pertaining to the scalar tomography, the reconstructions related to the vector tomography will also make use of the backprojection methodology. However, the backprojection framework of the vector tomography differs from that of the scalar tomography as backprojection of the vectorial projections should resolve three components instead of one. Accordingly, we modify backprojection model from chapter 3 to fully resolve $\mathbf{A}(\mathbf{r})$. In particular, the vector backprojection framework will process sinograms from two different tilt series to resolve two out of the three components of $\mathbf{A}(\mathbf{r})$. Then the third component is retrieved by imposing the Coulomb gauge condition $\nabla \cdot \mathbf{A} = 0$, which in the Fourier space becomes [62]:
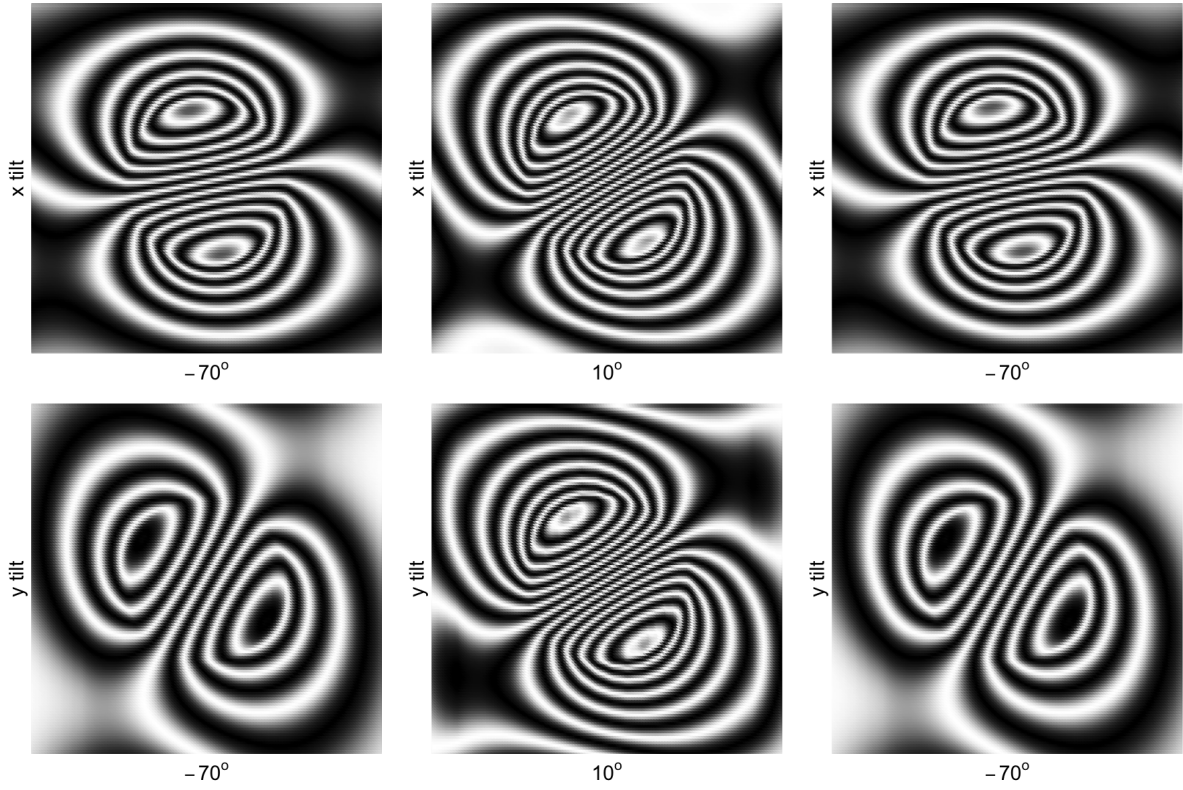
Figure 4.6: Holographic contour plots of the magnetic phase shits, $\varphi_{m,x}(x,y)$ and $\varphi_{m,y}(x,y)$, obtained from the forward projection of the nanoparticle through the x tilt series and the y tilt series respectively. The angle of inclinations are $-70°$, $10°$ and $70°$.

$$\mathbf{k'} \cdot \tilde{\mathbf{A}} = k'_u \tilde{A}_x + k'_v \tilde{A}_y + k'_w \tilde{A}_z = 0. \tag{4.23}$$

Now, the relation between $\mathbf{A}(\mathbf{r})$ and its projections, $\varphi_{m,x}$ and $\varphi_{m,y}$, can be written in the matrix form using eqs. 4.21, 4.22, and 4.23 as:

$$
\begin{bmatrix}
0 & -\sin(\theta) & \cos(\theta) \\
-\sin(\theta) & 0 & \cos(\theta) \\
k'_u & k'_v & k'_w
\end{bmatrix}
\begin{bmatrix}
\tilde{A}_x \\
\tilde{A}_y \\
\tilde{A}_z
\end{bmatrix}
=
\begin{bmatrix}
\tilde{\varphi}_{m,x} \\
\tilde{\varphi}_{m,y} \\
0
\end{bmatrix}. \tag{4.24}
$$

Eq. 4.24 also reveals as to why it was insisted to acquire projections from the two different tilt series. It is of the form $M\tilde{\mathbf{A}} = \tilde{\boldsymbol{\varphi}}_m$. Hence, solving for $\tilde{\mathbf{A}}$ requires inversion of matrix M such that:

$$
\begin{aligned}
\tilde{\mathbf{A}} \quad &= \quad M^{-1}\tilde{\boldsymbol{\varphi}}_m \\
&= \frac{1}{\beta}
\begin{bmatrix}
k'_v \cos(\alpha) & -k'_v \cos(\theta) - k'_w \sin(\theta) & \cos(\alpha)\sin(\theta) \\
-k'_u \cos(\alpha) - k'_w \sin(\alpha) & k'_u \cos(\theta) & \cos(\theta)\sin(\alpha) \\
k'_v \sin(\alpha) & k'_u \sin(\theta) & \sin(\alpha)\sin(\theta)
\end{bmatrix}
\begin{bmatrix}
\tilde{\varphi}_{m,x} \\
\tilde{\varphi}_{m,y} \\
0
\end{bmatrix}, \quad \tag{4.25}
\end{aligned}
$$

where, $\beta = \sin(\theta)\{k'_u \cos(\alpha) + k'_w \sin(\alpha)\} + k'_v \sin(\alpha)\cos(\theta)$.

Realizing the fact that $k'_u = k_u$; $k'_v = k_v \cos(\theta)$; $k'_w = k_v \sin(\theta)$ for the x tilt series, $k'_u = k_u \cos(\alpha)$; $k'_v = k_v$; $k'_w = k_u \sin(\alpha)$ for the y tilt series and substituting these values in eq. 4.25, one obtains:

$$
\begin{aligned}
\tilde{A}_x \quad &= \quad \frac{k'_v k'_u k_v \tilde{\varphi}_{m,x} - k_u((k'_v)^2 + (k'_w)^2 \tilde{\varphi}_{m,y}}{k'_w((k'_u)^2 + (k'_v)^2 + (k'_w)^2)} \\
&= \quad \frac{\cos(\theta)k_u k_v}{\sin(\theta)(k_u^2 + k_v^2)}\tilde{\varphi}_{m,x} - \frac{(k_v^2 + k_u^2 \sin(\alpha))}{\sin(\alpha)(k_u^2 + k_v^2)}\tilde{\varphi}_{m,y}, \quad \tag{4.26}
\end{aligned}
$$

$$
\begin{aligned}
\tilde{A}_y \quad &= \quad \frac{-((k'_u)^2 + (k'_w)^2)k_v \tilde{\varphi}_{m,x} + k_v k'_u k'_v \tilde{\varphi}_{m,y}}{k'_w((k'_u)^2 + (k'_v)^2 + (k'_w)^2)} \\
&= \quad -\frac{(k_u^2 + k_v^2 \sin^2(\theta))}{\sin(\theta)(k_u^2 + k_v^2)}\tilde{\varphi}_{m,x} + \frac{k_u k_v \cos(\alpha)}{\sin(\alpha)(k_u^2 + k_v^2)}\tilde{\varphi}_{m,y}, \quad \tag{4.27}
\end{aligned}
$$

$$\begin{aligned}
\tilde{A}_z &= \frac{k_v' k_w' k_v \tilde{\varphi}_{m,x} - k_u k_u' k_w' \tilde{\varphi}_{m,y}}{k_w'((k_u')^2 + (k_v')^2 + (k_w')^2)} \\
&= \frac{k_v^2 \cos(\theta)}{(k_u^2 + k_v^2)} \tilde{\varphi}_{m,x} + \frac{k_u^2 \cos(\alpha)}{(k_u^2 + k_v^2)} \tilde{\varphi}_{m,y}.
\end{aligned} \tag{4.28}$$

Eqs. 4.26, 4.27, and 4.28 suggests that the angles for the projection acquisition for the x tilt and the y tilt can be dissimilar. However, from the practical standpoint, the final reconstruction is more accurate if the angles of projections are the same for the two tilts and are properly aligned. For the same reason, we proceed by considering $\alpha = \theta$. Now, the only remaining part is to transform the projections, (x, y, θ), from the polar space to the Cartesian space, (x, y, z). This task is completed by performing the smearing/backprojection operation - as discussed in section 3.1.2 - in combination with eqs. 4.26, 4.27, and 4.28. Additionally, absolute value functions $|k_v|$ and $|k_u|$ are used to filter the projection data in the Fourier space for the x tilt series and the y tilt series respectively. Considering all these details, the final filtered backprojection formulae [47, 62, 34] to reconstruct $\mathbf{A}(\mathbf{r})$ results in (the asterisk subscript represent x, y, or z):

$$A_*(x, y, z) = \int_0^\pi \varphi_{m,x,*}(x, y\cos(\theta) + z\sin(\theta)) + \varphi_{m,y,*}(x\cos(\theta) + z\sin(\theta), y)d\theta, \tag{4.29}$$

where,

$$\varphi_{m,x,*} = \mathcal{F}^{-1}\left[\frac{|k_v|}{\sin(\theta)(k_u^2 + k_v^2)}\begin{bmatrix} k_u k_v \cos(\theta) \\ -(k_u^2 + k_v^2 \sin(\theta)) \\ k_v^2 \cos(\theta)\sin(\theta) \end{bmatrix} \tilde{\varphi}_{m,x}(k_u, k_v)\right] = \begin{bmatrix} \varphi_{m,x,x} \\ \varphi_{m,x,y} \\ \varphi_{m,x,z} \end{bmatrix}, \tag{4.30}$$

$$\varphi_{m,y,*} = \mathcal{F}^{-1}\left[\frac{|k_u|}{\sin(\theta)(k_u^2 + k_v^2)}\begin{bmatrix} -(k_v^2 + k_u^2 \sin(\theta)) \\ k_u k_v \cos(\theta) \\ k_u^2 \cos(\theta)\sin(\theta) \end{bmatrix} \tilde{\varphi}_{m,y}(k_u, k_v)\right] = \begin{bmatrix} \varphi_{m,y,x} \\ \varphi_{m,y,y} \\ \varphi_{m,y,z} \end{bmatrix}. \tag{4.31}$$

A VFET based pseudo code to reconstruct A_x from $\varphi_{m,x}$ and $\varphi_{m,y}$ is provided in algorithm 4.1. The same algorithm can be used to deduce A_y and A_z.

Algorithm 4.1 VFET approach to reconstruct A_x.

- For θ in angles

  1. Fourier transform the projections, $\varphi_{m,x}$ and $\varphi_{m,y}$, such that:
  $$\tilde{\varphi}_{m,x}(k_u, k_v) = \mathcal{F}(\tilde{\varphi}_{m,x}(x, y)),$$
  $$\tilde{\varphi}_{m,y}(k_u, k_v) = \mathcal{F}(\tilde{\varphi}_{m,y}(x, y)).$$

  2. Multiply the Fourier transformed projections from (1) by the Ram-Lak filter such that:
  $$\tilde{\varphi}_{m,x}(k_u, k_v) = |k_v|\tilde{\varphi}_{m,x}(k_u, k_v),$$
  $$\tilde{\varphi}_{m,y}(k_u, k_v) = |k_u|\tilde{\varphi}_{m,y}(k_u, k_v).$$

  3. Retrieve the contribution of A_x in each of the tilts in the following manner:
  $$\tilde{\varphi}_{m,x,x}(k_u, k_v) = \frac{k_u k_v \cos(\theta)}{\sin(\theta)(k_u^2 + k_v^2)}\tilde{\varphi}_{m,x}(k_u, k_v),$$
  $$\tilde{\varphi}_{m,y,x}(k_u, k_v) = -\frac{(k_v^2 + k_u^2 \sin(\theta))}{\sin(\theta)(k_u^2 + k_v^2)}\tilde{\varphi}_{m,y}(k_u, k_v).$$

  4. Perform the inverse Fourier Transform of the result from the pervious step such that:
  $$\varphi_{m,x,x}(x, y) = \mathcal{F}^{-1}(\tilde{\varphi}_{m,x}(k_u, k_v)),$$
  $$\varphi_{m,y,x}(x, y) = \mathcal{F}^{-1}(\tilde{\varphi}_{m,y}(k_u, k_v)).$$

  5. Evaluate, $A_x(x, y, z)+ = \varphi_{m,x,x}(x, y\cos\theta + z\sin\theta) + \varphi_{m,y,x}(x\cos(\theta) + z\sin(\theta), y)$.

- End

  $$A_x(x, y, z) = \frac{\pi}{N_{\text{angles}}} A_x(x, y, z).$$
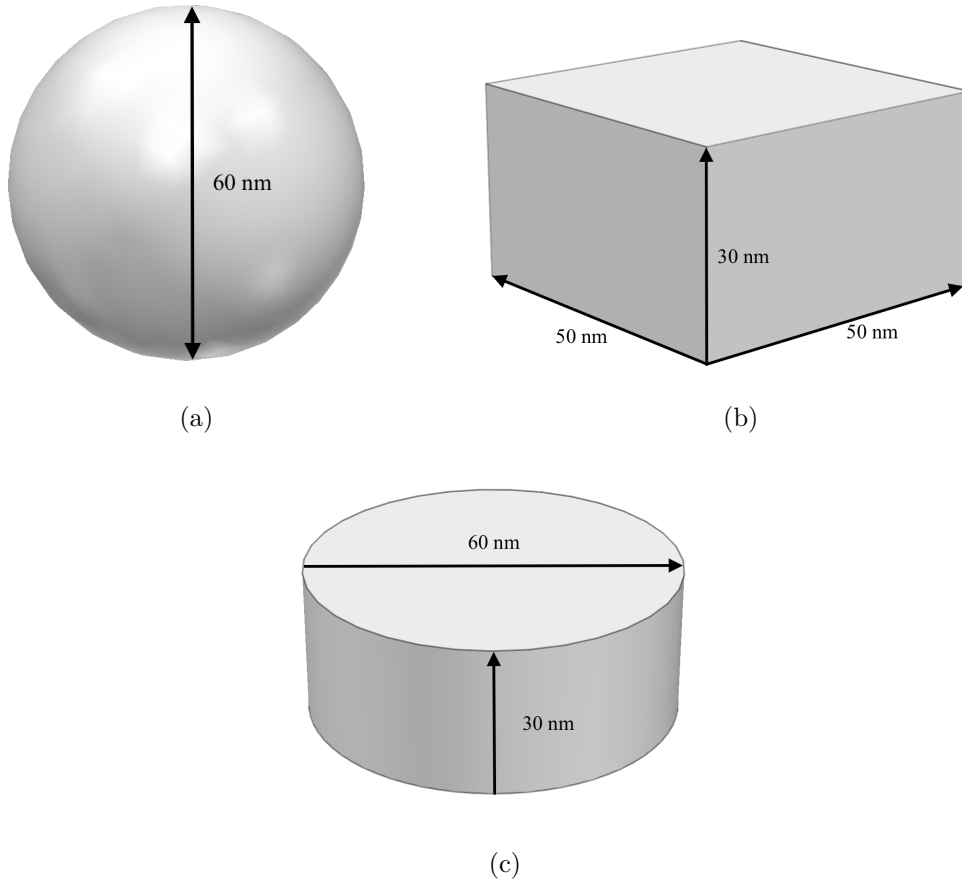
Figure 4.7: (a) Spherical Magnetic Nanoparticle (MNP) with diameter of 60 nm. (b) Prismatic MNP with lateral dimensions of [50 × 50] nm and thickness of 30 nm. (c) Cylindrical MNP with diameter of 60 nm and thickness of 30 nm. (c)
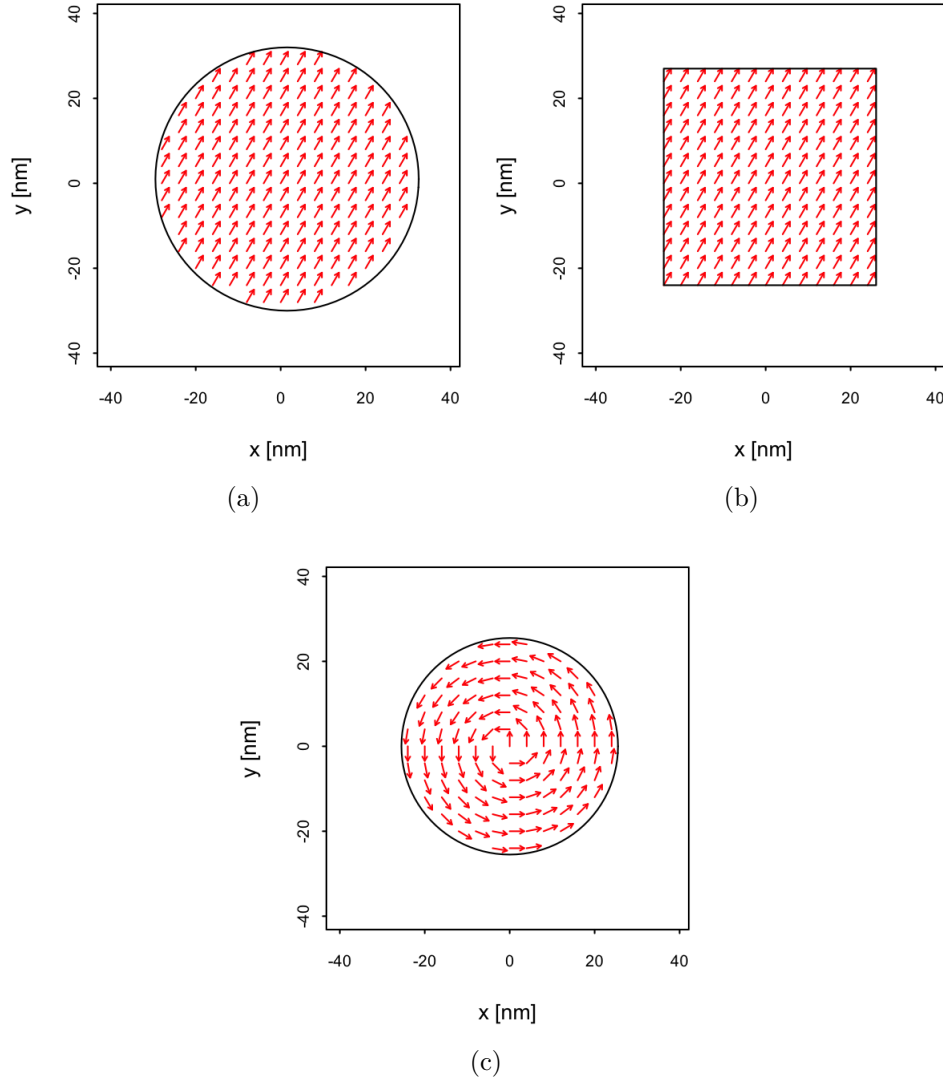
Figure 4.8: Vector plot illustrating (a) uniform magnetization of each z plane of the spherical MNP (4.7a) due to magnetization direction, $\hat{\mathbf{m}} = [\cos\frac{\pi}{6}, \sin\frac{\pi}{6}, 0]$, (b) uniform magnetization of each z plane of the prismatic MNP (4.7b) due to magnetization direction, $\hat{\mathbf{m}} = [\cos\frac{\pi}{6}, \sin\frac{\pi}{6}, 0]$, and (c) counter-clockwise magnetization direction of each z plane of cylindrical MNP (4.7c).

We move on to show numerical implementations from the VFET approach. We make use of simulated/synthetic magnetic nanoparticles (MNPs) that are uniformly and non-uniformly magnetized. In particular, we use sphere and prism as uniformly magnetized and circular disk as non-uniformly magnetized particles. The spherical nanoparticle (NP) has diameter of 60 nm and prismatic NP has dimensions of $[50 \times 50 \times 30]$ nm. Both of them have magnetization direction, $\mathbf{m}$, of $\left[\cos \frac{\pi}{6}, \sin \frac{\pi}{6}, 0\right]$ along each z plane. Likewise, the circular disk has diameter of 60 nm, height of 30 nm, and exhibits counter clock wise magnetization with sharp vortex [61, 63] along each z plane. All three have saturation magnetization, B_o, of 1T. The three NP samples with their corresponding magnetizations are depicted in figures 4.7 and 4.8 respectively.

Next, we determine projection measurements of vector potential of the NPs in x and y tilt series using eqs. 4.21 and 4.22. Moreover, we calculate two sets of measurements for each tilt series. First set, namely full range, comprises of projections in the range $[-90°, +90°]$ at a 2° step size while second set, namely missing wedge, includes projections in the range of $[-70°, +70°]$, again, at a 2° step size. Subsequently, we implement the VFET approach to, separately, resolve vector potential from the two data sets and compare the reconstructed results with their corresponding ground truths. These comparisons were performed by the means of normalized root mean squared error (NRMSE) between reconstructed result, $\hat{y}$, and ground truth, y, as [64]:

$$\text{NRMSE} = \frac{1}{\hat{y}_{\max} - \hat{y}_{\min}} \sqrt{\frac{\sum\limits_{i=1}^{n} (\hat{y}_i - y_i)^2}{n}},$$

where n is the total number of points.

Some of the results retrieved from the two projection data sets and their corresponding ground truths are illustrated in figure 4.9. The main purpose of this implementation is to provide readers with a firsthand glimpse of the effect of limited angular range - gently broached in section 3.3 - on the level of reconstruction using the VFET approach. The qualitative comparisons in figure 4.9. alludes that blurring of edges, protrusions and ring artifacts are more prominent in the reconstruction determined from the missing wedge set than the ones derived from the full range set. The diminishing effect of downsizing the range of angular projection on the level of reconstruct is, further, corroborated by the
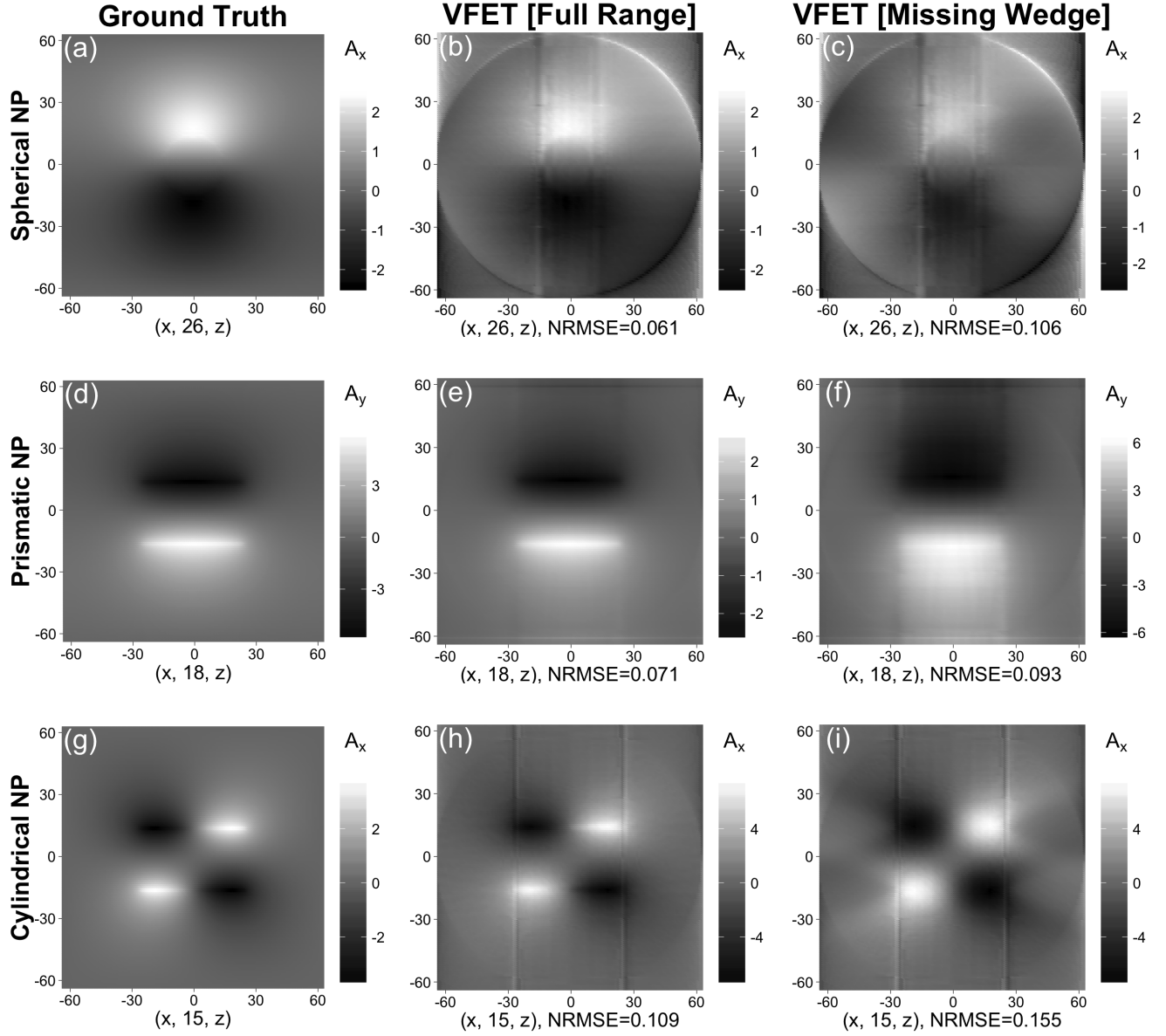
Figure 4.9: Reconstructed magnetic vector potential from full range [center column] and missing wedge [rightmost column] projection data sets. The leftmost column depicts ground truth or theoretical vector components. The top row plots correspond to plane $(x, 26, z)$ of spherical NP, the center row plots correspond to plane $(x, 18, z)$ of prismatic NP and bottom row plots correspond to plane $(x, 15, z)$ of cylindrical NP.
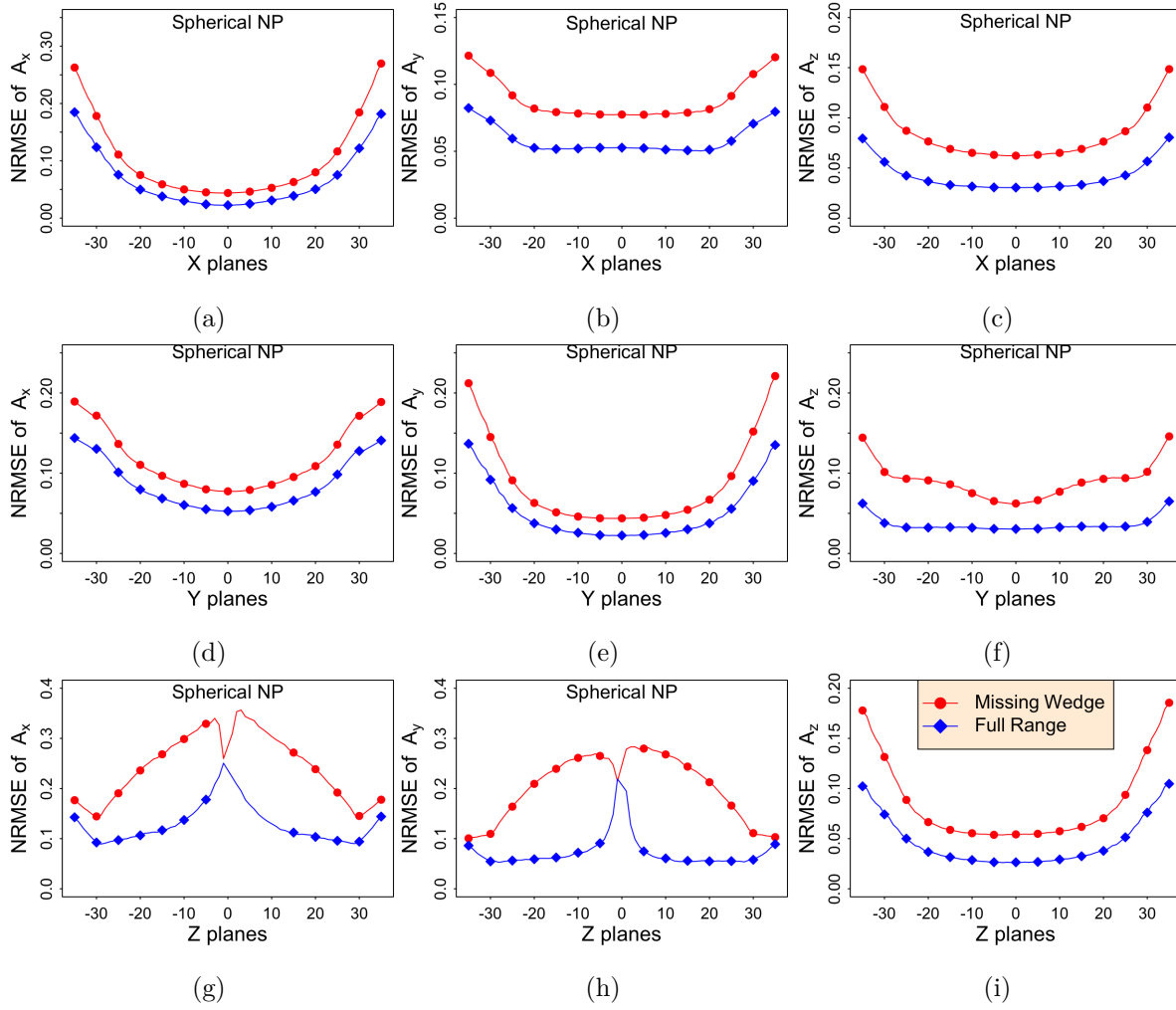
Figure 4.10: Planar NRMSE plots of magnetic vector potential of spherical NP retrieved using the VFET approach on the missing wedge projection set (line with circle) and the full range projection set (line with diamond).
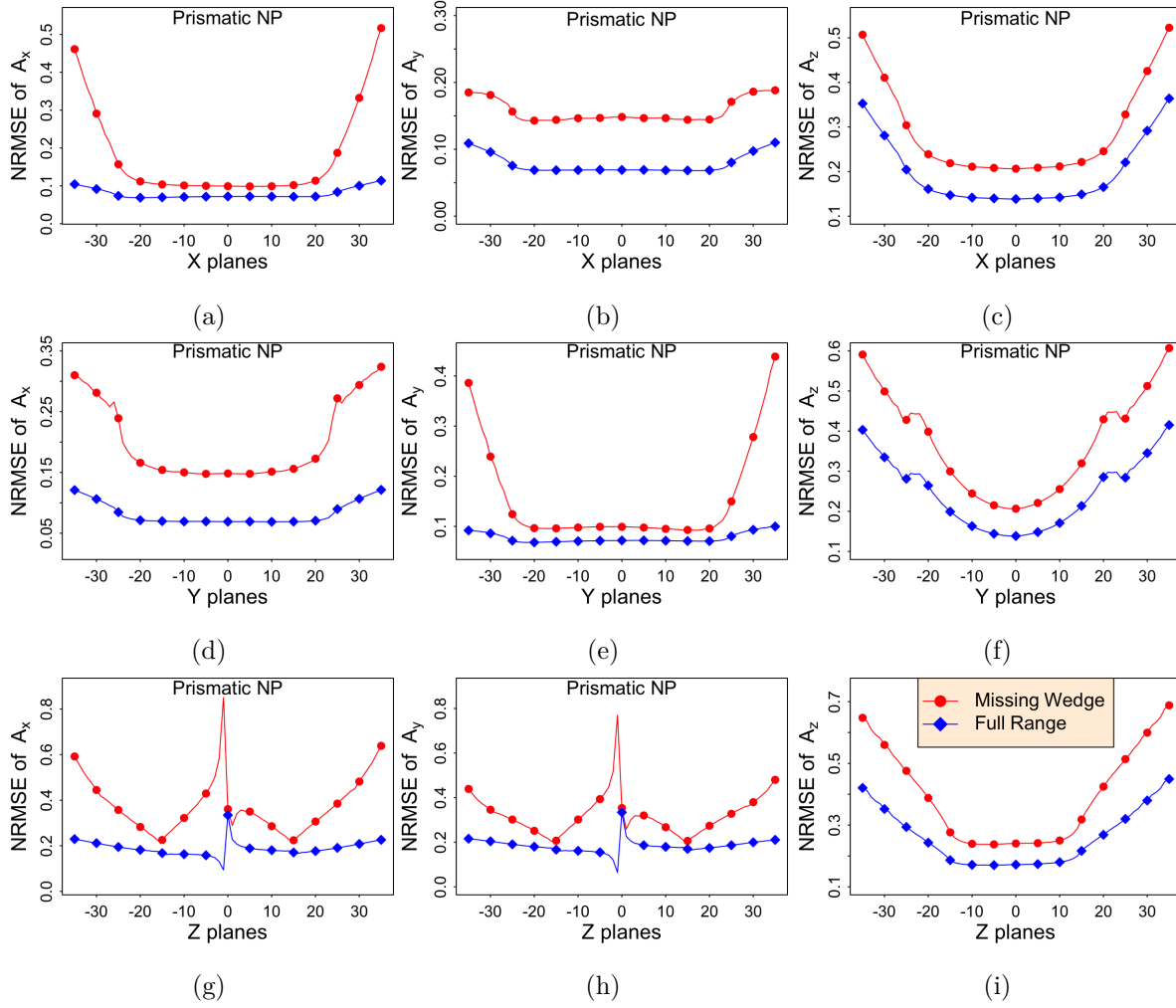
Figure 4.11: Planar NRMSE plots of magnetic vector potential of Prismatic NP retrieved using the VFET approach on the missing wedge projection set (line with circle) and the full range projection set (line with diamond).
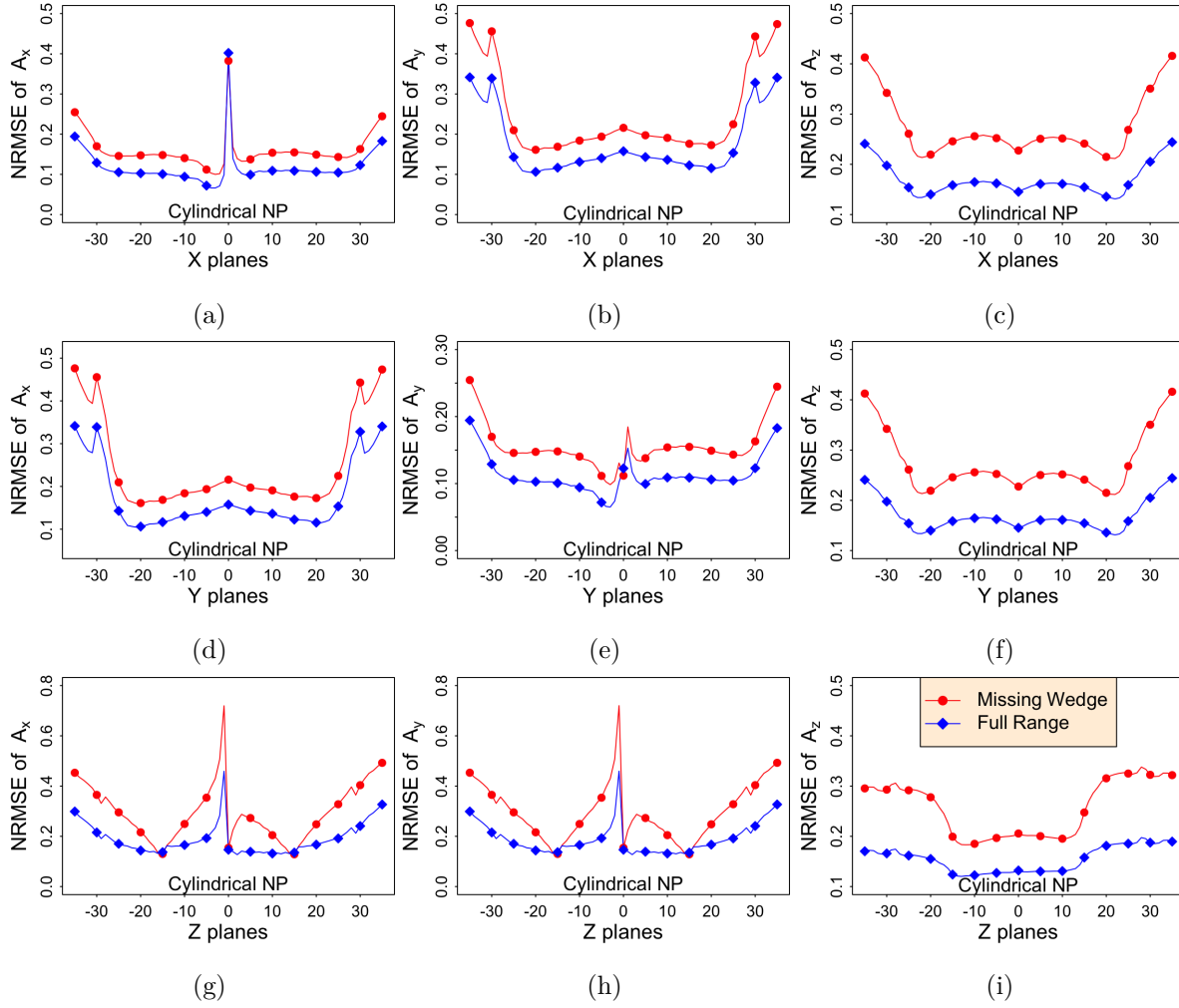
Figure 4.12: Planar NRMSE plots of magnetic vector potential of Cylindrical NP retrieved using the VFET approach on the missing wedge projection set (line with circle) and the full range projection set (line with diamond).

NRMSE planar plot in figures 4.10 - 4.12. The NRMSE corresponds to x, y, and z planes in the range $[-35, 35]$. These plots indicate that the reconstruction deduced from the missing wedge projection set exhibits higher level deviation from the ground truth than its full range counterpart by about $5-30\%$. In addition, one can easily infer that the reconstruction deviates more from its theoretical values in case of the prismatic NP (figure 4.11) - that consists of edges - than the spherical NP (figure 4.10). This discrepancy exacerbates, further, for the reconstruction pertaining to NP that exhibit non-uniform magnetization (figure 4.12) when compared to the ones with uniform magnetization (figures 4.10, 4.11).

The VFET approach is based on the conventional tomography method called filtered backprojection (FBP) and only incorporates filter in its framework. Therefore, it is unable to properly compensate for missing wedge phenomenon in experimental-type incomplete measurements. Likewise, the VFET methodology does not account for the other important factors such as, level of noise in the datasets, what particular type of statistical distribution does the measurement exhibit. Also, its framework does not allow us to incorporate any prior knowledge of the system that we might know beforehand. All these shortcomings of the VFET approach have motivated us to seek a more sophisticated tomographic method model called Model Based Iterative Reconstruction (MBIR). The MBIR approach is based on Bayesian inference and hence, we project that it will resolve $\mathbf{A}(\mathbf{r})$ at a higher accuracy than that deduced from the VFET methodology.

The discourse of proving our claim about the MBIR approach to resolve $\mathbf{A}(\mathbf{r})$ begins by first laying out the basics and the framework of this methodology in the next chapter. Subsequently, we incorporate the MBIR technique to tomographically reconstruct vector potential of simulated as well as experimental datasets and make valuable assertions about our claim.

Chapter 5

MAP estimate: A Bayesian Inference

Bayesian inference is a statistical method that is based on Bayes' theorem. It allows us to update the probability for a hypothesis as more information becomes available. It is very effective in defining the notion of probability for an uncertain event that cannot be repeated numerous times [65]. For instance, consider an uncertain event of whether or not Real Madrid, last year's winner, will win this year's UEFA champions cup. At the moment, two clubs (including Real Madrid) remain in this tournament. With this information, one would guess that there is a fifty percent chance of Real Madrid winning the cup. However, with the aid of Bayesian inference, one can consider the fact that ever since the rebranding of UEFA champions league in 1992, no club has won the cup in consecutive years to statistically come to a conclusion that it is most likely that Real Madrid will not win this year's cup. Here, in the light of new information, we used Bayesian analysis to revise our initial uncertainty and subsequently attempted to give a more optimal prediction [65, 66]. Such elegant interpretation of probability has made Bayesian statistic a great tool to solve problems related to diverse areas such as, science, philosophy, medicine, engineering etc.

In this chapter we elucidate on the statistical framework of maximum a posteriori (MAP) estimate with the aid of the Bayesian probability. The implementation of this framework is illustrated with the help of de-noising and de-blurring analysis.

5.1   Bayes' theorem

Bayes' theorem, originally stated by Reverend Thomas Bayes, provides an equation to update our belief of initial hypothesis when a new piece of evidence becomes available [67]. We incorporate our assumption, before observing the data, in the form of prior probability as $p(x)$. The effect of observed data is expressed through the conditional probability, $p(y/x)$. Then, using Bayes' theorem, the uncertainty in x after having observed the data is relayed in the form of posterior probability, $p(x/y)$ as [68]:

$$p(x/y) = \frac{p(x) \times p(y/x)}{p(y)}. \tag{5.1}$$

The quantity $p(y/x)$ is also called likelihood function. It expresses how probable the observed data, y, is for a particular setting of x. There are two fundamentally different approaches that one can adhere to from here onwards. These are, the frequentist route and the Bayesian route. In the frequentist paradigm, probabilities represent long run frequencies of events. The validation across the repeated trials forms the basis for modeling the uncertainty in the frequentist approach [69]. A widely used frequentist estimator is maximum likelihood, in which x is set such that the value of $p(y/x)$ is maximized. In various optimization procedures, maximizing the likelihood function equates as taking negative log of the function. Accordingly, the negative log is determined to systematically minimize error observed in our measurements.

However, if one were to perform fair coin toss three times and land head each time, frequentist interpretation would imply that the future coin tosses would also land head. It clearly shows the limitation of the frequentist viewpoint and this is where the Bayesian viewpoint comes into play. In the bayesian paradigm, we only consider the observed data and there is no notion of repeated trials [69]. Moreover, as stated before, prior knowledge is incorporated and is revised as a posteriori in the light of new evidence. In our interpretation of Bayes' theorem, we take a mid way approach by incorporating the idea of the Bayesian as well as the frequentist viewpoints. We determine a posteriori for the likelihood function that has been maximized. In other words, we maximize the a posteriori. This technique is called maximum a posteriori (MAP) estimate [70]. An operation that guarantees the maximization of any function is taking logarithm. Hence,

MAP can be mathematically expressed as:

$$
\begin{aligned}
\text{MAP} &= \arg \max\{p(x/y)\}, \\
&= \arg \max\{\log p(y/x) + \log p(x) - \log p(y)\}.
\end{aligned}
$$

Since the term $p(y)$ does not depend on x or does not communicate any information on prior, it is dropped from the optimization. Thus, the resulting MAP estimate expression comes out to be:

$$
\begin{aligned}
\text{MAP} &= \arg \max\{\log p(y/x) + \log p(x)\} \\
&= \arg \min\{-\log p(y/x) - \log p(x)\}.
\end{aligned} \tag{5.2}
$$

This concludes a general overview of the Bayes' theorem and how we seek to utilize the Bayesian analysis. In the next section, we implement the Bayesian inference to clean up a noisy data set via deducing its MAP estimate.

5.2 MAP restoration from a noisy measurement

In this section we will explore the use of the MAP estimation to extract a clean data from its correponding noisy data. The measured data, Y, has been corrupted by additive Gaussian noise, W. Hence, the noiseless image, X, is related to the noisy image in the following manner:

$$
Y = X + W, \tag{5.3}
$$

where each random variable of the Gaussian noise is assumed to be independent and identically distributed (i.i.d). Likewise, the parameters for the Gaussian noise consist of the mean as 0 and the variance as σ_w^2.

Our aim is to deduce as close of an approximation of X as possible. The estimation of X is completed by adhering to an analysis comprised of three parts. The first part is the prior model formulation. Here, we model the distribution of the image before acquiring the

data based on our prior information. In particular, quadratic and non-quadratic Gaussian Markov Random Field (MRF) are incorporated in the prior model formulation. The second part consists of the noise model. Here, we incorporate the probability distribution of the noise exhibited by the image data. The final part comprises of the MAP estimate. The MAP estimation part is completed by performing a coordinate descent minimization of a cost function called iterative coordinate descent (ICD). A thorough account on each of the aforementioned aspects to determine the MAP estimate is provided under the following headings:

5.2.1 Prior model

We begin by considering a random field, X, defined on a set of N points. Each pixel X_s, for $s \, \epsilon \, S$, takes on a $\mathbb{R}^+$. Furthermore, X is assumed to be a Markov Random Field (MRF). This assumption comes directly from widely observed application of MRF to solve similar problems [71, 72, 73, 74]. In particular, MRF's ability to preserve the intricacies of an image through its local neighborhood operations makes it a powerful tool to estimate the clean image [70]. Similarly, the noisy data is assumed to have positive valued measurement as in the cases of various practical based application. With the assumption of X to be MRF with strictly positive density, the Hammersley-Clifford theorem states that it must have the form of a Gibbs distribution [75, 76]. Likewise, we assume that the Gibbs distribution for X uses two nearest neighbor interactions or pairwise cliques [70] such that:

$$\mathcal{C} = \{\{i,j\}|i \, \epsilon \, \partial j \text{ for } i,j \, \epsilon \, S\},$$

where ∂j denotes the neighbors of i. A depiction of MRF is shown in figure 5.1. The Gibbs density of the MRF is assumed to have the following form [3]:

$$p(x) = \frac{1}{z} \exp \left\{ -\sum_{c \, \epsilon \, \mathcal{C}} V_c(x_c) \right\}, \tag{5.4}$$

where z is a normalizing constant known as the partition function, x_c is the vector containing values of x on the set of cliques $c \, \epsilon \, \mathcal{C}$, and $V_c(x_c)$ is any functions of x_c. Sometimes
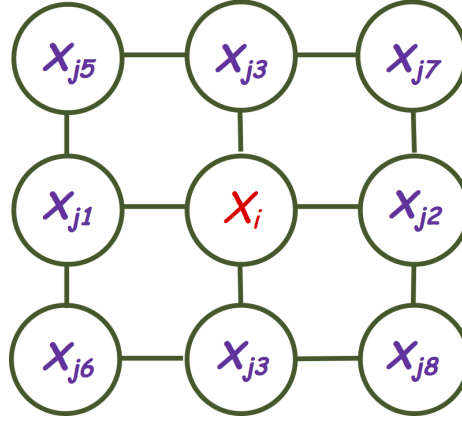
Figure 5.1: An illustration of Markov Random field (MRF) of a pixel X_i in the neighborhood of X_{j*}. Here, two nearest neighbors are taken into the consideration with $X_{j,1-4}$ as the first nearest neighbors and $X_{j,5-8}$ as the second nearest neighbors.

the function $V_c(x_c)$ is also referred as a potential function. Here, we will use a class of MRF known as generalized Gaussian MRF (GGMRF) to model the potential function such that [77, 78, 79]:

$$
\begin{aligned}
p(x) &= \frac{1}{z(g,p,\sigma_x)} \exp\left\{-\frac{1}{p\sigma_x^p} \sum_{\{i,j\}\,\epsilon\,\mathcal{C}} g_{i,j}|x_i - x_j|^p\right\} \\
&= \frac{1}{z(g,p,1)\sigma_x^N} \exp\left\{-\frac{1}{p\sigma_x^p} \sum_{\{i,j\}\,\epsilon\,\mathcal{C}} g_{i,j}|x_i - x_j|^p\right\} \qquad (5.5)
\end{aligned}
$$

In eq. 5.5, the potential function, $|\Delta|^p$, acts on pairs of pixels with $1 \leq p \leq 2$. The choice of p is critical in coping with the edges of images. When $p = 2$, the potential function penalizes large differences in neighboring pixels, and so sharp edges are discouraged. On the other hand, when $p = 1$ sharp edges are no more costly than smooth edges. Thus, fine edges are preserved in the image [70]. We deduce the MAP estimates making use of the Gaussian and the non-Gaussian MRF prior models to depict the aforementioned effect on edges with the choice of a particular value of p. Likewise, σ_x is the variance of the Gibbs distribution. Finally, $g_{i,j}$ is a noncausal weighing filter that is symmetric and is normalized such that:

$$\sum_{j \epsilon \partial j} g_{i,j} = 1.$$

5.2.2   Noise model

We use noise model to formulate the likelihood part while determining the MAP estimate of the clean image. Given that W is i.i.d with 0 mean, the likelihood term for N data points can be expressed as:

$$
\begin{aligned}
p(y/x) &= \prod_{i \, \epsilon \, S} \frac{1}{(2\pi\sigma_w^2)^{1/2}} \exp\left\{-\frac{(y_i - x_i)^2}{2\sigma_w^2}\right\} \\
&= \frac{1}{(2\pi\sigma_w^2)^{N/2}} \exp\left\{-\frac{1}{2\sigma_w^2}\sum_{i \, \epsilon \, S}(y_i - x_i)^2\right\}.
\end{aligned}
\tag{5.6}
$$

5.2.3   MAP estimate and cost function

The joint probability distribution of the prior and the likelihood parts formulate posterior probability. The posterior probability can be maximized in accordance to eq. 5.2 to determine the MAP estimate of x as:

$$\hat{x} = \operatorname*{argmin}_{x}\left\{\frac{1}{2\sigma_w^2}\sum_{i \, \epsilon \, S}(y_i - x_i)^2 + \frac{1}{p\sigma_x^p}\sum_{\{i,j\} \, \epsilon \, \mathcal{C}} g_{i,j}|x_i - x_j|^p\right\}. \tag{5.7}$$

Thus, the cost function to be minimized comes out to be:

$$c(x) = \frac{1}{2\sigma_w^2}\sum_{i \, \epsilon \, S}(y_i - x_i)^2 + \frac{1}{p\sigma_x^p}\sum_{\{i,j\} \, \epsilon \, \mathcal{C}} g_{i,j}|x_i - x_j|^p. \tag{5.8}$$

From eq. 5.7 it is clear that the cost function has to be minimized to compute the estimate. However, if the optimization does not achieve the exact global minimum, then the resulting MAP estimate is unstable. Thus, compromising the quality of the solution. One particular route to ensure a stable MAP estimate is to check if the cost function is convex in nature or not. Convexity of the MAP cost function, $c(x)$, will ensure the existence, uniqueness, and stability of the MAP estimate. Moreover, a strictly convex cost function for each x_i in its neighborhood of MRF will ensure that its optimization will

yield a global minimum that is unique [3, 80, 81]. With this in our mind, let us check if our cost function in eq. 5.8 is truly a convex function. First, differentiating both sizes of eq. 5.8, one gets:

$$\frac{\partial c(x)}{\partial x_i} = \frac{1}{\sigma_w^2}\sum_{i \in S}(x_i - y_i) + \frac{1}{\sigma_x^p}\sum_{\{i,j\} \in C} g_{i,j}|x_i - x_j|^{p-1}\text{sign}(x_i - x_j). \tag{5.9}$$

Likewise, the second derivative of the cost function with respect to x_i gives:

$$\begin{aligned}
\frac{\partial^2 c(x)}{\partial x_i^2} &= \frac{1}{\sigma_w^2}\sum_{i \in S}1 + \frac{1}{\sigma_x^p}\sum_{\{i,j\} \in C} g_{i,j}|x_i - x_j|^{p-2} \\
&> 0. \tag{5.10}
\end{aligned}$$

The result in inequality 5.10 confirms that the cost function in eq. 5.8 is indeed strictly convex in nature. Consequently, the minimization of the cost function yields a globally minimum and a stable MAP solution. This concludes our analysis on the cost function. We proceed to elucidate on a gradient decent method called iterative coordinate decent (ICD) to minimize the cost function.

5.2.4 Iterative Coordinate Descent (ICD)

Let us consider the case of the Gaussian MRF prior ($p = 2$) such that the cost function of each pixel can be expressed as:

$$c(x_i) = \frac{1}{2\sigma_w^2}\sum_{i \in S}(y_i - x_i)^2 + \frac{1}{2\sigma_x^2}\sum_{\{i,j\} \in C} g_{i,j}(x_i - x_j)^2. \tag{5.11}$$

Now, the ICD [82] techique comes into the picture by sequentially minimizing the cost function of 5.11 with respect to each pixel in each iteration. Accordingly, differentiating the expression in eq. 5.11 and solving for the minimum x_i yields:

$$\frac{\partial c(x_i)}{\partial x_i} = \frac{y_i - x_i}{\sigma_w^2}.(-1) - \frac{1}{\sigma_x^2}\sum g_{i,j}(x_i - x_j) \overset{set}{=} 0;$$

$$\Rightarrow x_i + \frac{\sigma_w^2}{\sigma_x^2}\sum g_{i,j}x_i = y_i + \frac{\sigma_w^2}{\sigma_x^2}\sum g_{i,j}x_j;$$

$$\Rightarrow x_i = \frac{y_i + \frac{\sigma_w^2}{\sigma_x^2} \sum g x_j}{(1 + \frac{\sigma_w^2}{\sigma_x^2})}. \tag{5.12}$$

Eq. 5.12 determines how the ICD methodology updates each pixel for each iteration. Additionally, the ICD updates form a monotone decrease sequence. This statement can be proven by the method of induction. $\forall\, i$ s.t. $i \in S$, $x_{i,2} - x_{i,1} = -\frac{\sigma_w^2}{\sigma_x^2} \sum g_{i,j}(x_{i,2} + x_{i,1}) < 0 \Rightarrow x_{i,2} < x_{i,1}$. Here $x_{i,1}$ and $x_{i,2}$ are values of the pixel x_i in the first and second iteration respectively. Now, suppose that the monotone decreasing sequence of the ICD is true until the kth iteration s.t. $x_{i,k} < x_{i,k-1}$. Next, for $(k+1)^{th}$ iteration, one gets:
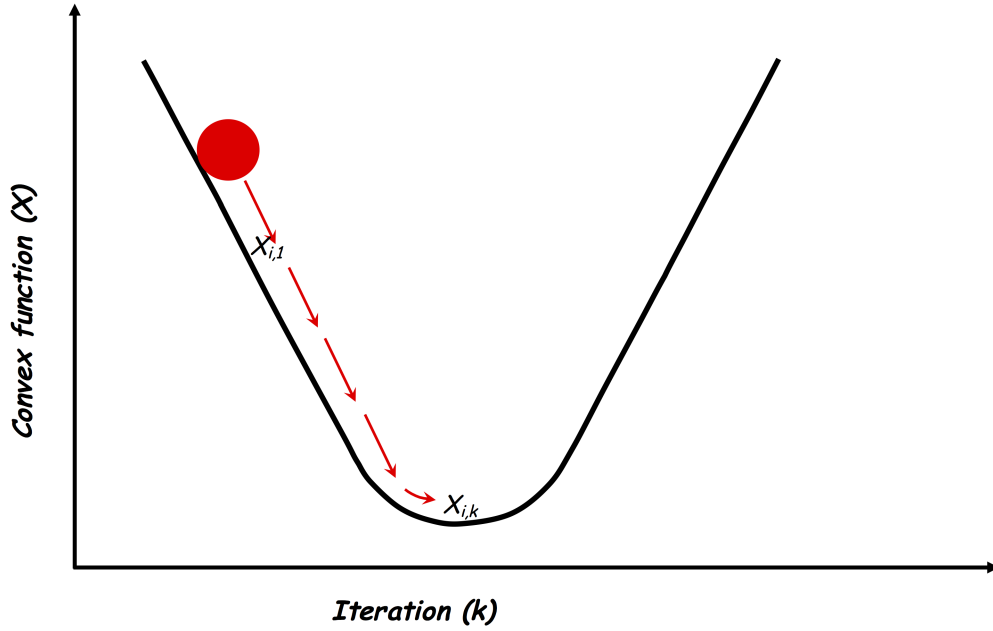
Figure 5.2: Schematic of determining minimum of a convex function using iterative coordinate descent (ICD) technique.

$$
\begin{aligned}
x_{i,(k+1)} - x_{i,k} &= \frac{\sigma_w^2}{\sigma_x^2}\{-\sum g_{i,j}(x_{i,(k+1)} - x_j) + \sum g_{i,j}(x_{i,k} - x_j)\} \\
&= \frac{\sigma_w^2}{\sigma_x^2}\{-\sum g(x_{i,k} + x_{i,(k+1)})\} \\
&< 0.
\end{aligned}
$$

(a)

(b)
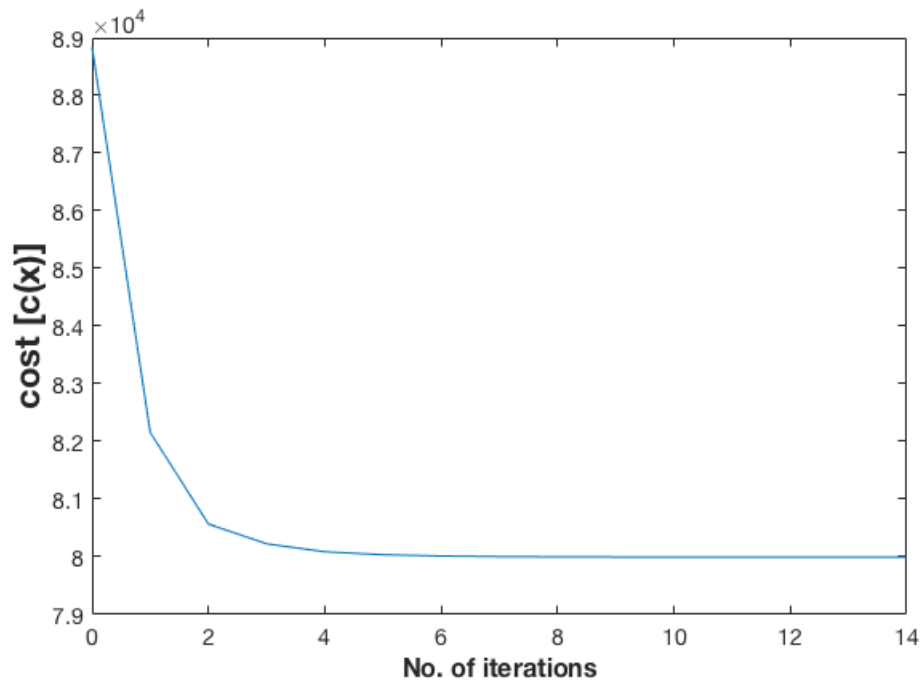
(c)

Figure 5.3: (a) Noisy image with additive Gaussian noise of $\sigma_w^2 = 16^2$. (b) MAP estimate of X using Gaussian prior model. (c) Illustration of minimization of the cost function using the ICD technique.

Hence, proving the fact that the ICD updates indeed form a monotonically decreasing sequence while minimizing the cost function. This attribute of ICD is visually depicted in figure 5.2. Finally, the ICD update is completed by imposing the constraint that each pixel takes on only the positive values as elucidated in algorithm 5.2.

The only parameters that are yet to be declared to determine the MAP estimate are the variances of the Gaussian and the Gibbs distributions. An experimentalist, usually, has a good insight into the level of noise in the measurements. Accordingly, depending upon the nature of the problem and the measurement, the variance for either prior or noise model is assigned. Still, one may encounter cases where the variance of neither of the two models be remotely known or could be gauged from the past measurements. In such scenario, the joint posterior distribution can be optimized with respect to the variance to deduce its estimate. For instance, the maximum likelihood estimator for the scale parameter σ_x for the GGMRF comes out to be:

$$\hat{\sigma}_x^p = \frac{1}{N} \sum_{\{i,j\} \epsilon \mathcal{C}} g_{i,j} |x_i - x_j|^p.$$

Having defined the statistical framework and the parameters required to determined the MAP estimate of X, we now proceed to show the implementation of the framework. For the same purpose, consider the variance of the Gaussian noise in the measurement, Y, to be 16^2 (figure 5.3a). Next, following the pseudo codes to perform the ICD of the cost function - delineated in algorithm 5.2 - we determine the MAP estimate of X. Thus obtained result is depicted in figure 5.3b. Likewise, decay of the cost as the iteration proceeds is depicted in figure 5.3c. The MAP estimate clearly shows that the initial noise in figure 5.3a has been subdued. However, traces of coarseness are still event in the estimate. For the same reason, we will now proceed to deduce the MAP estimate with non-Gaussian prior model (i.e. $p \neq 2$) and verify that choosing the value of p closer to 1 indeed improves the quality of the estimate.

5.2.5   MAP estimate with non-Gaussian prior

A non-Gaussian MRF prior model requires us to minimize the quantity in eq. 5.8 for values of p other than 2. In particular, it involves solving for x_i in the eq. 5.9. This

expression cannot be solved directly by means of analytical method. Consequently, we have to make use of some numerical methods.

One particular technique that has been around to solve a problem of such nature is the Newton-Raphson method or the line search method [3]. In this method, we numerically estimate the minima of the convex function, $c(x_i)$, with respect to the pixel, x_i, within the pixel's neighborhood of the MRF. In addition, we can adopt either half interval line-search method or bisection method to solve for x_i in the interval, $[a, b]$ where, $a = \text{minimum}\{x_i, x_j \text{ for } j \, \epsilon \, \partial j\}$ and $b = \text{maximum}\{x_i, x_j \text{ for } j \, \epsilon \, \partial j\}$. A pseudo code to implement the bisection method is provided in algorithm 5.1.

Algorithm 5.1 Bisection Method

- Initialize a and b so that $c'(a) \cdot c'(b) \leq 0$.

- diff $= \text{abs}(c'(b) - c'(a))$.

- While (diff > threshold) {

  $m \leftarrow (a + b)/2$.

  If $c'(m) \leq 0$, then $a \leftarrow m$.

  If $c'(m) > 0$, then $b \leftarrow m$.

  diff $= \text{abs}(c'(b) - c'(a))$.

  }

It is not difficult to infer that minimizing the cost function using the Newton-Raphson method is computationally expensive to implement. For the same reason, we resort to a different method called majorization technique. The majorization technique allows nonquadratic optimization problems to be converted into iterative quadratic optimization [3, 83]. More specifically, we replace the potential function, $\rho(\Delta)$ where, $\rho(\Delta) = |\Delta|^p$, by a simpler quadratic surrogate/substitution function, $\rho(\Delta; \Delta')$, such that the minimum of both the functions corresponds to the same x_i in their respective codomains [84, 85]. A depiction of this procedure is shown in figure 5.4. A more detailed analysis on surrogate functions and its derivations can be found elsewhere in reference [3]. Nonetheless, below
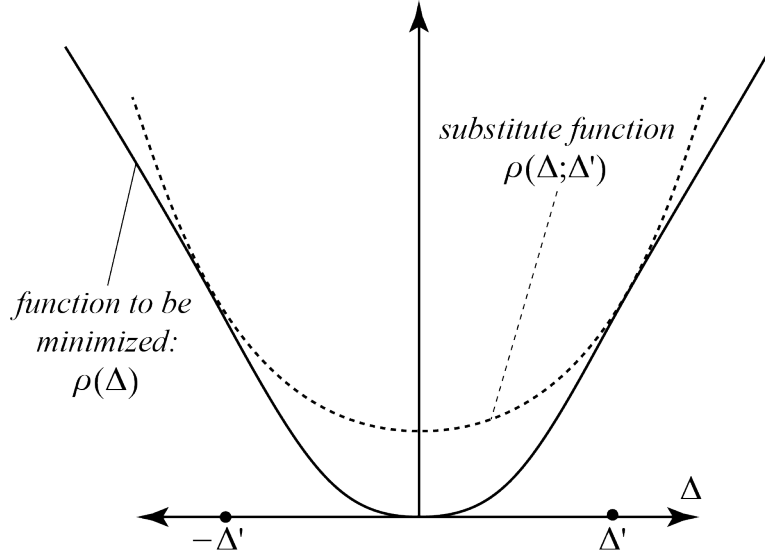
Figure 5.4: A depiction of the intuition behind the formulation of the substitute function of the non-quadratic potential function [3].

are the final results for the symmetric bound surrogate function:

$$\rho(\Delta; \Delta') = \begin{cases} \frac{\rho'(\Delta')}{2\Delta'}\Delta^2 & \text{if } \Delta' \neq 0, \\ \frac{\rho''(0)}{2}\Delta^2 & \text{if } \Delta' = 0. \end{cases} \tag{5.13}$$

Again referring to table 7.1 in reference [3], one finds the corresponding surrogate function for q-Generalized Gaussian Markov Random Field (q-GGMRF) to be:

$$\frac{\rho'(\Delta')}{2\Delta'} = \frac{|\Delta|^{p-2}}{2\sigma_x^p} \frac{\left|\frac{\Delta}{T\sigma_x}\right|^{q-p}\left(\frac{q}{p} + \left|\frac{\Delta}{T\sigma_x}\right|^{q-p}\right)}{\left(1 + \left|\frac{\Delta}{T\sigma_x}\right|^{q-p}\right)^2}, \tag{5.14}$$

$$\frac{\rho''(0)}{2} = \frac{1}{p\sigma_x^p} \text{ for } q = 2.$$

Having determined the surrogate potential function, $\rho(\Delta; \Delta')$, we can proceed to construct a surrogate MAP cost function in the following manner [3]:

$$c(x; x') = \frac{1}{2\sigma_w^2} \cdot (y_i - x_i)^2 + \sum g_{i,j} \rho(x_i - x_j; x_i' - x_j')$$

$$= \frac{1}{2\sigma_w^2} \cdot (y_i - x_i)^2 + \sum \tilde{g}_{i,j} (x_i - x_j)^2, \qquad (5.15)$$

where,

$$\tilde{g}_{i,j} \leftarrow g_{i,j} \frac{|x_i - x_j|^{p-2}}{2\sigma_x^p} \frac{\left|\frac{x_i - x_j}{T\sigma_x}\right|^{q-p} \left(\frac{q}{p} + \left|\frac{x_i - x_j}{T\sigma_x}\right|^{q-p}\right)}{\left(1 + \left|\frac{x_i - x_j}{T\sigma_x}\right|^{q-p}\right)^2} \text{ for } \triangle \neq 0,$$

$$\tilde{g}_{i,j} \leftarrow g_{i,j} \frac{1}{p\sigma_x^p} \text{ for } \triangle = 0, \quad q = 2.$$

Thus derived surrogate cost function can, now, be analytically minimized with respect to x_i to deduce the MAP estimate for the non-Gaussian MFR prior as:

$$x_i = \frac{y_i + 2\sigma_w^2 \sum \tilde{g}_{ij} x_j}{1 + 2\sigma_w^2 \sum \tilde{g}_{ij}}. \qquad (5.16)$$

The pseudo code to determine the MAP estimate for the non-Gaussian prior model has been jointly provided with the Gaussian one in algorithm 5.2. Following the same algorithm, we minimize the cost function for $p = 1.1$ and evaluate the MAP estimate. The result from this implementation is illustrated in figure 5.5. A thorough comparison of the MAP estimates from the Gaussian and the non-Gaussian priors reveals that the result from the later yields an estimate of superior quality. Thus, confirming our initial claim on the choice of p. This confirmation is of great importance to gain an insight for a better edge reconstruction while performing the tomographic reconstruction using the Bayesian statistical framework. A more detailed analysis on the prior model for the tomographic reconstruction will be provided in the next chapter. For now, we proceed to the next section on the Bayesian Framework that is devoted to de-blurring.

5.3 MAP restoration from a blurry and noisy measurement

In this section, we aim to restore a clean image, X, from a measurement that is blurry as well as noisy. The relation between the clean image, and the blurry/noisy measurement can be expressed as:

Algorithm 5.2 ICD Algorithm to de-noise using Gaussian and non-Gaussian prior model

---

- For each $i \, \epsilon \, S$

  $x_i \leftarrow y_i$.

- Select or estimate the values of σ_w and σ_x.

- For k in 1 to K

  1. For each $i \, \epsilon \, S$

     if (Gaussian prior == TRUE){

     $$x_i \leftarrow \max \left\{ 0, \frac{y_i + \frac{\sigma_w^2}{\sigma_x^2} \sum g_{i,j} x_j}{(1 + \frac{\sigma_w^2}{\sigma_x^2})} \right\}$$

     }

     if (non-Gaussian prior == TRUE){

     set $1 < p < 2$ and $q = 2$,

     call_$\tilde{g}_{ij}()$

     $$x_i \leftarrow \max \left\{ 0, \frac{y_i + 2\sigma_w^2 \sum \tilde{g}_{ij} x_j}{1 + 2\sigma_w^2 \sum \tilde{g}_{ij}} \right\}$$

     }

- End

- call_$\tilde{g}_{ij}()${

  if $((x_i - x_j) \neq 0)$ $\tilde{g}_{ij} \leftarrow g_{ij} \frac{|x_i - x_j|^{p-2}}{2\sigma_x^p} \dfrac{\left| \frac{x_i - x_j}{T\sigma_x} \right|^{q-p} \left(\frac{q}{p} + \left| \frac{x_i - x_j}{T\sigma_x} \right|^{q-p} \right)}{\left(1 + \left| \frac{x_i - x_j}{T\sigma_x} \right|^{q-p} \right)^2}$

  else $\tilde{g}_{ij} \leftarrow g_{ij} \frac{1}{p\sigma_x^p}$

  }

(a)

(b)

(c)

Figure 5.5: (a) Noisy image with additive Gaussian noise with $\sigma_w^2 = 16^2$. (b) MAP estimate of X using non-Gaussian prior model with $p = 1.1$. (c) Illustration of minimization of surrogate cost function using the ICD.

$$Y = HX + W, \tag{5.17}$$

where H is a circulant-block-circulant matrix that implements a 2D shift invariant filter applied with circular boundary condition. A particular instance of such matrix could be of the following impulse response [86]:

$$\begin{bmatrix} 1/81 & 2/81 & 3/81 & 2/81 & 1/81 \\ 2/81 & 4/81 & 6/81 & 4/81 & 2/81 \\ 3/81 & 6/81 & 9/81 & 6/81 & 3/81 \\ 2/81 & 4/81 & 6/81 & 4/81 & 2/81 \\ 1/81 & 2/81 & 3/81 & 2/81 & 1/81 \end{bmatrix}.$$

The main reason behind performing the MAP restoration from the blurry and noisy image is due to the problem's resemblance to the tomographic reconstruction problem. More specifically, the set up of the tomography problem is also of the form $Y = A_f X$, where A_f is the forward projection operator and Y is the sinogram measurements. A more detailed description on the tomographic reconstruction using the MAP estimate will be provided in the next chapter. For now, we proceed with the MAP restoration of X from the blurry/noisy image.

First, the prior model for the blurry and noisy measurements is formulated in the similar manner that for the noisy measurements with the aid of eq. 5.5. Moreover, we incorporate the q-GGMRF surrogate potential function from eqs. 5.13 and 5.14 to model the prior distribution such that the cost function can be analytically minimized for the values of p in the range $(1, 2)$. The part where the MAP estimate framework of the de-blurring problem differs from the de-noising problem is the exponential term of the noise model. Due to the blurring kernel, H, the x term of the Gaussian noise distribution in eq. 5.6 gets replace by Hx. Accordingly, the MAP estimate of the blurry image has the form:

$$\hat{x} = \arg \min_{x \geq 0} \left\{ \frac{1}{2\sigma_w^2} ||y - Hx||^2 + \sum_{i,j \epsilon \mathcal{C}} \tilde{g}_{i,j}(x_i - x_j)^2 \right\}, \tag{5.18}$$

where $\tilde{g}_{i,j}$ assumes the same values as in eq. 5.15. Likewise, $x \geq 0$ indicates that the

optimization is performed adhering the fact that the measurements take only positive values. Then the surrogate cost function to be minimized has the form:

$$c(x) = \frac{1}{2\sigma_w^2}||y - Hx||^2 + \sum_{i,j\epsilon\mathcal{C}}\tilde{g}_{i,j}(x_i - x_j)^2. \tag{5.19}$$

Because we iteratively minimizing the cost function, let us define new variables, u and v that represent the updated value and the value from the previous iteration, respectively, for each pixel. Next, define an error vector, $e = y - Hx$, such that the cost function can be written as:

$$
\begin{aligned}
c(u) &= \frac{1}{2\sigma_w^2}||e - H_{*,i}(u - v)||^2 + \frac{1}{2\sigma_x^2}\sum_{i,j\epsilon\mathcal{C}}\tilde{g}_{i,j}(u - x_j)^2 \\
&= \frac{1}{2\sigma_w^2}||e - H_{*,i}\alpha||^2 + \frac{1}{2\sigma_x^2}\sum_{i,j\epsilon\mathcal{C}}\tilde{g}_{i,j}(u - x_j)^2,
\end{aligned} \tag{5.20}
$$

where $H_{*,i}$ indicates the ith column of the matrix H and $\alpha = u - v$. Now, consider the first term of the cost function, $c(u)$, and perform the Taylor series expansion of the term around the point $\alpha = 0$ to get:

$$f(\alpha) = \text{constant} + \frac{-e^t H_{*,i}\alpha}{\sigma_w^2} + \frac{||H_{*,i}||^2\alpha^2}{2\sigma_w^2}. \tag{5.21}$$

Substituting the $f(\alpha)$ term from eq. 5.21 back to eq. 5.20, one gets:

$$c(u) = \text{constant} + \theta_1(u - v) + \frac{1}{2}\theta_2(u - v)^2 + \sum_{i,j\epsilon\mathcal{C}}\tilde{g}_{i,j}(u - x_j)^2.$$

Differentiating the expression w.r.t u and solving for the minimum result, one gets:

$$u = \frac{\theta_2 v - \theta_1 + 2\sum \tilde{g}_{i,j}x_j}{\theta_2 + 2\sum \tilde{g}_{i,j}}, \tag{5.22}$$

where $\theta_1 = \frac{-e^t H_{*,i}}{\sigma_w^2}$, $\theta_2 = \frac{||H_{*,i}||^2}{\sigma_w^2}$ and $\tilde{g}_{i,j}$ assumes the same values as in eq. 5.15.

A summary of the MAP restoration of X from the burry and noisy measurement with the aid of q-GGMRF prior model is elucidated in algorithm 5.3. Following the same pseudo code, we performed the de-blurring analysis of the blurred and noisy image depicted in figure 5.6a. The restored MAP estimate of X is delineated in figure 5.6b.

Likewise, figure 5.6c depicts how the cost function sequentially decreases over the course of the ICD updates.

Algorithm 5.3 ICD Algorithm to de-blurr an image using q-GGMRF surrogate prior model

---

- For each $i \,\epsilon\, S$

  $x_i \leftarrow y_i$

- Select the value for p in the range $(1, 2]$ and set $q = 2$

- Select or estimate the values of σ_w and σ_x

- Initialize $e \leftarrow y - Hx$

- For k in 1 to K

  1. For each $i \,\epsilon\, S$

     $v \leftarrow x_i$

     $\theta_1 \leftarrow \frac{-e^t H_{*,i}}{\sigma_w^2}$

     $\theta_2 \leftarrow \frac{||H_{*,i}||^2}{\sigma_w^2}$

     call$\_\tilde{g}_{ij}()$

     $x_i \leftarrow \max\left\{0, \frac{\theta_2 v - \theta_1 + 2\sum \tilde{g}_{ij} x_j}{\theta_2 + 2\sum \tilde{g}_{ij}}\right\}$

     $e \leftarrow e - H_{*,i}(x_i - v)$

- End

- call$\_\tilde{g}_{ij}()\{$

  if $((x_i - x_j) \neq 0)$ $\tilde{g}_{ij} \leftarrow g_{ij}\frac{|x_i - x_j|^{p-2}}{2\sigma_x^p} \frac{\left|\frac{x_i - x_j}{T\sigma_x}\right|^{q-p}\left(\frac{q}{p} + \left|\frac{x_i - x_j}{T\sigma_x}\right|^{q-p}\right)}{\left(1 + \left|\frac{x_i - x_j}{T\sigma_x}\right|^{q-p}\right)^2}$

  else $\tilde{g}_{ij} \leftarrow g_{ij}\frac{1}{p\sigma_x^p}$

  $\}$
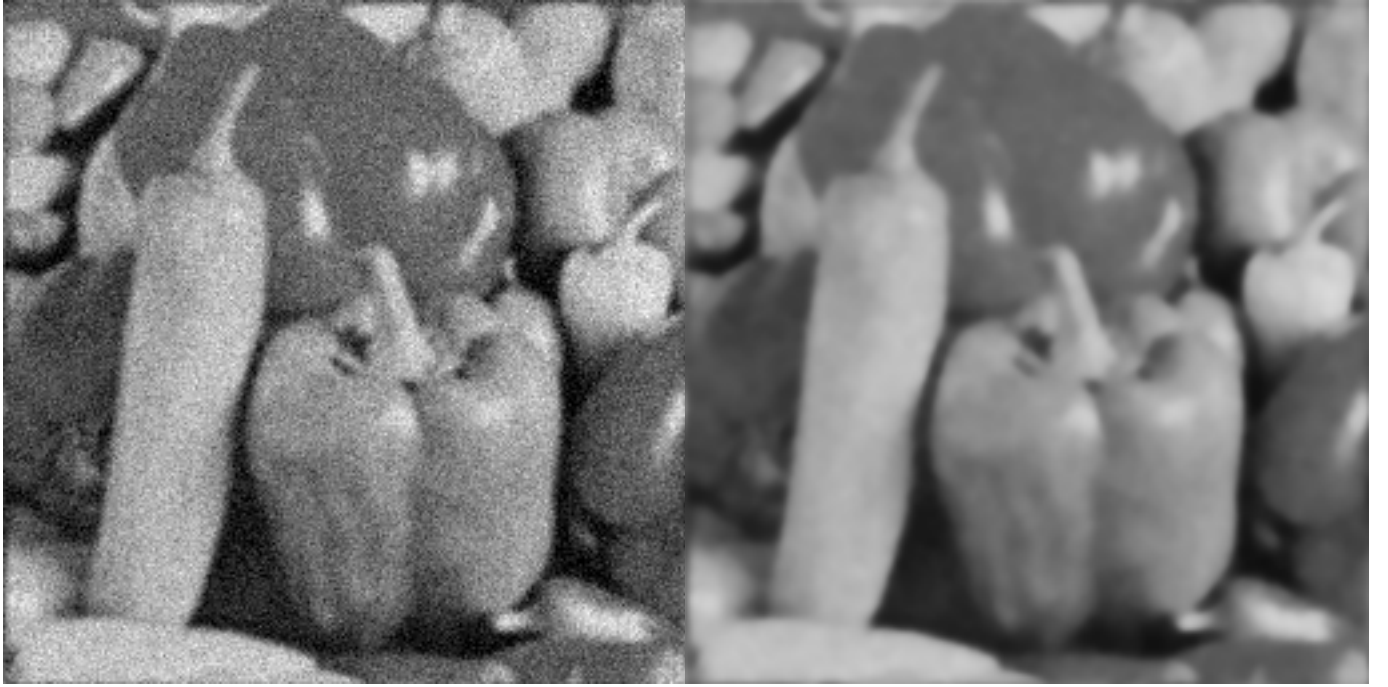
(a)

(b)

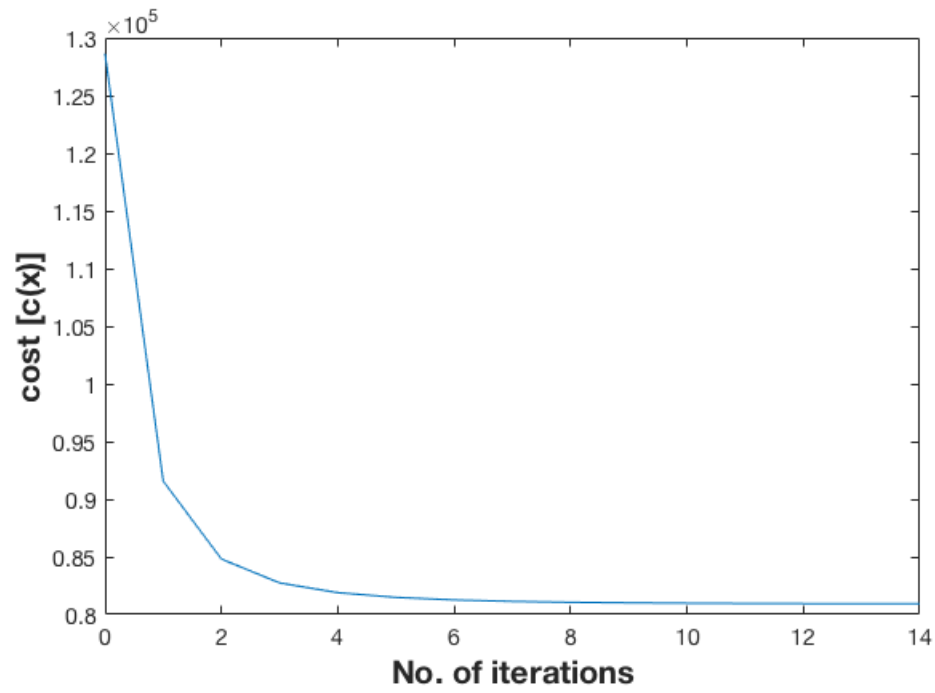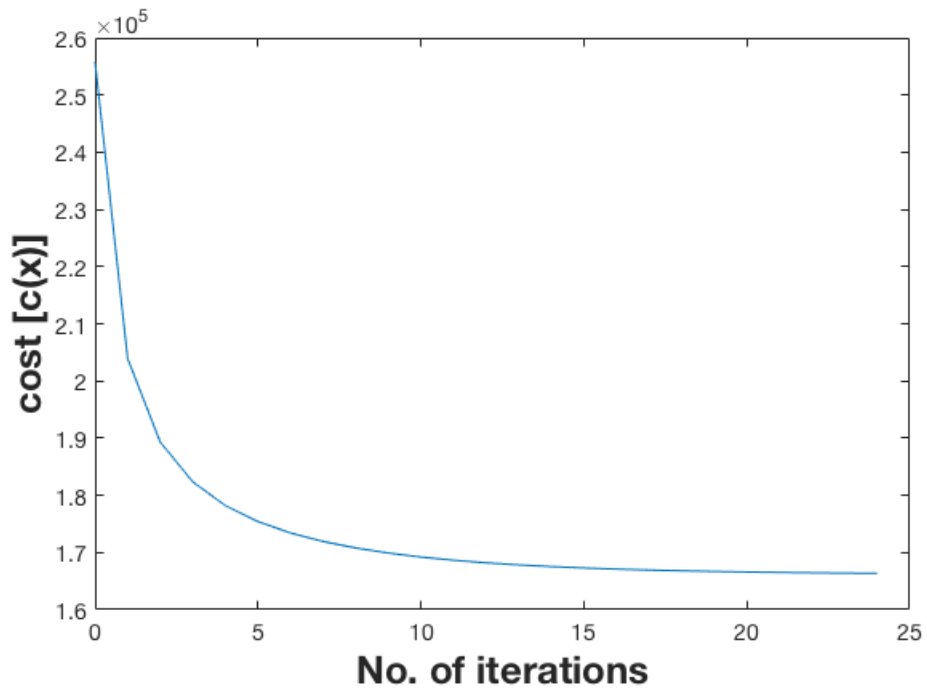(c)

Figure 5.6: (a) Blurry image with additive Gaussian noise ($\sigma_w^2 = 16^2$). (b) MAP estimate of X using q-GGMRF surrogate prior model with $p = 1.1$. (c) Illustration of minimization of surrogate cost function using the ICD techinque.

To sum up, this chapter delineates on how the Bayes' theorem can be used to incorporate the prior information about a system from which the measurements are being obtained. The Bayes' theorem comprises of prior and likelihood terms. The prior part allows us to incorporate valuable a-priori information about the object being studied. Likewise, the likelihood term enables us to model the probability distribution of the observed data conditioned under the assumed prior. The joint probability distribution of the prior and the likelihood probabilities forms the posteriori probability. The posterior probability is iteratively maximized to deduce a most probable estimate. This technique is called maximum a posteriori (MAP) estimate. It turns out that the MAP estimation is determined by minimizing the cost function. For the same reason, the convexity of the cost function is crucial to ascertain the existence, uniqueness and stability of the MAP estimate. Finally, choice of the value of parameter p in the prior model plays a significant role in terms the quality of the MAP restoration. In particular, when the value of p is $1.1, 1.2$ or closer to 1, it is observed that the MAP restoration is more efficient in edge preservation and boundary distinction. However, when the value of $p \neq 2$, the cost function cannot be minimized analytically by the usual calculations. Consequently, we make use of the majorization technique to analytically solve the prior model in which the value of p falls in the range of $(1, 2)$.

This concludes our account on the Bayesian inference to deduce the MAP estimate. In the next chapter, we implement the statistical framework of the MAP estimation technique to resolve tomographic problems. It elucidates on the Bayesian framework for scalar as well as vector reconstructions.

Chapter 6

Tomographic Reconstruction Using MBIR

In chapter 3, we concluded that it is not possible to reconstruct the initial density with cent percent accuracy because of the availability of only a discrete set of projections. Moreover, convectional tomography methods, such as the Filtered Back Projection (FBP) approach, although yield a good estimate with a complete set of projections, the reconstruction is severely underdetermined with an incomplete set of measurements. Likewise, chapter 4 concludes that the reconstruction obtained from the Vector Field Electron Tomography (VFET) approach significantly deviates from the theoretical values due to its inability to compensate for *missing wedge* of information. In view of these findings, we have resorted to adopt a more robust and statistical based tomographic reconstruction framework called Model Based Iterative Reconstruction (MBIR) [3].

Over the years, the MBIR approach has been extensively explored for the scalar reconstruction. The results from the MBIR approach show that it substantially improves the reconstruction quality [87, 88, 89]. Based on the success of the MBIR approach at the scalar interface, we hypothesize that the MBIR technique can overcome the shortcomings of the VFET methodology and resolve the vector reconstruction problem with a high precision all across the spatial region.

In general, the MBIR approach seeks a tomographic solution that best matches the probabilistic behavior of the data. This process is aided by introducing a prior distri-

bution in the framework that reflects the knowledge or beliefs concerning the types of values that are acceptable as estimates of the original sample [90]. The MBIR framework achieves the aforementioned solution via minimizing a cost function dictated by the measurements and the system's prior information [3, 70]. In particular, MBIR updates each pixel in each iteration by minimizing the pixel's associated cost. Eventually, it leads to the determination of a global minimum of the cost function and thereby, deducing the most probable estimate [82].

In this chapter, we first derive a generic statistical framework for the MBIR approach. Then we implement the MBIR technique to resolve a 2D scalar tomography problem. Subsequently, we expand the MBIR method to reconstruct the solenoid part of a 2D vector field. This portion serve as a proof-of-concept that the underdetermined vector tomography results, like scalar tomography based densities, can be improved with the MBIR approach. Finally, we implement the MBIR approach to resolve 3D vector potential problems. Again, we employ the RMSE analysis - as explained in chapter 3 - to perform a direct comparison of results obtained from the VFET approach with those deduced from the MBIR approach. We show our results for simulated as well as experimental datasets.

6.1 Formulation of the MAP estimate for the tomographic reconstruction

Similar to the de-noising and the de-blurring analysis in chapter 5, statistical tomographic reconstruction requires optimization of the cost function derived from the joint probability distribution of the likelihood function and the prior distribution. Accordingly, we begin by assuming that the data measured from the experiment obeys Poisson's distribution. In fact, measurements acquired from TEM experiments - for magnetic vector potential reconstruction - observe Poisson's distribution [35]. Likewise, let sample, x, be of N-dimensional vector and projection data, y, be of M-dimensional vector. Also, define H_{ij} as the probability that an electron transmitted through pixel j is registered in the ith detector. Then the measured data y, as per Poisson distribution with parameter H_{i*}, gives the likelihood function as [88, 90]:

$$\mathcal{P}(Y = y | x) = \prod_{i=1}^{M} \frac{(H_{i,*}x)^{y_i} e^{-H_{i,*}x}}{y_i!}, \tag{6.1}$$

where, H_{i*} is the ith row of the projection matrix. Using the convention, $p_i = H_{i*}x$ and taking the log of the expression, we get:

$$\log \mathcal{P}(y/x) = \sum_{i=1}^{M} y_i \log(p_i) - p_i - \log(y_i!). \tag{6.2}$$

Here, the log likelihood function is differentiable and is strictly convex. Accordingly, the maximum likelihood (ML) estimation of x from y yields the optimization problem to take the form:

$$\begin{aligned} \hat{x}_{ml} &= \arg\min_{x} \sum_{i=1}^{M} (p_i - y_i \log p_i). \\ &= \arg\min_{x} \sum_{i=1}^{M} f(p_i), \end{aligned} \tag{6.3}$$

where, $f(p_i) = p_i - y_i \log p_i$.

Next, we formulate prior model, $p(x)$, and use Bayes' theorem to determine posterior probability. A particular prior model that has proven to be useful in image processing as well as in tomographic reconstruction is the Markov Random Field (MRF) [71, 72, 73, 74]. The success of using MRF stems from the fact that it allows us to establish a correlation between the neighboring pixels [91]. Furthermore, under some weak condition, Hammersley-Clifford states that a random field is a MRF if and only if it forms a Gibbs distribution. Hence, a general form of Gibbs MRF to incorporate the prior model can be mathematically expressed as:

$$p(x) = \frac{1}{z} \exp \left\{ - \sum_{\{j,k\} \epsilon C} b_{jk} \rho(x_j - x_k) \right\}, \tag{6.4}$$

where C is the set of all neighboring pixel pairs, b_{jk} is the element of the noncausal predictor matrix b linking pixels j and k. Here, b is a symmetric matrix and is invariant i.e. same for each pixel j [3, 88]. Likewise, $\rho(\cdot)$ denotes potential function and is of the form $|\Delta|^p$, as shown in expression 5.5 for the case of Generalized Gaussian Markov

Random Field (GGMRF). Now, combining the log of the prior distribution with the maximum likelihood expression in 6.3, we determine the maximum a posteriori (MAP) estimate of the sample, x, in the following manner:

$$\hat{x}_{\text{MAP}} = \operatorname*{argmin}_{x} \left\{ \sum_{i=1}^{M} f(p_i) + \sum_{\{j,k\}\epsilon C} b_{jk}\rho(x_j - x_k) \right\}. \tag{6.5}$$

The expression for the MAP estimate in eq. 6.5 gives the cost function to be:

$$c(x) = \sum_{i=1}^{M} f(p_i) + \sum_{\{j,k\}\epsilon C} b_{jk}\rho(x_j - x_k). \tag{6.6}$$

It can easily be verified that the cost function in eq. 6.6 is strictly convex. The convexity of the cost function allows us to perform Iterative Coordinate Descent (ICD), similar in the manner described in chapter 5, to deduce a MAP estimate that is stable and is globally minimum. Generally, the ICD procedure is initialized with the filtered backprojection result as the starting low cost value for the MAP estimate [88]. This aids in a faster convergence to the global minimum as oppose to initializing the cost function with a random estimate. However, before proceeding straight into the cost minimization task, we first simplify the log likelihood part to facilitate the optimization. In particular, we compute the first two terms of the Taylor series expansion of the log likelihood. Then, the first and the second partial derivatives of the log likelihood term are evaluated at $p = \tilde{p}$ (where, $\tilde{p} = Hx_{\text{FBP}}$) as:

$$f'(\tilde{p}_i) = 1 - \frac{y_i}{\tilde{p}_i}; \tag{6.7}$$

$$f''(\tilde{p}_i) = \frac{y_i}{(\tilde{p}_i)^2}. \tag{6.8}$$

Next, assuming $y > 0$, the Taylor series expansion of $f(\tilde{p})$ at $\tilde{p} = y$ is evaluated to be:

$$\begin{aligned} f(\tilde{p}_i) &= f(y_i) + \frac{f'(y_i)(\tilde{p}_i - y_i)}{1!} + \frac{f''(y_i)(\tilde{p}_i - y_i)^2}{2!} \\ &= \text{constant} + 0 + \frac{(y_i - \tilde{p}_i)^2}{2y_i}. \end{aligned} \tag{6.9}$$

Now we focus on the prior term of the cost function. It has already been established in chapter 5 that the non-quadratic prior model are more equipped to preserve edges than the quadratic prior model (with $p = 2$). However, minimization of the non-quadratic cost function requires implementation of numerical method like Newton-Raphson technique. Since Newton-Raphson method is computationally expensive, we make use of the majorization technique to substitute the non-quadratic cost function with a quadratic function. One can take a look at figure 5.4 to get an insight of how the majorization technique works. Subsequently, the substitute/surrogate cost function, to be minimized, can be expressed as::

$$c(x; x') = \sum_{i=1}^{M} f(\tilde{p}_i) + \sum_{\{j,k\}\epsilon C} b_{jk}\rho(x_j - x_k; x'_j - x'_k). \tag{6.10}$$

As in the case of image processing analysis performed in section 5.2.5, we model the potential function, $\rho(\Delta)$, using q-Generalized Gaussian Markov Random Field (q-GGMRF). Accordingly, referring to table 7.1 in reference [3], the surrogate cost function using q-GGMRF prior model can be expressed as:

$$c(x; x') = \sum_{i=1}^{M} f(\tilde{p}_i) + \sum_{\{j,k\}\epsilon C} \tilde{b}_{jk}(x_j - x_k)^2, \tag{6.11}$$

where,

$$\tilde{b}_{jk} = \begin{cases} b_{jk}\frac{|x'_j-x'_k|^{p-2}}{2\sigma_x^p} \dfrac{\left|\frac{x'_j-x'_k}{T\sigma_x}\right|^{q-p}\left(\frac{q}{p}+\left|\frac{x'_j-x'_k}{T\sigma_x}\right|^{q-p}\right)}{\left(1+\left|\frac{x'_j-x'_k}{T\sigma_x}\right|^{q-p}\right)^2} & \text{for } \Delta \neq 0 \\ \\ b_{jk}\frac{1}{p\sigma_x^p} & \text{for } \Delta = 0 \end{cases}. \tag{6.12}$$

p, q, T, and σ_x are q-GGMRF parameters. In our implementation we set $q = 2$ and $p = 1.001$ to facilitate edge preserving reconstructions. Similarly, σ_x is the variance of the prior distribution and its value is set to achieve a balance between noise and resolution. Finally, the constant T determines the approximate threshold of transition between low and high contrast regions.

The cost function in eq. 6.11 can be minimized using either global or local techniques [70]. For our implementation, we adhere to the ICD [82] approach that locally minimizes

the cost function in each iteration. In view of the local based minimization, the cost function for each pixel, x_j, can be written as:

$$
\begin{aligned}
c(x_j) &= f(\tilde{p}_i) + \sum_{k \epsilon \partial j} b_{jk} \rho(x_j - x_k; x'_j - x'_k) \\
&= \frac{||y_i - H_{i,*}x_j||^2}{2y_i} + \sum_{k \epsilon \partial j} \tilde{b}_{jk}(x_j - x_k)^2 \\
&= ||y_i - H_{i,*}x_j||^2_W + \sum_{k \epsilon \partial j} \tilde{b}_{jk}(x_j - x_k)^2,
\end{aligned}
\tag{6.13}
$$

where $W = \text{diag}\{1/y_1, 1/y_2, \ldots, 1/y_M\}$ and is more popularly known as diagonal noise weighing matrix in tomographic problems. For our implementation we set W as an identity matrix. Subsequently, the cost function in eq. 6.13 can be simplified as:

$$
c(x; x') = \frac{1}{2}||y - Hx||^2 + \sum_{k \epsilon \partial j} \tilde{b}_{jk}(x_j - x_k)^2.
\tag{6.14}
$$

The cost function in eq. 6.14 is quadratic and so its minimum can be expressed in closed form. Accordingly, we proceed to differentiate the surrogate function and solve for minimum x_j to yield each pixel update as:

$$
x_j \leftarrow \frac{H^T y + 2 \sum_{k \epsilon \partial j} \tilde{b}_{jk} x_k}{1 + 2 \sum_{k \epsilon \partial j} \tilde{b}_{jk}}.
\tag{6.15}
$$

This concludes a general overview of tomographic reconstruction using the MAP based framework or the MBIR approach. In the forthcoming sections, we make use of the MBIR technique to perform the 2D and the 3D tomographic reconstruction.

6.2 On 2D interface

In order to computationally incorporate the MBIR approach, we first summarize the theoretical framework of the approach in the form of a pseudo code. The pseudo code is provided in algorithm 6.1. An important point to notice here is that the error sinogram, e, is not updated after each pixel update. However, this is not the case in a typical

---

Algorithm 6.1 Fourier Transform-based MBIR method for scalar tomography

---

- initialize $u \leftarrow \text{FBP}(y)$

- $v \leftarrow H^T y$

- **while** not converged **do**

    for $j = 1$ to N **do**

        for $k\epsilon\partial j$ of u_j determine $\tilde{b}_{jk}$ using eq. 6.12

        $u_j \leftarrow (v_i + 2\sum\limits_{k\epsilon\partial j} \tilde{b}_{jk}u_j)/(1 + 2\sum\limits_{k\epsilon\partial j} \tilde{b}_{jk})$

        end for

    end for

    $e \leftarrow y - Hu$

    $u \leftarrow u + H^T e$

- **end while**

MBIR based scalar reconstruction. Standard MBIR based tomographic reconstruction incorporates forward projection that is entirely calculated in real space. Most importantly, it performs forward projection of a single pixel or a voxel such that the error sinogram can be updated after each pixel update [92]. On the contrary, our forward projection model is based on the Fourier Slice Theorem that determines the forward projection of an entire object. Hence, updating the error sinogram after each pixel update would mean performing FFT and inverse FFT of an entire object, which would be computationally infeasible. For the same reason, we update the error sinogram after all N pixels have been updated namely batch process update. The Fourier based forward model is formulated to make the framework compatible to impose Coulomb gauge constraint when we, later, extend it for the reconstruction of the vector potential.

Adhering algorithm 6.1, we performed the tomographic reconstruction of the 2D Shepp-Logan phantom. The q-GGMRF parameters parameters used in this implementation comprised of $p = 1.1, T = 0.001$ and $\sigma_x = 0.8$. We used a 3×3 non-causal weighting
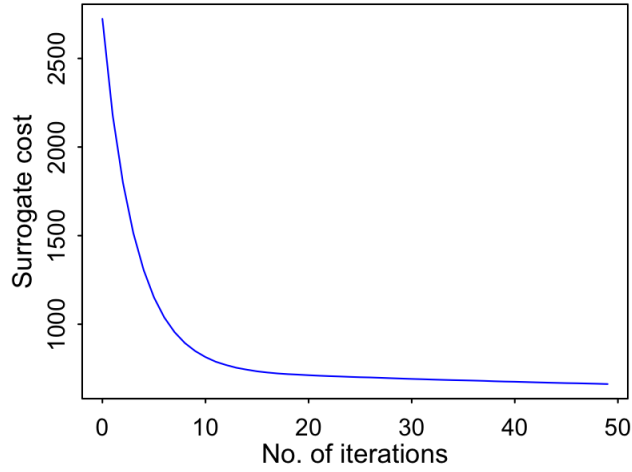
Figure 6.1: Illustration of minimization of surrogate cost function using ICD technique to deduce the MBIR estimate of Shepp-Logan phantom in fig. 6.2(e).

matrix, b_{jk}, to incorporate the influence of two nearest neighbors for any given pixel. The first nearest neighbors are weighted by a factor of 1/6 while the second nearest nearest neighbors are weighted by a factor of 1/12. The decreasing trend of the surrogate cost function over several iterations is shown in figure 6.1. Likewise, the corresponding MAP estimate obtained after the cost minimization is depicted in figure 6.2(e). We have compiled the MBIR result along with the results from other tomography methods such as Backprojection (BP), Filtered Backprojection (FBP), Simultaneous Iterative Reconstruction Technique (SIRT) - discussed in chapter 3 - for a direct comparison between different tomography methods. Also, we have changed the color scale from gray scale to red-blue scale; so that the accuracy of the MBIR approach to resolve the initial density can be realized even by a quick glance.

A thorough analysis of figure 6.2 reveals that the result obtained from the BP approach (figure 6.2(b)) agrees the least with the true phantom. The RMSE value of the BP result was calculated to be 0.4635. Such high RMSE value was expected as BP method is the simplest form of reconstruction technique which does not incorporate any filter or iterative technique in its model. Noise seen in the BP result is considerably subdued in the FBP result (figure 6.2(c)). Similarly, the RMSE value decreased to about 0.1586 for the FBP result. Reconstruction from the SIRT method (figure 6.2(d)) shows further
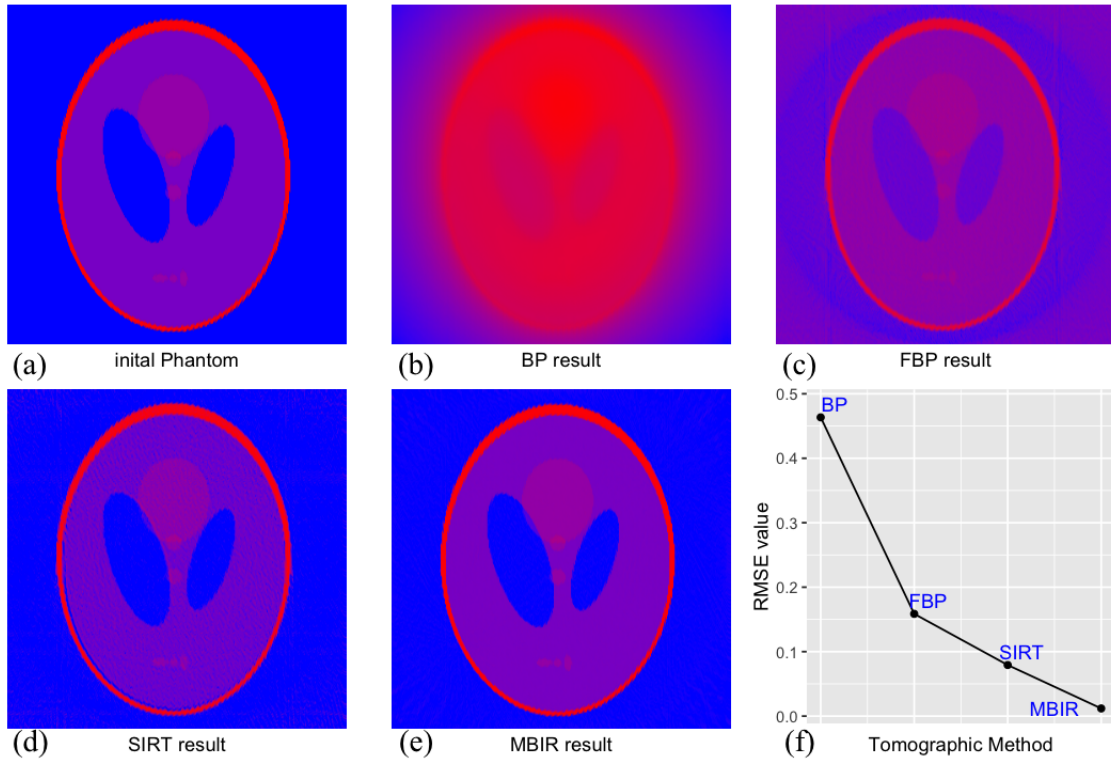
Figure 6.2: An illustration of reconstructed results of the (a) 2D Shepp-Logan phantom from different tomographic methods. The tomographic methods we have used comprises of (b) Back Projection [BP], (c) Filtered Back Projection [FBP], (d) Simultaneous Iterative Reconstruction Technique (SIRT), and (e) Model Based Iterative Technique (MBIR). These images (a-e) have values in the range 0 (corresponding to blue) to 1 (corresponding to red). The final plot, (f), consists of Root Mean Square Error (RMSE) analysis of the results obtained from aforementioned tomographic methods.

improvement as ring artifact, seen in the FBP result, is entirely diminished. The RMSE value corresponding to the SIRT result was determined to be 0.0793. As explained in section 3.1.4, the effectiveness of the SIRT approach over analytical method like the FBP approach stems from the fact that the SIRT approach iteratively works to minimize error sinogram. However, the ill poised nature of tomography problems restricts the SIRT strategy to exhibit semi-convergence [93, 94]. Accordingly, improvements seen in the first few SIRT iterates, start to deteriorate as the number of iterations increases due to noise propagation. Finally, the reconstruction obtained from the MBIR approach (figure 6.2(e)), visually, looks to be the most accurate reconstruction when compared to the results from other methods. This result is obtained after minimizing its corresponding cost function (figure 6.1), is globally minimum and is unique. Hence, the coarseness seen along the inner region of the locally converged SIRT result is no longer visible in the MBIR result. Also, the superiority of the MBIR approach over any of the other tomography methods can be discerned from the RMSE analysis whereupon the MBIR result was deemed to exhibited an error of only 0.0213.

We proceed to reconstruct the solenoid component of 2D fluid flow within a circle (figure 4.2a) making use of the MBIR approach. Thus obtained MAP estimate of the solenoid part is illustrated in figure 6.3(b) along with its theoretical, in figure 6.3(a), and its FBP, in figure 6.3(c), based solenoid counterparts. We illustrate the results in terms of contour plots. Accordingly, readers can qualitatively gauge how the irregularities in the contours of the solenoid part of the field from the FBP result have been regularized with the aid of the MBIR approach. Moreover, line plot comparison in figure 6.3(d) delineates the accuracy of the MBIR approach over the FBP method to ascertain correct values of the solenoid. In regards to the quantitative gain, the NRMSE of the FBP based reconstruction was determined to be 4%, which decreased to about 3% with the MBIR approach. There is not much of gain in terms of NRMSE analysis due to the fact that the FBP approach, here, does a good job in estimating the true value at the first place. This is primarily owing to the fact that the initial field has contribution from only the x component and is 2D in nature. Nonetheless, the ability of the MBIR approach to regularize the reconstructed solenoid part to deduce a close approximation of the theoretical values is a promising result. It falls along the lines of our hypothesis that the MBIR approach resolves the 3D

magnetic vector potential, $\mathbf{A}(\mathbf{r})$, more accurately than the one deduced from the VFET approach. Accordingly, we move on from proof-of-concept type implementation of the MBIR approach to, truly, reconstruct $\mathbf{A}(\mathbf{r})$ using the approach and test our claim in the next section.

6.3 On 3D interface (Magnetic Vector Potential)

In this section, we provide a thorough outline on how to incorporate the MBIR framework for the reconstruction of all three components of the magnetic vector potential, $\mathbf{A}(\mathbf{r})$. Thus formulated framework is used to reconstruct $\mathbf{A}(\mathbf{r})$ from x tilt and y tilt series of synthetic Nanoparticles (NPs). Next, the MBIR framework is used to deduce $\mathbf{A}(\mathbf{r})$ of experimental datasets such as permalloy (Py) square island and Py lattice. Finally, a detailed comparative study is performed on the reconstructions obtained from the MBIR approach and the VFET approach. Based on the study, we give the final verdict on our hypothesis.

6.3.1 MBIR framework for vector reconstruction

The MBIR framework for vector field reconstruction revolves around solving an optimization problem similar in form to the one expressed in eq. 5.2. Specifically, we seek to formulate a framework that will iteratively work to minimize the sum of the squared differences between the data and its estimated forward projection, in combination with a regularizing prior function, $\mathcal{P}(x)$. However, in contrast to scalar reconstruction, we need to resolve three different components in a vector reconstruction. The projection measurements of a vector potential encompass more than one component as shown by eqs. 4.21 and 4.22. Hence, it is not possible to take just one of the tilt series and minimize with respect to one of the vector components to reconstruct the potential field. In fact, the VFET approach in 4.2.2 section has shown us that the three components of the vector potential can only be reconstructed if we have measurements from two different tilt series and if we impose the Coulomb gauge constraint [62]. Accordingly, our generic MBIR framework from section 6.1 needs to be reformulated to account for input measurements
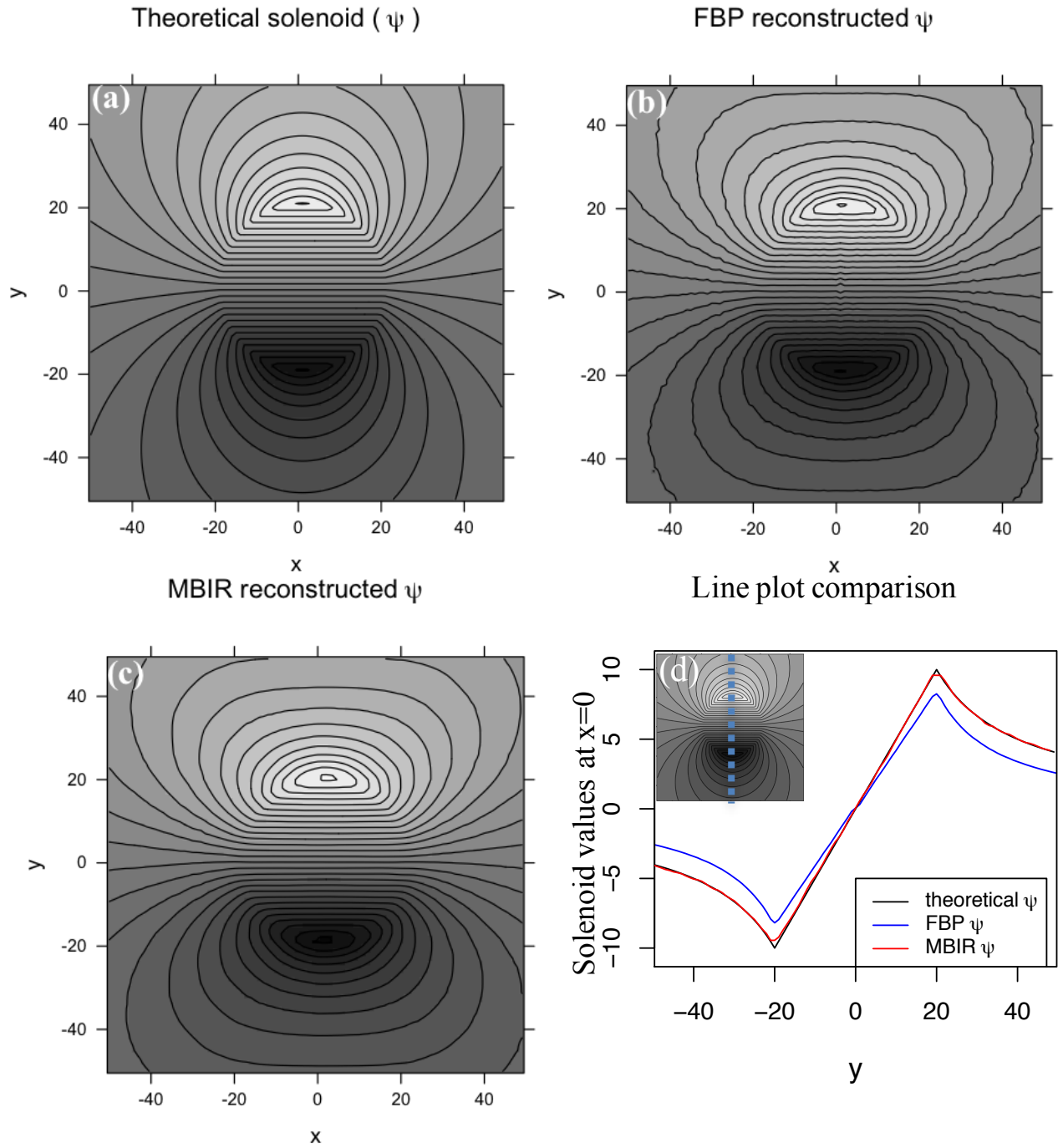
Figure 6.3: Reconstruction of (a) solenoid part (ψ) of a 2D vector field using (b) the filtered backprojection (FBP) approach and (c) the MBIR approach. Plot (d) illustrates line plot comparison of solenoid values at $x = 0$ from the two approaches.
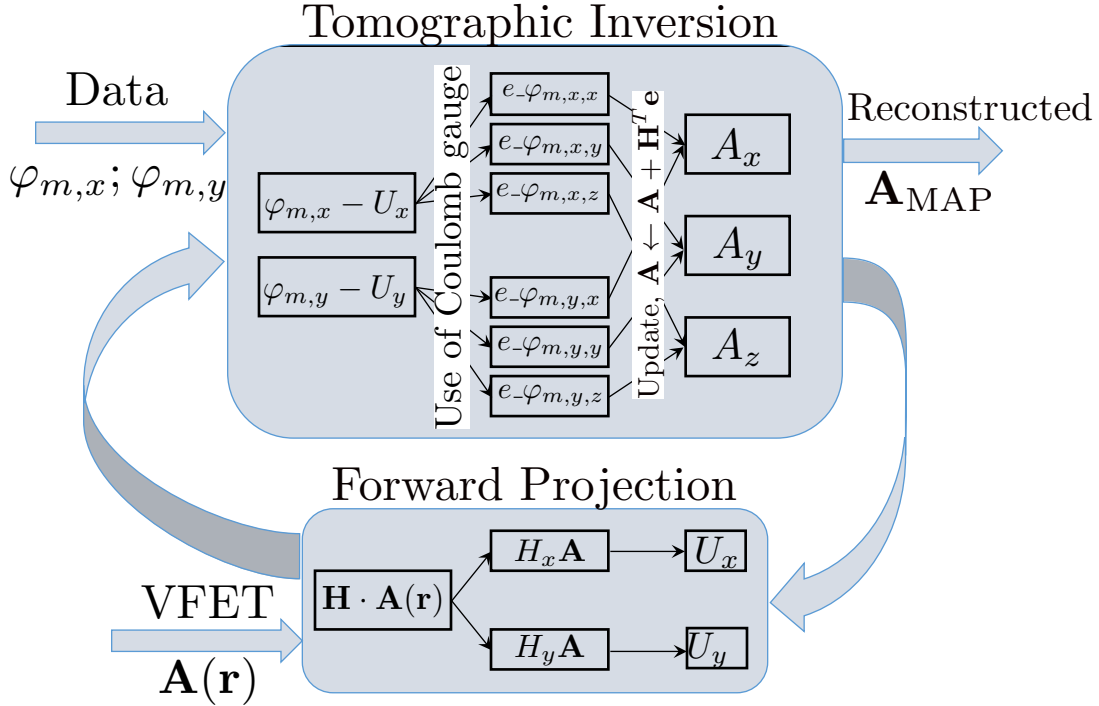
Figure 6.4: Flowchart illustrating the use of the MBIR technique to reconstruct the magnetic vector potential, $\mathbf{A}(\mathbf{r})$. First, the values for $\mathbf{A}(\mathbf{r})$ are initialized using the VFET approach. Next, $\mathbf{A}(\mathbf{r})$ is forward projected in x and y tilt series (U_x and U_y). Thus determined tilt series is subtracted from the sinogram measurements ($\varphi_{m,x}$ and $\varphi_{m,y}$) obtained from experiments. Subsequently, the contribution of error sinogram to each component of vector potential is evaluated by employing the coulomb gauge condition. The error sinogram is inverted and is added to initial $\mathbf{A}(\mathbf{r})$ value to update vector potential. Finally, the updated $\mathbf{A}(\mathbf{r})$ is passed on to the forward projection interface and the loop continues until the cost function in eq. 6.16 is minimized to yield $\mathbf{A}_{\mathrm{MAP}}$.
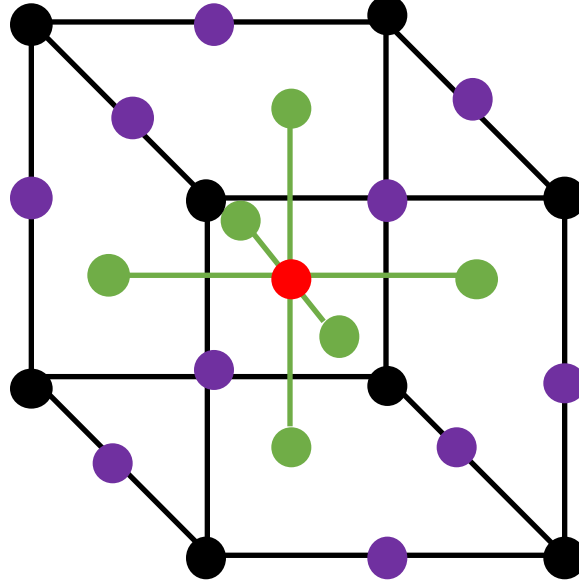
Figure 6.5: A 3D illustration of first (green ball), second (purple ball) and third (black ball) nearest neighbors of a voxel (red ball), respectively.

from the two tilt series and imposition of the gauge constraint.

We begin MBIR based vector reconstruction by defining input data, $\varphi_m = [\varphi_{m,x}, \varphi_{m,y}]$, and subsequent estimates of magnetic vector potential, $\mathbf{x} = [x_x, x_y, x_z]$. Let $\mathbf{H} = [H_x, H_y]$ where H_x and H_y are operators for forward projection of a vector in counter clockwise direction for x tilt and y tilt series, in accordance to eqs. 4.21 and 4.22, respectively. Then the forward projection of $\mathbf{x}$ yields, $\mathbf{Hx} = [H_x, H_y]\,\mathbf{x} = [U_x, U_y]$. We define a deconvolution operator, $\mathbf{D} = [D_x, D_y, D_z]$, that will serve to evaluate contributions of magnetic phase shift (as per eq. 4.30 and 4.31) and $\mathbf{A}(\mathbf{r})$ to each component of vector potential separately. Hence, any of the components D_* of deconvolution operator applied on phase shift yields $D_*\varphi_m = [D_*\varphi_{m,x}, D_*\varphi_{m,y}] = [\varphi_{m,x,*}, \varphi_{m,x,*}]$; and its application on $\mathbf{A}(\mathbf{r})$ yields $D_*\mathbf{A}(\mathbf{r}) = A_*$.

Next, we define the prior model analogous to the one defined in section 6.1. We use a q-GGMRF as the potential function that minimizes the cost function for a given voxel based on the difference with its neighboring voxels. However, contrary to the 2D MBIR approach, we incorporate the influence of three nearest neighbors (fig. 6.5) for any given voxel while evaluating the potential function $\rho(\cdot)$. Accordingly, the non-causal weighting

matrix, b_{jk}, now contains $3 \times 3 \times 3$ values with first, second and third weighing factors assigned as, 9/132, 9/264, and 9/396, respectively. Finally, we again make use of the surrogate majorization technique such that the q-GGMRF potential function assumes a quadratic form for $p \neq 2$.

Having defined all the pertinent variables, we can now express MBIR-based vector reconstruction as the solution to the following optimization problem:

$$\hat{\mathbf{x}} = \underset{\mathbf{x}}{\operatorname{argmin}} \left\{ \frac{1}{2} \|\mathbf{D}\varphi_m - \mathbf{D}(\mathbf{Hx})\|^2 + \sum_{k\epsilon\partial j} \tilde{b}_{jk}\mathbf{D}(\mathbf{x}(j) - \mathbf{x}(k))^2 \right\}, \tag{6.16}$$

where b_{jk} is determined using eq. 6.12. In practice, we do not directly solve eq. 6.16. Instead we make use of deconvolution operator, $\mathbf{D}$, and de-convolve eq. 6.16 into three MAP estimation problems as:

$$\hat{x}_x = \underset{\mathbf{x}}{\operatorname{argmin}} \left\{ \frac{1}{2} \|D_x\varphi_m - D_x(\mathbf{Hx})\|^2 + \sum_{k\epsilon\partial j} \tilde{b}_{jk}D_x(\mathbf{x}(j) - \mathbf{x}(k))^2 \right\}, \tag{6.17}$$

$$\hat{x}_y = \underset{\mathbf{x}}{\operatorname{argmin}} \left\{ \frac{1}{2} \|D_y\varphi_m - D_y(\mathbf{Hx})\|^2 + \sum_{k\epsilon\partial j} \tilde{b}_{jk}D_y(\mathbf{x}(j) - \mathbf{x}(k))^2 \right\}, \tag{6.18}$$

$$\hat{x}_z = \underset{\mathbf{x}}{\operatorname{argmin}} \left\{ \frac{1}{2} \|D_z\varphi_m - D_z(\mathbf{Hx})\|^2 + \sum_{k\epsilon\partial j} \tilde{b}_{jk}D_z(\mathbf{x}(j) - \mathbf{x}(k))^2 \right\}. \tag{6.19}$$

Next, we identify cost function associated with each of the potential estimates in eq. 6.17, 6.18, and 6.19 as:

$$c(\mathbf{x}, x_x; x_x') = \frac{1}{2} \|D_x\varphi_m - D_x(\mathbf{Hx})\|^2 + \sum_{k\epsilon\partial j} \tilde{b}_{jk}D_x(\mathbf{x}(j) - \mathbf{x}(k))^2, \tag{6.20}$$

$$c(\mathbf{x}, x_y; x_y') = \frac{1}{2} \|D_y\varphi_m - D_y(\mathbf{Hx})\|^2 + \sum_{k\epsilon\partial j} \tilde{b}_{jk}D_y(\mathbf{x}(j) - \mathbf{x}(k))^2, \tag{6.21}$$

$$c(\mathbf{x}, x_z; x_z') = \frac{1}{2} \|D_z\varphi_m - D_z(\mathbf{Hx})\|^2 + \sum_{k\epsilon\partial j} \tilde{b}_{jk}D_z(\mathbf{x}(j) - \mathbf{x}(k))^2, \tag{6.22}$$

Algorithm 6.2 MBIR method to reconstruct magnetic vector potential

---

1. Evaluate $\mathbf{A}(\mathbf{r}) \leftarrow$ VFET

2. $\mathbf{F}(\mathbf{r}) \leftarrow$ VFET

3. **while** not converged **do**

   (a) **for** i in $1 : N$ {

   Determine corresponding $\tilde{b}_{ij}$ for $\{i, j\} \, \epsilon \, \mathcal{C}$ of $A_x(i)$ using eq. 6.12

   $$A_x(i) \leftarrow \frac{F_x(i) + 2 \sum\limits_{\{i,j\}\epsilon\mathcal{C}} \tilde{b}_{ij} A_x(j)}{1 + 2 \sum\limits_{\{i,j\}\epsilon\mathcal{C}} \tilde{b}_{ij}} \quad \}$$

   end for

   (b) Update A_y and A_z in a manner similar to (a)

   (c) Forward project $\mathbf{A}(\mathbf{r})$ using eqs. and to determine U_x and U_y eqs. 4.21 and 4.22 respectively

   (d) Determine error sinogram for the two series as:

   $e\_\varphi_{m,x} = \varphi_{m,x} - U_x$

   $e\_\varphi_{m,y} = \varphi_{m,y} - U_y$

   (e) Use the results of imposing gauge constraint from eq. on $e\_\varphi_{m,x}$ and $e\_\varphi_{m,y}$ to determine $e\_\varphi_{m,x,x}, e\_\varphi_{m,x,y}, e\_\varphi_{m,x,z}, e\_\varphi_{m,y,x}, e\_\varphi_{m,y,y}$ and $e\_\varphi_{m,y,z}$

   (f) Update the components of vector potential as

   $A_x \leftarrow A_x + H^T(e\_\varphi_{m,x,x} + e\_\varphi_{m,y,x})$

   $A_y \leftarrow A_y + H^T(e\_\varphi_{m,x,y} + e\_\varphi_{m,y,y})$

   $A_z \leftarrow A_z + H^T(e\_\varphi_{m,x,z} + e\_\varphi_{m,y,z})$

   end do

We, again, employ the ICD technique to minimize the surrogate cost function in eqs. 6.20 - 6.22. Accordingly, differentiating these equations with respect to $\mathbf{x}(j)$ and setting the resultant equal to zero, we get:

$$x_x(j) \leftarrow \frac{\left(H_x^T \varphi_{m,x,x} + H_y^T \varphi_{m,y,x}\right) + 2 \sum_{\partial k \epsilon j} \tilde{b}_{jk} x_x(k)}{1 + 2 \sum_{\partial k \epsilon j} \tilde{b}_{jk}}, \tag{6.23}$$

$$x_y(j) \leftarrow \frac{\left(H_x^T \varphi_{m,x,y} + H_y^T \varphi_{m,y,y}\right) + 2 \sum_{\partial k \epsilon j} \tilde{b}_{ij} x_y(k)}{1 + 2 \sum_{\partial k \epsilon j} \tilde{b}_{jk}}, \tag{6.24}$$

$$x_z(j) \leftarrow \frac{\left(H_x^T \varphi_{m,x,z} + H_y^T \varphi_{m,y,z}\right) + 2 \sum_{\partial k \epsilon j} \tilde{b}_{jk} x_z(k)}{1 + 2 \sum_{\partial k \epsilon j} \tilde{b}_{jk}}. \tag{6.25}$$

Note that the MAP estimate of each component of vector potential, $\hat{x}_*$, is determined by performing element wise minimization of its associated cost function from eq. 6.17 - 6.19 with respect to overall magnetic vector potential, $\mathbf{x}(j)$, instead of individual component, $x_*(j)$. This is primarily owing to the fact that each component is reconstructed with the aid of two tilt series, $\varphi_{m,x}$ and $\varphi_{m,y}$, which in turn has contributions from all three components of vector potential, $\mathbf{A}(\mathbf{r})$. Hence, each iteration of ICD required to ascertain $\mathbf{A}(\mathbf{r})$ comprises of simultaneously evaluating eq. 6.23 - 6.25 and then making use of forward model and deconvolution operator to update estimates of vector component as:

$$\mathbf{Dx} \leftarrow \mathbf{Dx} + \mathbf{H}^T(\mathbf{D}\varphi_m - \mathbf{D}(\mathbf{Hx})). \tag{6.26}$$

Summaries of the MBIR based $\mathbf{A}(\mathbf{r})$ reconstruction are illustrated in the form of schematic in figure 6.4 and in the form of pseudo code in Algorithm 6.2. In the next two subsections we make use of the MBIR algorithm to reconstruct vector potential of simulated data set as well an experimental data set.

6.3.2 MBIR on synthetic datasets

In this section, we apply the MBIR algorithm to reconstruct the $\mathbf{A}(\mathbf{r})$ of synthetic magnetic nanoparticles (spherical, prismatic and cylindrical MNPs) discussed in section

Figure 6.6: Reconstructed magnetic vector potential of the spherical NP deduced from the VFET approach [center column] and the MBIR approach [right most column] with the aid of projection in range $[-70°, 70°]$. The leftmost column depicts the ground truth. Plots in the top row correspond to the plane $(x, 28, z)$ while the ones in the bottom row correspond to the plane $(x, 35, z)$.
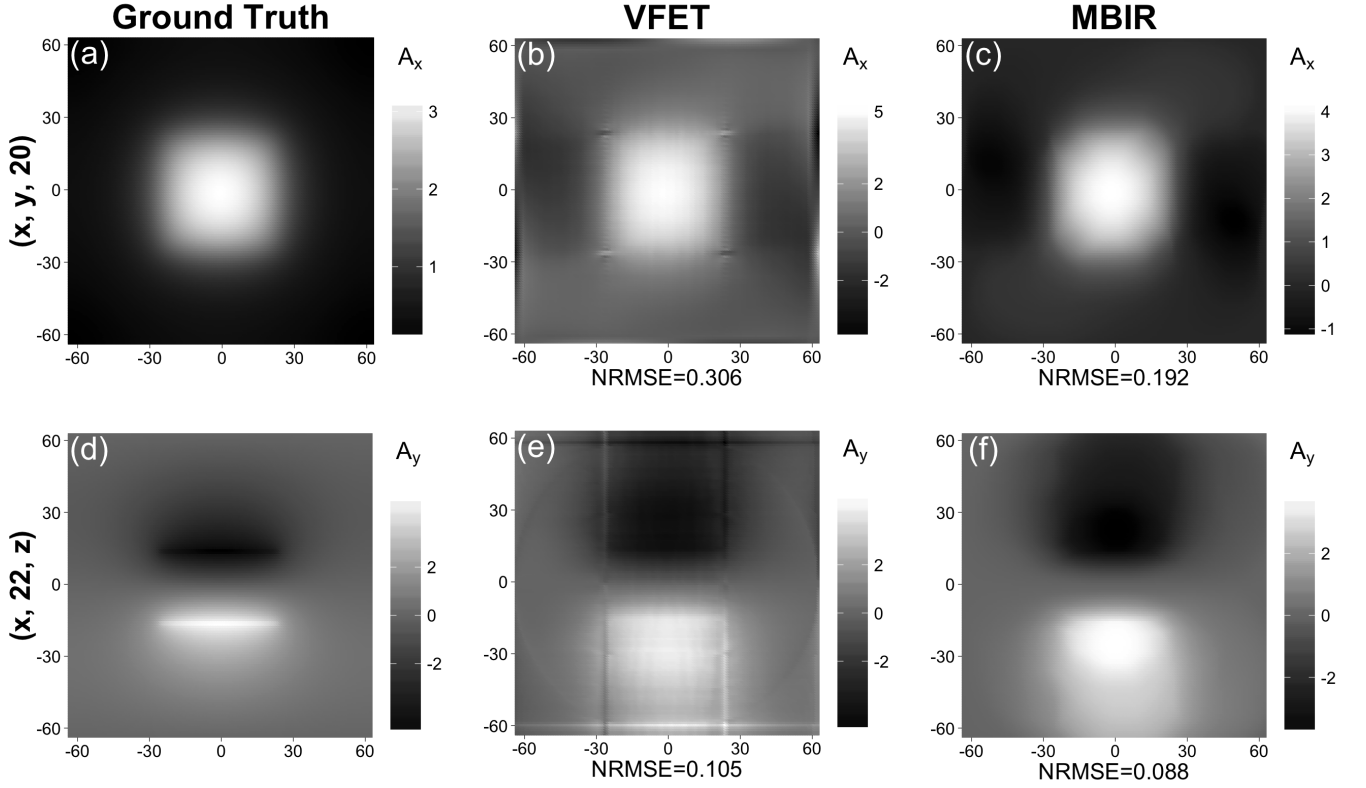
Figure 6.7: Reconstructed magnetic vector potential of the prismatic NP deduced from the VFET approach [center column] and the MBIR approach [right most column] with the aid of projection in range $[-70°, 70°]$. The leftmost column depicts the ground truth. Plots in the top row correspond to the plane $(x, y, 20)$ while the ones in the bottom row correspond to the plane $(x, 22, z)$.
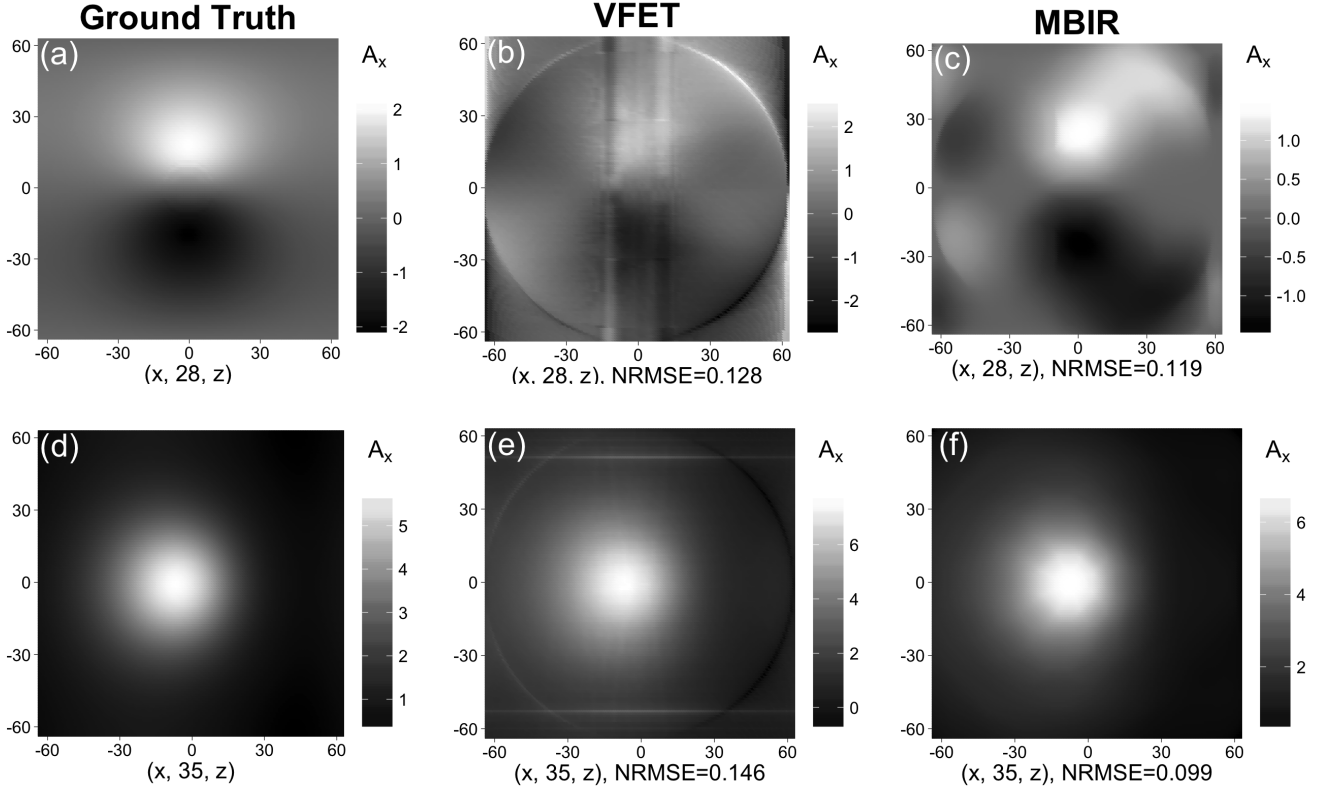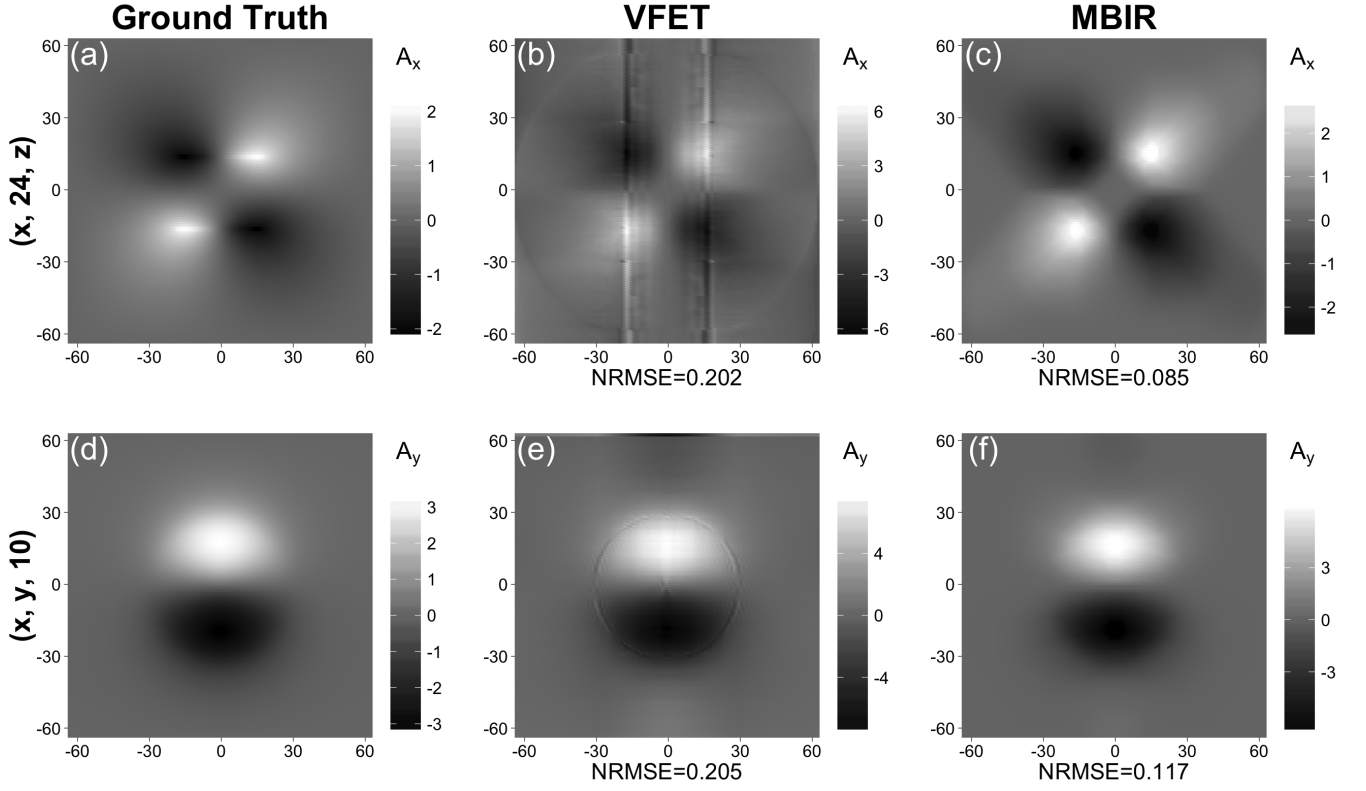
Figure 6.8: Reconstructed magnetic vector potential of the cylindrical NP deduced from the VFET approach [center column] and the MBIR approach [right most column] with the aid of projection in range $[-70°, 70°]$. The leftmost column depicts the ground truth. Plots in the top row correspond to the plane $(x, 24, z)$ while the ones in the bottom row correspond to plane $(x, y, 10)$.

4.2.2. The reconstruction was performed making use of the missing wedge projection set since this set replicates the limited angular scenario typical of TEM based experimental measurements. The q-GGMRF parameters used for the reconstruction comprised of $p = 1.001, T = 0.01$ and $\sigma_x = 0.8$. Selected results retrieved from the MBIR approach are depicted in Figures 6.6, 6.7 and 6.8. These figures also include corresponding plots from the ground truth and the VFET approach for the purpose of qualitative comparison of reconstruction accuracy between the two approaches. Additionally, we present quantitative comparisons between the two methods in terms of NRMSE plots in Figures 6.9, 6.10 and 6.11 for the spherical, prismatic and cylindrical NPs respectively.

A review of the plots in figures 6.6, 6.7 and 6.8 reveals that the low spatial resolutions, protrusions, ring artifacts and edge artifacts evident in the VFET reconstructions are significantly suppressed in the MBIR-based reconstructions. In case of the spherical MNP, we note that the quantitative gain in terms of decrease in the NRMSE values for the MBIR-based reconstruction as compared to the ones from the VFET approach is relatively low for A_x and A_y components (figures 6.9(a-b, d-e, g-h)). However, the NRMSE plots for A_z component show reduction in the error by about 10% all across the x, y and z planes having employed the MBIR approach from the VFET approach (figures 6.9(c, f, i)). In case of the prismatic MNP, the NRMSE plot in figure 6.10 delineates $2-20\%$ reduction in error for the MBIR approach from the VFET approach. Finally, for the cylindrical MNP the NRMSE values in figure 6.11 demonstrate a decrease in error by about $10-40\%$, all across the x, y and z planes, for the MBIR technique. We end this section with 3D representation of magnetic vector potential of the three MNPs in figure 6.12. This plot is produced with the aid of ParaView plotting tool [95].

6.3.3 MBIR on experimental datasets

This section elucidates on the use of real data sets to demonstrate the gain in reconstruction quality from making use of the MBIR approach. More specifically, a $Ni_{80}Fe_{20}$ (permalloy/py) square island and a 2D lattice of elongated Py islands ("stadia") are used for the comparative study of the MBIR and VFET techniques. First, Py island sample was fabricated by depositing a 27 nm Py thin film on a square TEM grid with a SiO sup-

Figure 6.9: Planar NRMSE plots of magnetic vector potential of spherical NP retrieved using the VFET approach (line with circle) and the MBIR approach (line with asterisk).

Figure 6.10: Planar NRMSE plots of magnetic vector potential of prismatic NP retrieved using the VFET approach (line with circle) and the MBIR approach (line with asterisk).
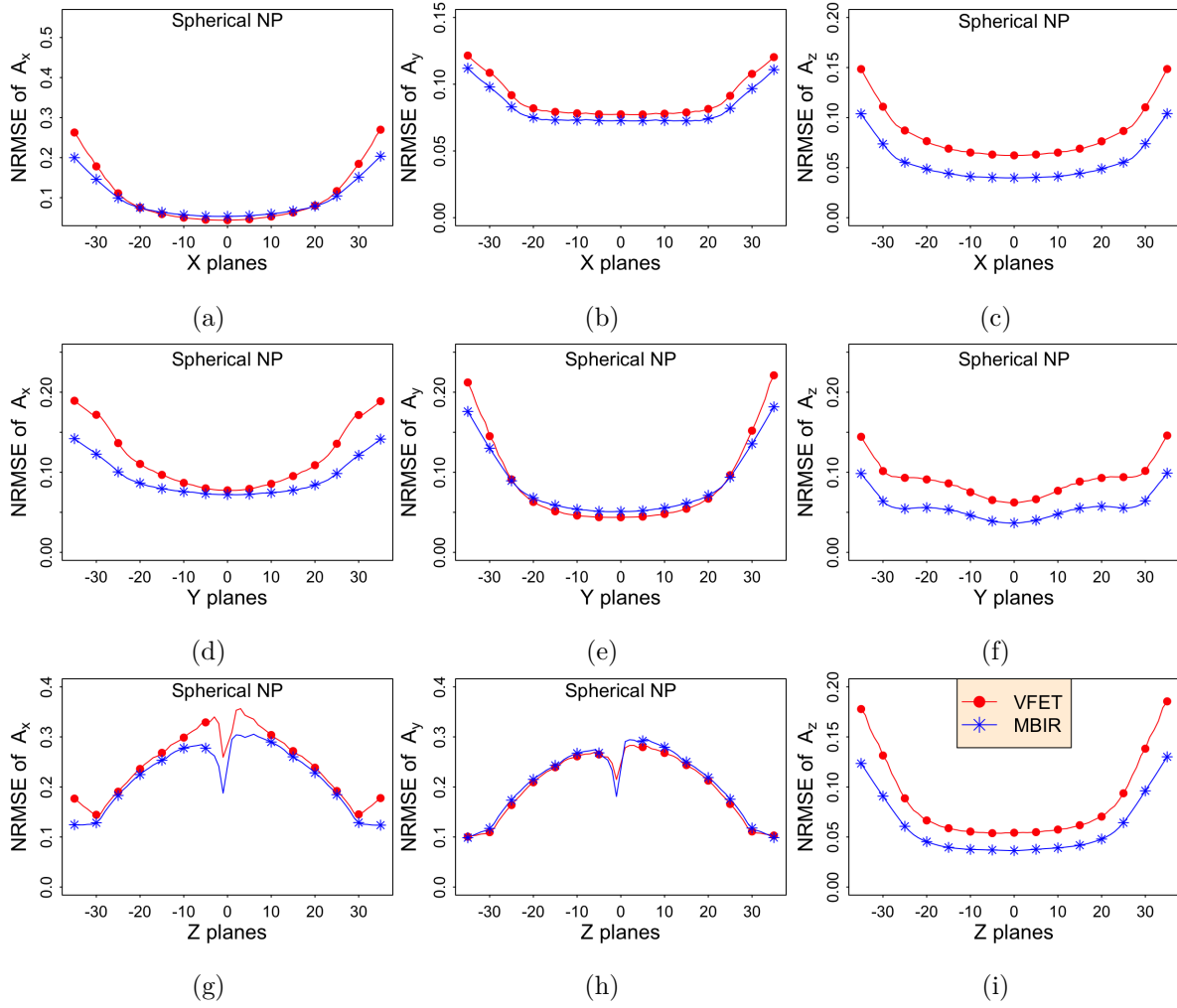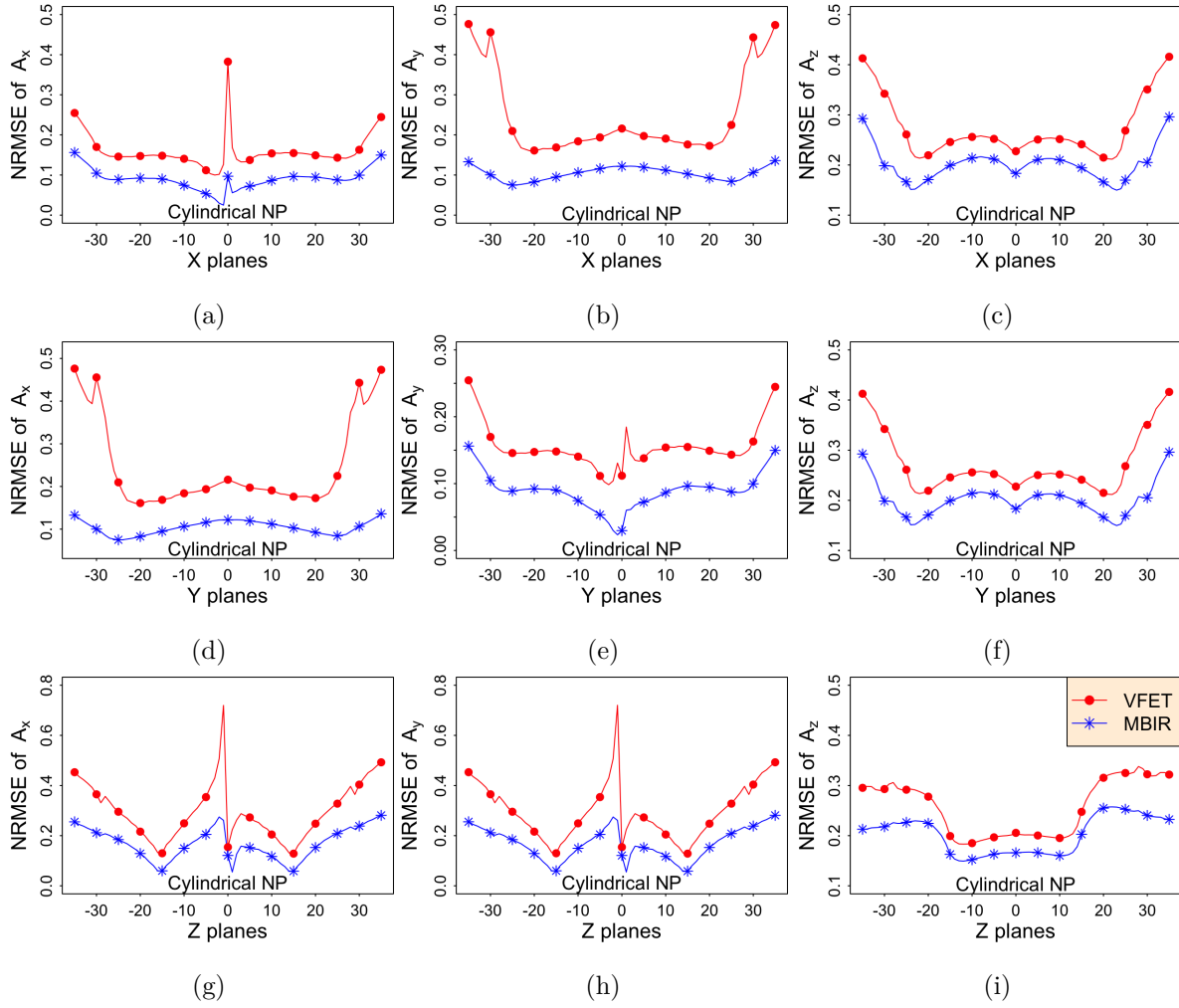
Figure 6.11: Planar NRMSE plots of magnetic vector potential of cylindrical NP retrieved using the VFET approach (line with circle) and the MBIR approach (line with asterisk).
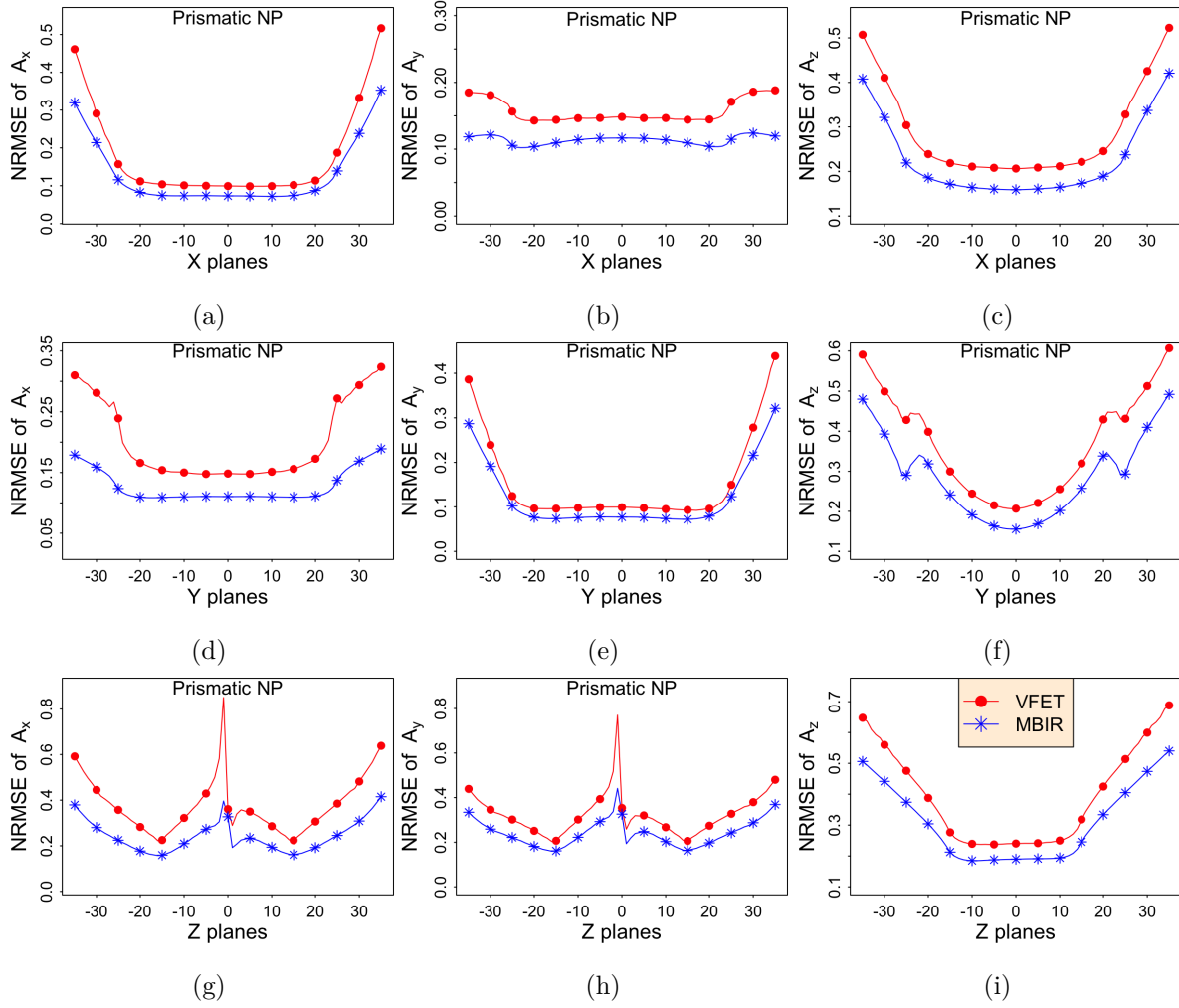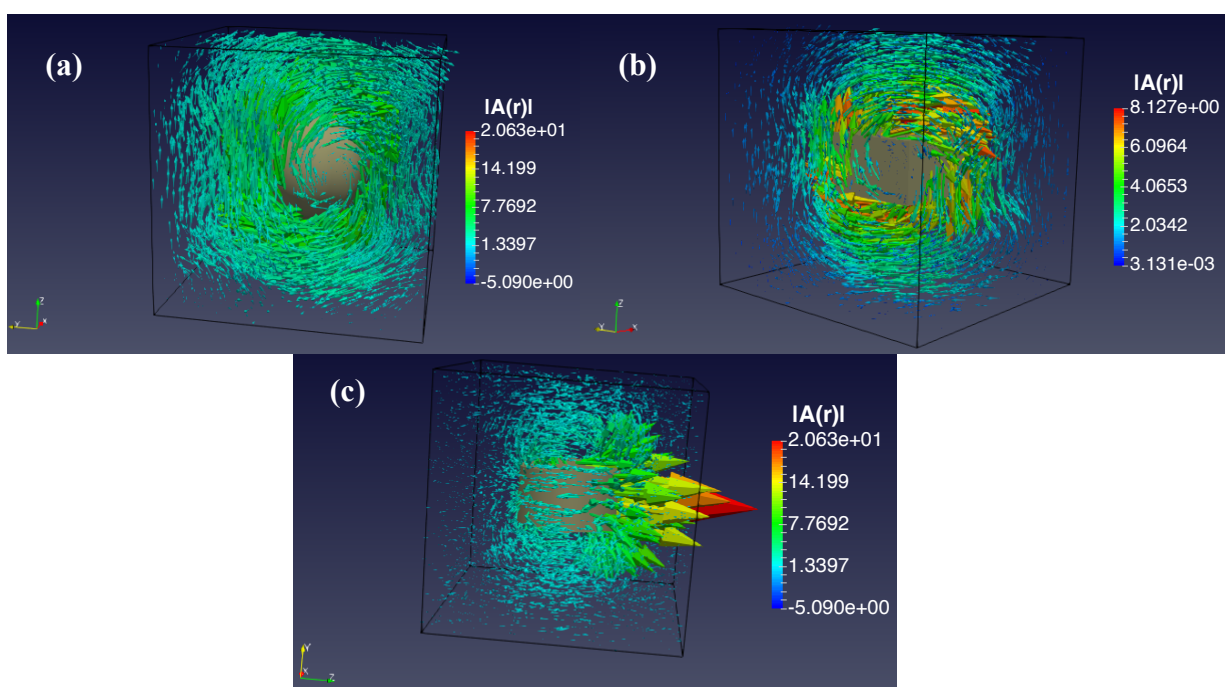
Figure 6.12: 3D illustration of vector potential reconstructed from the MBIR approach of (a) Spherical MNP (b) Prismatic MNP (c) Cylindrical MNP.

port membrane. Magnetron sputtering was used to deposit the thin film. Then a square island was patterned using focused ion beam (FIB) milling. The grid was mounted in a tomography holder and loaded into JOEL 2100F TEM equipped with a special low field pole piece for magnetic characterization and a spherical aberration corrector. The TEM experiment was operated at 200 kV and two tilt series about orthogonal axes, x & y, were recorded for angles ranging from $-70°$ to $+70°$ at a $2°$ increment. A three-image through-focus series was acquired for each tilt angle. This was followed by a sample flip of $180°$ and two more tilt series were acquired under identical conditions [96]. The magnetic phase shift was then determined by employing the TIE formalism in combination with time symmetry property (as described in chapter 2). Figures 6.13(a-c) depicts the under-, in-, and over-focus Fresnel images of the Py island acquired at the $0°$ tilt for the upright position. Likewise, figure 6.13(d) illustrates the corresponding holographic plot [at $\cos(\varphi_m)$] of the magnetic phase shift of the Py square island deduced from the TIE formalism for the $0°$ tilt. As noted in the figure, each phase map of Py sq. island has a resolution of 256×256 px with 1 px equal to 3.2 nm.

The second sample, Py lattice, was fabricated on a JEOL 9300 electron beam lithography system. A single layer of ZEP resist of 100 nm thickness was coated on a Si/SiN substrate, followed by patterning of a square lattice with element shape parameters of $2Lx = 290$ nm, $2Ly = 130$ nm, and a lattice spacing of $a = 390$ nm. A Py film of 20 nm thickness was deposited on a seed layer of Cr (3 nm) using dc magnetron sputtering at 3 mTorr pressure and 50 W power. The pattern was transferred by a lift-off process. This was followed by optical lithography and wet-etching of Si to create electron transparent windows on 3 mm square grids, which could be loaded directly into the TEM for observation. The microscopy was, again, performed using the JEOL 2100F TEM and through focus series was recorded for upright and flipped positions for x as well as y tilt series [97]. Subsequently, magnetic phase shift was evaluated. Here the projection measurements acquired in the two tilt series comprised of angles ranging from $-50°$ to $+50°$ at a step size of $1°$. Figures 6.14(a-c) depicts the under-, in-, and over-focus Fresnel images of the Py lattice acquired at the $0°$ tilt for the upright position. Correspondingly, figure 6.14(d) depicts a holographic plot [at $\cos(100\varphi_m)$] of the magnetic phase shift of the sample at $0°$ tilt from the TIE formalism. Each phase map has a resolution of 256×256 pixels with 1

px equal to 6 nm.

We implement our tomographic reconstruction on a 3D voxel grid with 256^3 nodes for both the samples. First, we employ the VFET approach (as discussed in section 4.2.2) to determine an estimate of $\mathbf{A}(\mathbf{r})$ of the Py island sample. The VFET result is then used to initialize the MBIR algorithm. The q-GGMFR parameters used during the discourse of MAP estimation of $\mathbf{A}(\mathbf{r})$ of the Py island comprised of $q = 2.0, p = 1.001, T = 0.01$, and $\sigma_x = 0.8$. The cost function in eq. 6.16 was then monotonically decreased over 35 iterations to determine a MAP estimate of $\mathbf{A}(\mathbf{r})$. The forward model calculation for each iteration was distributed over 24 parallel threads using OpenMP and required about 14 minutes to complete the iteration. Some of the $\mathbf{A}(\mathbf{r})$ results obtained from the VFET and MBIR approaches of the Py island are depicted in figures (6.15 - 6.17).

A thorough review of vector potential plots of the Py island sample from the two approaches reveals that the MBIR approach yields higher quality reconstruction that its VFET counterpart. First, streak and line artifacts that plague the VFET results (figures 6.15(a-c), 6.16(a-c) & 6.17(a-c)) are substantially minimized in the MBIR results (figures 6.15(d-f), 6.16(d-f) & 6.17(d-f)). Next, by comparing figures 6.15(g-i) with 6.15(j-l) and 6.16(g-i) with 6.16(j-l), we conclude that the MBIR technique more appropriately traces the edges in the reconstruction than the VFET method. Furthermore, the VFET results show faint to no distinctions between bright and dark regions. On the other hand, the bright and dark contrasts are clearly distinguishable in the MBIR results. Finally, white noise and blurriness, that degrade certain regions of the VFET results (figure 6.17 (g-i)), are considerably subdued in the MBIR result (figure 6.17(j-l)).

Similarly, we proceed to reconstruct $\mathbf{A}(\mathbf{r})$ of the Py lattice sample. We employ the same q-GGMRF parameters as in the case of the Py square island to determine the MAP estimate of the vector potential of the Py lattice. Again the cost function in eq. 6.16 is monotonically decreased over 35 iterations. The computational time for each iteration was about 18 minutes. Some of the VFET and the MBIR results obtained for the Py lattice sample is depicted in figures 6.18 through 6.20.

A methodical comparison of plots deduced from the two methods for the Py lattice sample reveals that the MBIR results show a significant gain in spatial resolution. The coarseness and noise artifacts seen in the VFET results (figures 6.18(g-i) & 6.19(g-i)) are
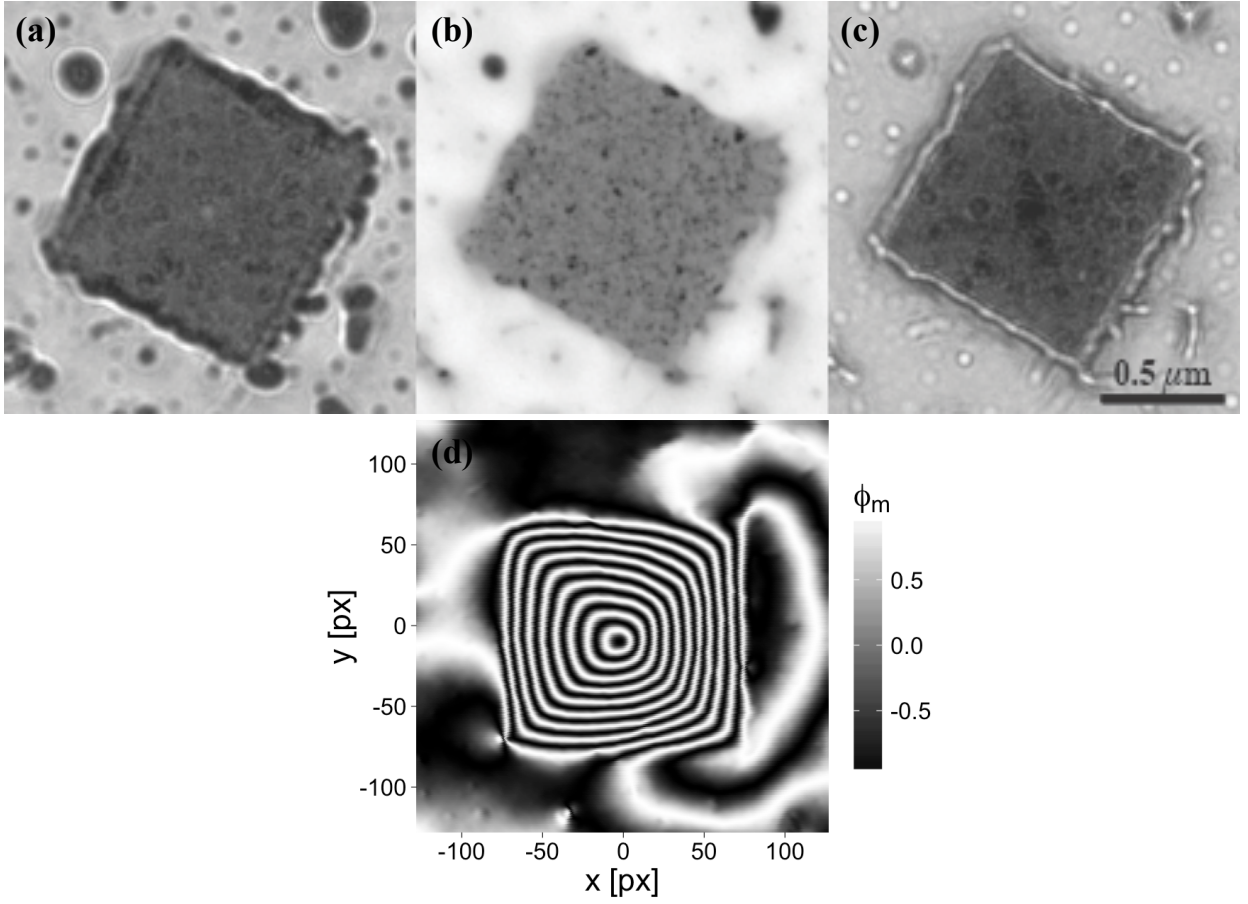
Figure 6.13: (a) – (c) show under-, in-, and over-focus Fresnel images of the Permalloy (Py) square island at 0° tilt. (d) Illustration of holographic contour map, ϕ_m, of the magnetic phase shift, φ_m, of the square Py sample at 0° tilt, where $\phi_m = \cos(\varphi_m)$ rad and 1 px = 3.2 nm.
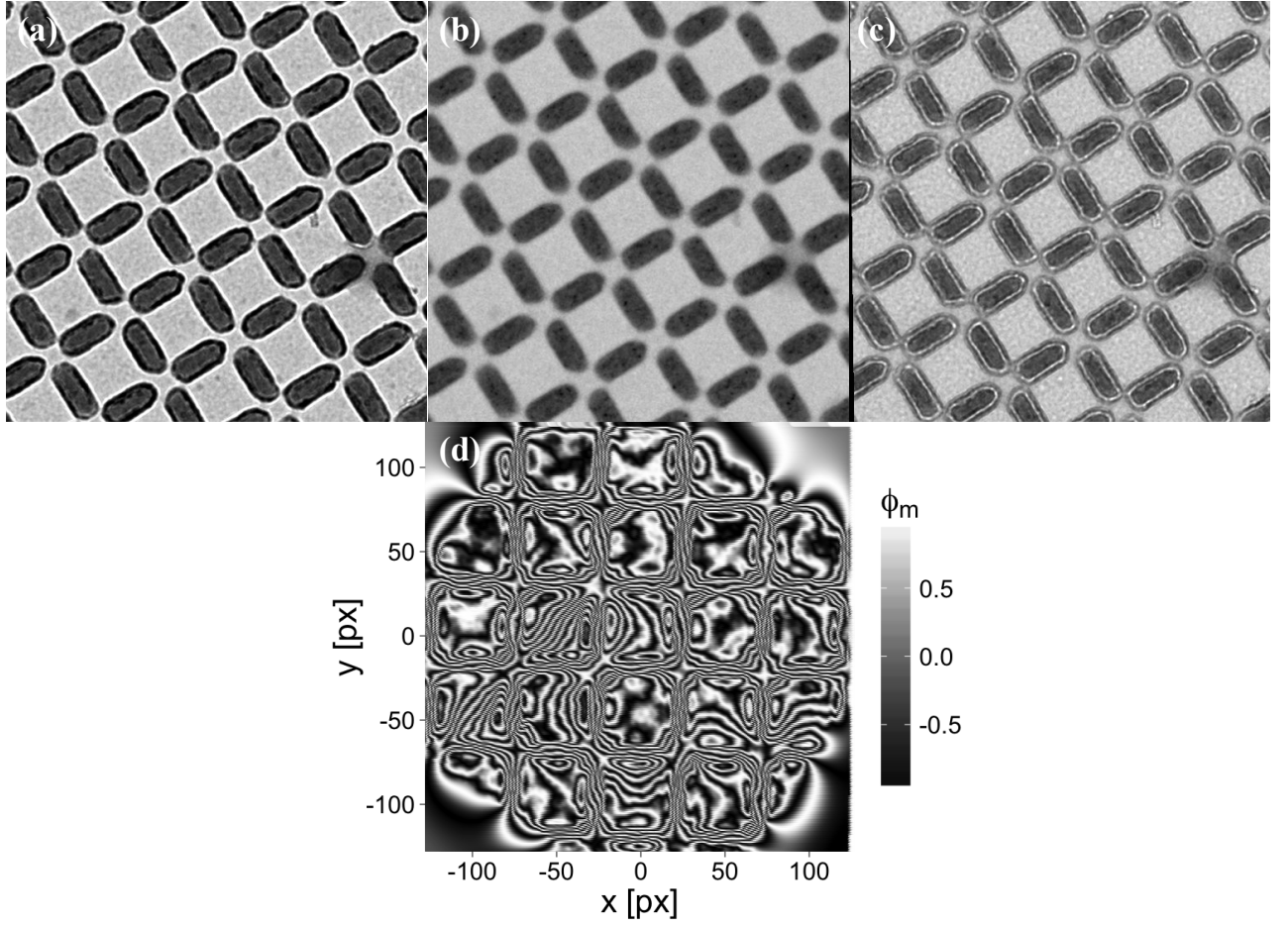
Figure 6.14: (a) – (c) show under-, in-, and over-focus Fresnel images of the Permalloy (Py) lattice sample at 0° tilt. (d) Illustration of holographic contour map, ϕ_m, of the magnetic phase shift, φ_m, of the Py lattice sample at 0° tilt, where $\phi_m = \cos(100\varphi_m)$ rad and 1 px = 6 nm.
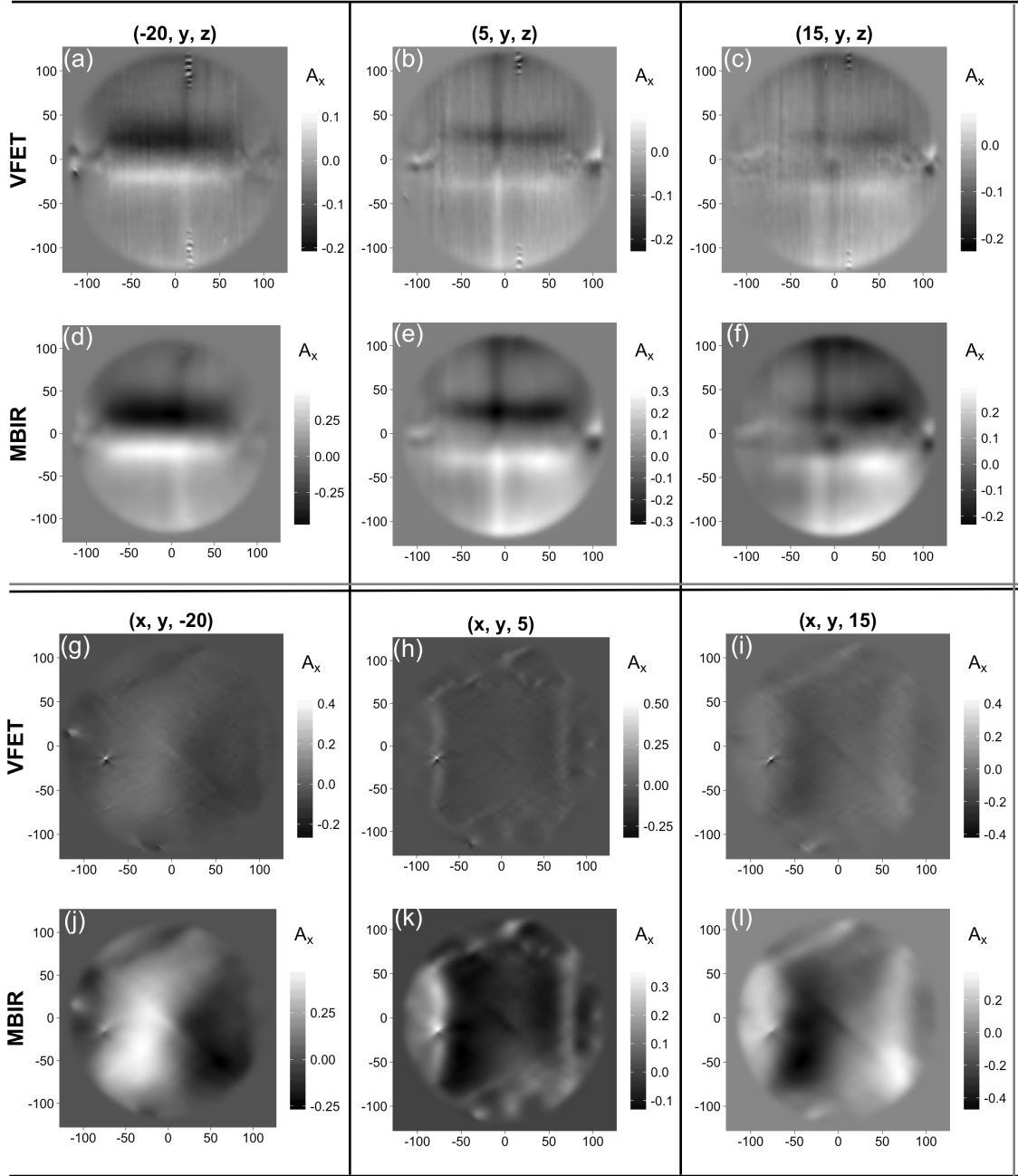
Figure 6.15: Reconstructed A_x of Py island from the VFET approach [first and third column] and the MBIR approach [second and fourth column]. The unit for $\mathbf{A}(\mathbf{r})$ is T-px where 1 px equals 3.2 nm.
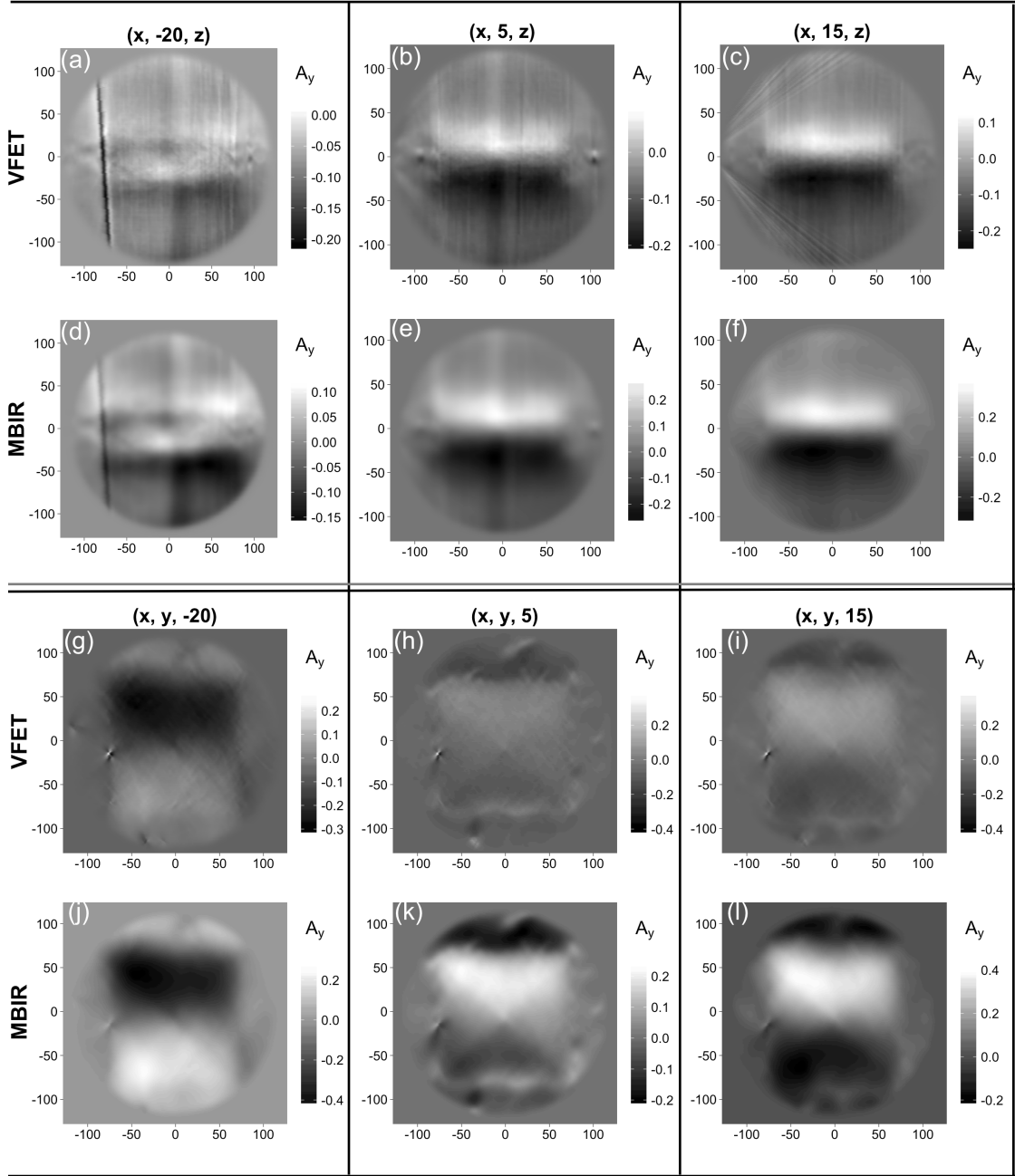
Figure 6.16: Reconstructed A_y of Py island from the VFET approach [first and third column] and the MBIR approach [second and fourth column]. The unit for $\mathbf{A}(\mathbf{r})$ is T-px where 1 px equals 3.2 nm.
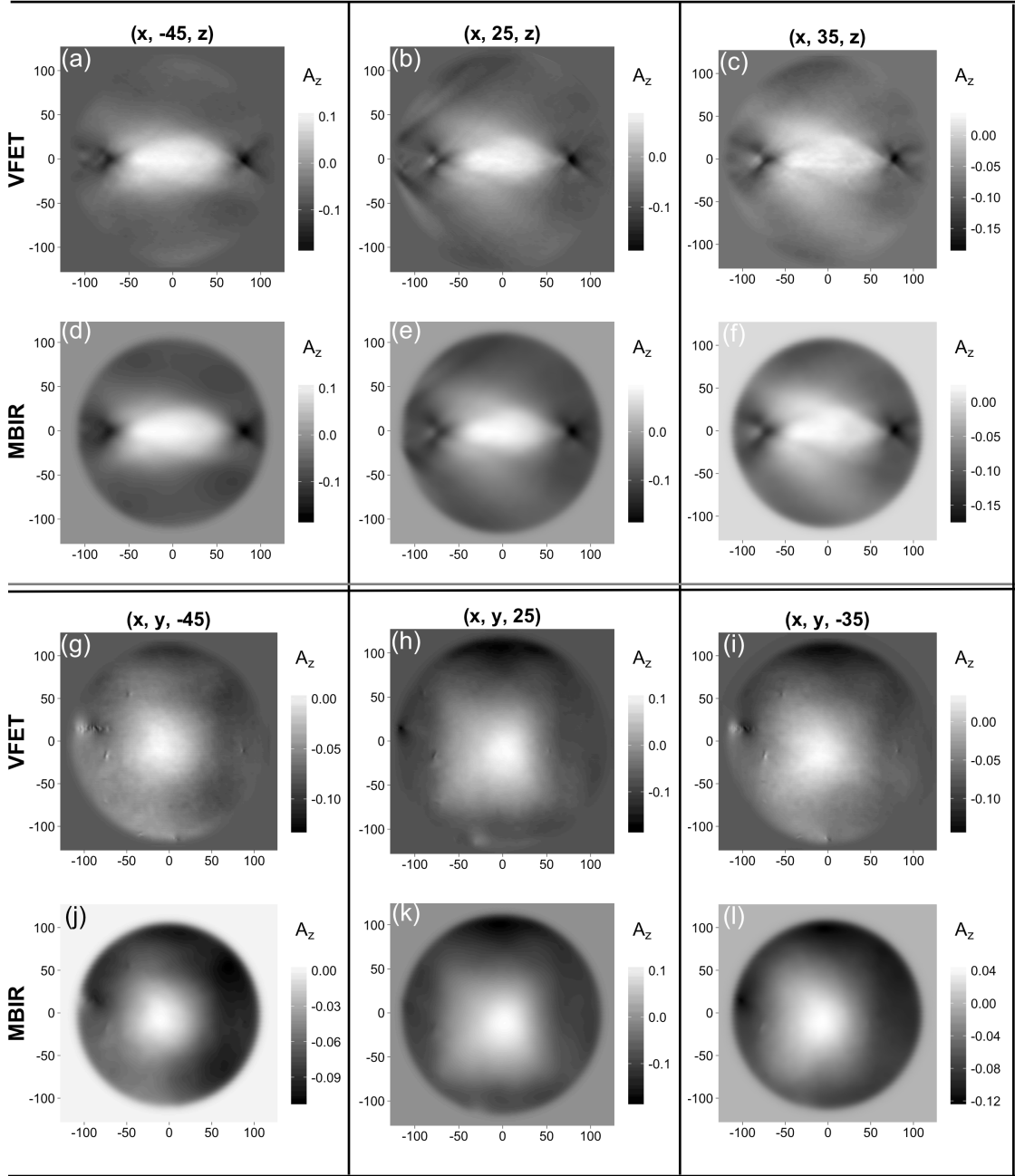
Figure 6.17: Reconstructed A_z of Py island from the VFET approach [first and third column] and the MBIR approach [second and fourth column]. The unit for $\mathbf{A}(\mathbf{r})$ is T-px where 1 px equals 3.2 nm.
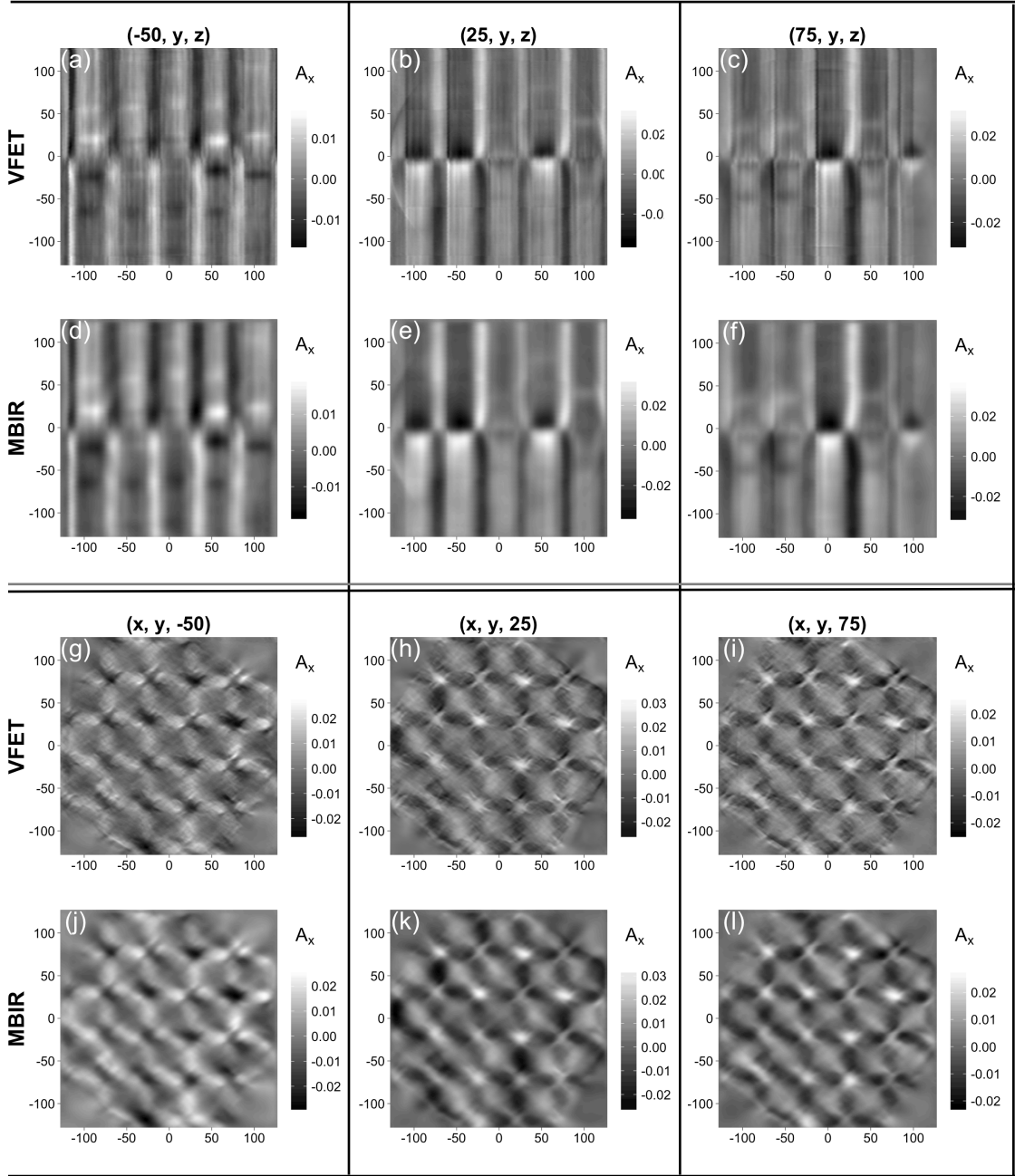
Figure 6.18: Reconstructed A_x of Py lattice from the VFET approach [first and third column] and the MBIR approach [second and fourth column]. The unit for A_x is T-px where 1 px equals 6 nm.
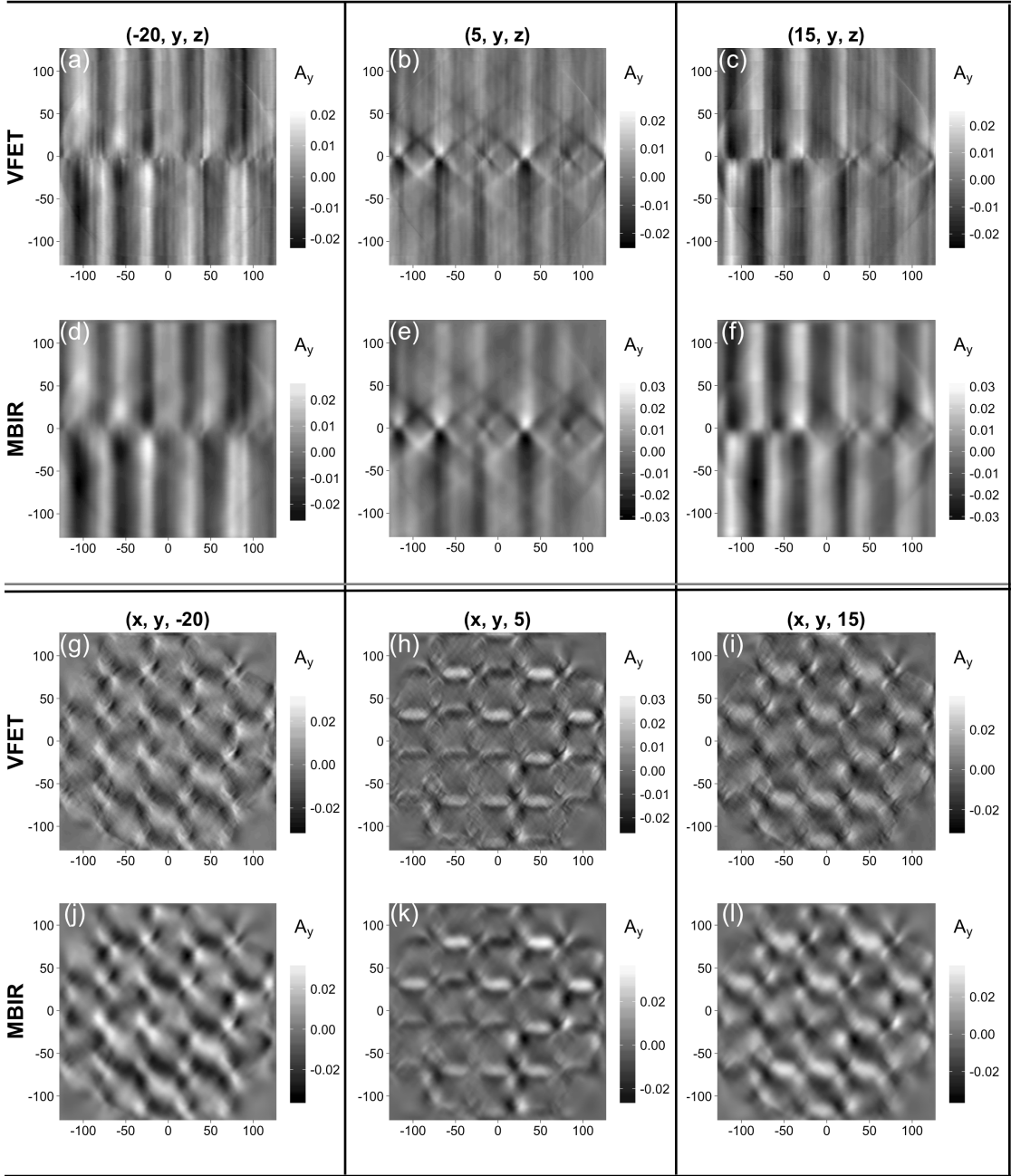
Figure 6.19: Reconstructed A_y of Py lattice from the VFET approach [first and third column] and the MBIR approach [second and fourth column]. The unit for A_y is T-px where 1 px equals 6 nm.
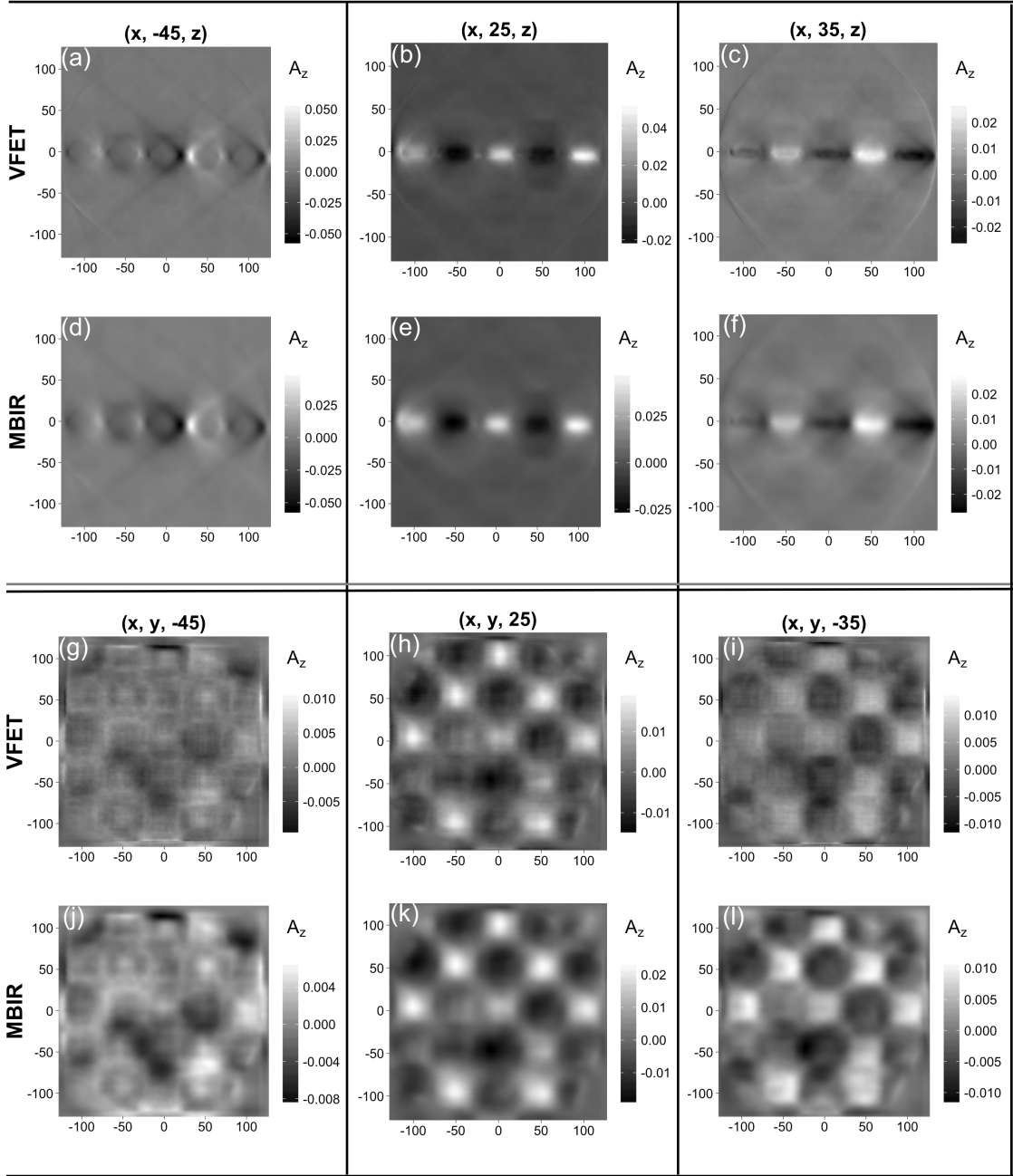
Figure 6.20: Reconstructed A_z of Py lattice from the VFET approach [first and third column] and the MBIR approach [second and fourth column]. The unit for A_z is T-px where 1 px equals 6 nm.

substantially reduced in the MBIR result (figures 6.18(j-l) & 6.19(j-l)). Furthermore, we see appropriately segmented and smoothly transitioning $\mathbf{A}(\mathbf{r})$ values in the MBIR results. The blurring artifacts observed in some of the VFET-based reconstructed regions (figures 6.20(g-i)) are considerably diminished in the MBIR results (figures 6.20(j-l)). Finally ring and streak artifacts that plague the VFET results (figures 6.18(a-c), 6.19(a-c), 6.20(a-c)) are substantially minimized in the MBIR results (figures 6.18(d-f), 6.19(d-f), 6.20(d-f)). These reconstruction gains in the MBIR-based $\mathbf{A}(\mathbf{r})$ results are observed throughout the 3D spatial region when compared to their VFET counterparts.

Since the reconstructed quantity is a 3D vector field, we conclude this section with a 3D rendering (figure 6.21) of the magnetic vector potential of Py lattice resulting from the MBIR reconstruction approach. Figure 6.21(a) shows a color-coded integrated (along the beam direction) magnetic induction map, derived from the magnetic phase shift by a gradient operation. The white rectangle delineates the region used for the 3D rendering of the vector field in figure 6.21(b). To reduce the complexity of the 3D rendering, the field vectors (shown as small cones with the appropriate orientation) are only drawn for the horizontal center plane going through the Py lattice islands and four vertical planes corresponding to the dashed lines in Figure 6.21(a). The yellow arrow indicates the viewing direction for the 3D rendering in Figure 6.21(b). The individual islands are colored according to the in-plane direction of the integrated magnetic induction following the color wheel in (a). Note that the induction directions, which are oriented along the local curl of the magnetic vector potential, are properly oriented; i.e., the opposite rotation of the vector field around the green and red islands is clearly visible, and application of the right-hand rule for the curl results in the correct direction of the integrated magnetic induction. Furthermore, the square of islands on the left front of the image, and the two squares in the back, are all in a vortex state, i.e., the magnetization of the islands circulates clockwise or counterclockwise. The corresponding section through the vector field shows vectors which are all blue ($\mathbf{A}$ pointing down) or all orange ($\mathbf{A}$ pointing up). For the square on the front right, however, two of the islands are blue, so that there is no closed vortex and the vector field is much more complex in this area, reflecting the local frustrated state of the magnetization pattern.
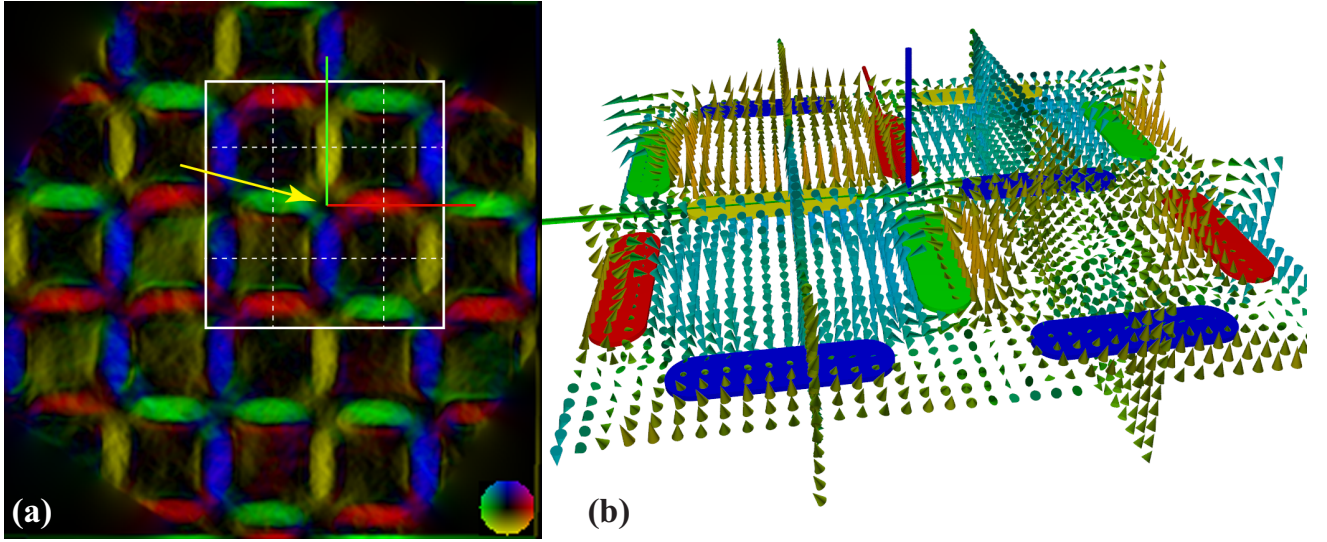
Figure 6.21: (a) Magnetic induction map of the 0° phase shift shown in Figure 6.14. (b) Schematic of islands enclosed inside the solid white lines and 3D magnetic vector potential corresponding to the dotted lines in (a).

6.4 Revisiting the hypothesis

We claimed that the MBIR framework can ameliorate the artifacts observed in the magnetic vector reconstruction obtained from the VFET approach. Our claim was based upon the fact that the MBIR approach incorporated important prior information about both the imaging system and the object being imaged instead of a mere filter-based approach such as in the case of the VFET technique. More specifically, we employed MRF to incorporate a prior idea that similar inputs have similar outputs (the nearby pixels or voxels have same values). In regards to imaging system, we formulated forward model to replicate image formation step while recording data for tomographic reconstruction. Then cost function was derived by finding a joint probability from the prior and forward models. The cost function was iteratively minimized by employing ICD technique to deduce a MAP estimate of a given reconstruction problem. Accordingly, MAP estimate of 2D Shepp-Logan phantom was determined to have 15% less error than the corresponding FBP result.

In case of vector field reconstruction, we extended the MBIR model to incorporate Coulomb gauge constraint and, subsequently, reconstructed all three components of vector potential from two tilt series. The NRMSE analysis illustrates that the MBIR approach generally reconstructs $\mathbf{A}(\mathbf{r})$ of simulated nanoparticles at $10 - 40\%$ more accurately than the VFET approach. Likewise, MBIR based vector potential of experimental datasets shows highly resolved reconstruction when compared to the corresponding result from the VFET approach. A major shortcoming of the VFET approach has been its inability to deduce a proper reconstruction for incomplete experimental dataset. VFET based vector potential determined from incomplete dataset is plagued with discrepancies such as ring artifacts, line and streak artifacts, blurring of edges and protrusions. On the contrary, the MBIR approach compensates for missing wedge of information due to its robust statistical framework. Accordingly, the aforementioned artifacts are substantially mitigated in the MBIR result. Finally, white noise, blur, and coarseness, ubiquitous in the VFET result, are considerably minimized in the MBIR results. In view of all these findings, we uphold our starting hypothesis and conclude the MBIR approach can overcome the shortcomings of the VFET approach and can accurately reconstruct magnetic vector potential.

Chapter 7

Future work

In this research work, a concerted effort was presented to determine the magnetic vector potential of nanoparticles (NPs). First we performed TEM experiments on these NPs and recorded images at different angles of inclination. Then we employed the Transport-of-Intensity Equation (TIE) formalism to extract the magnetic phase shift from these TEM images. Subsequently, we used vector tomography to reconstruct the magnetic potential of the NPs all across the 3D space. Most importantly, we incorporated Bayesian inference in our tomography model which has allowed us to ascertain the vector potential at $10 - 40\%$ more accurately than the reconstructions obtained from the previous filter-based vector field electron tomography (VFET) methodology.

Having determined one of the fundamental quantities, $\mathbf{A}$, in electrodynamics, we seek to further our investigation by determining other important quantities in the same paradigm such as the magnetic induction, $\mathbf{B}$, and the demagnetization field, $\mathbf{H}$. Magnetic induction is directly related to the vector potential by the mathematical relation, $\mathbf{B} = \nabla \times \mathbf{A}$ [38]. Likewise, we can make use of the secondary/derived definition of the vector potential which states that $\mathbf{A}$ is given by the convolution of the magnetization, $\mathbf{M}(\mathbf{r})$, with the dipolar kernel $\mathbf{r}/|\mathbf{r}|^3$ to determine $\mathbf{M}$ [96]. Finally, the relation $\mathbf{B} = \mu_o(\mathbf{M} + \mathbf{H})$ [98] can be used to ascertain the demagnetization field.

Many electrodynamics text books argue that the vector potential does not have any physical meaning and is introduced solely for the purpose of mathematical simplification of the equations while determining the electric field or magnetic field [99]. Although we
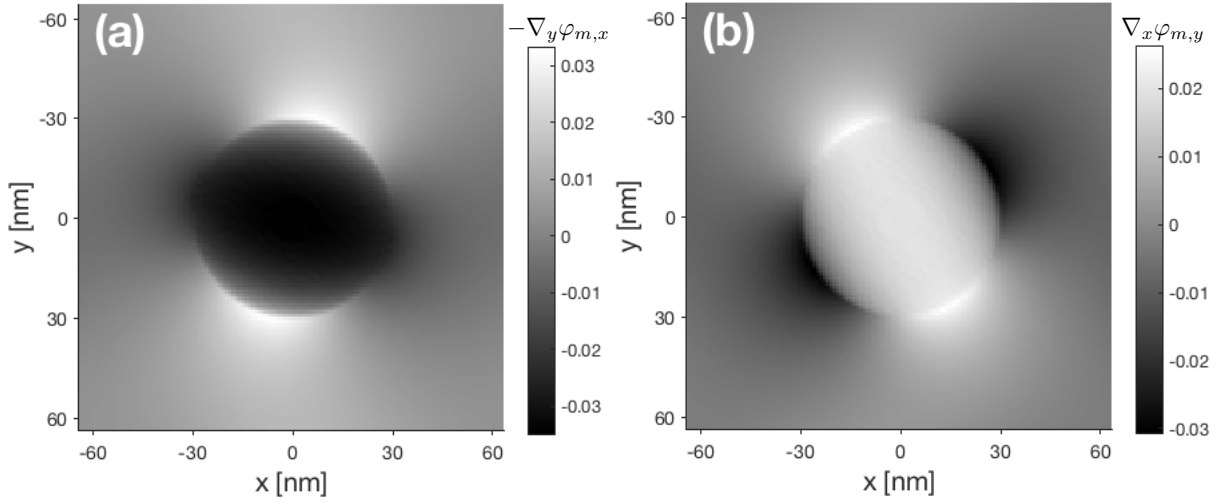
Figure 7.1: Illustration of projection data obtained as the gradient of phase shift of (a) x tilt as Proj. of B_x and (b) y tilt as Proj of B_y of the spherical magnetic NP in figure 4.7a. The tilt angle is $0°$.

are not looking to establish the physical significance of the vector potential, we do want to emphasize its significance for it shows up in different calculations such as the Aharonov-Bohm effect, the magnetic induction, and the magnetization. More information on how we seek to utilize the vector potential to determine other important electrodynamical quantities in the future can be found under the headings below:

7.1   Magnetic Induction

We make use of the Aharonov-Bohm relation [39] in eq. 2.3 and the fact that the curl of $\mathbf{A}$ yields $\mathbf{B}$ [38] to obtain the following relations between the magnetic phase shift, φ_m, and the magnetic induction, $\mathbf{B}$ [53]:

$$\frac{\partial}{\partial y}\varphi_m(x,y) = -\left(\frac{e}{h}\right)\int_{-\infty}^{\infty} B_x(x,y,z)dz, \tag{7.1}$$

$$\frac{\partial}{\partial x}\varphi_m(x,y) = \left(\frac{e}{h}\right)\int_{-\infty}^{\infty} B_y(x,y,z)dz. \tag{7.2}$$
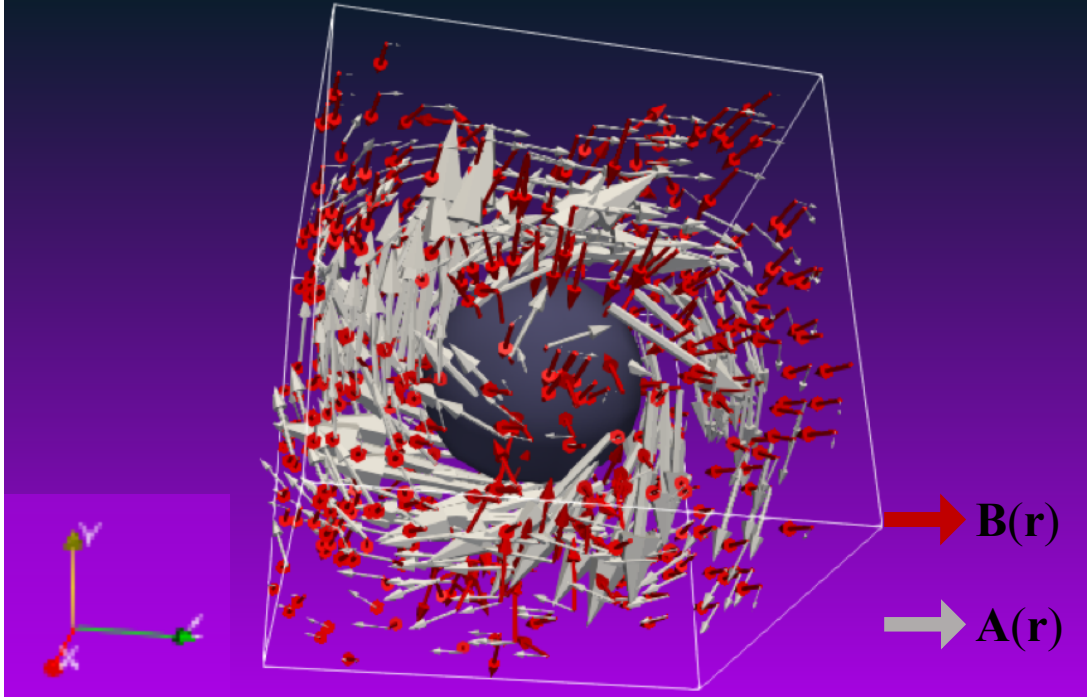
Figure 7.2: 3D representation of vector potential and magnetic induction of a spherical MNP with 30 nm radius and magnetization direction of $\left[\cos\frac{\pi}{6}, \sin\frac{\pi}{6}, 0\right]$. Silver arrows correspond to vector potential, $\mathbf{A(r)}$, and red arrows correspond to magnetic induction, $\mathbf{B(r)}$.

It can be inferred from eqs. 7.1 and 7.2 that taking the partial derivative of the magnetic phase shift w.r.t y yields projection measurements of B_x and that w.r.t x yields projection measurements of B_y. Additionally, $\nabla_y\varphi$ is calculated on the x tilt series and $\nabla_x\varphi$ is carried out on the y tilt series to determine the sinograms for B_x and B_y respectively. Figure 7.1 depicts the gradients of the phase shift at $0°$ projection in x and y directions of the spherical magnetic nanoparticle (MNP) illustrated in figure 4.7a. Next, we employ the MBIR algorithm to reconstruct B_x and B_y separately. Then the third component of magnetic induction, B_z, is determined by utilizing Gauss's law for the Magnetic field $(\nabla \cdot \mathbf{B} = 0)$ as:

$$B_z = -\int \left(\frac{\partial B_x}{\partial x} + \frac{\partial B_y}{\partial y}\right) dz.$$

Now that we have determined the vector potential and the magnetic induction of the

spherical NP, let us visualize how the vector field looks like in the 3D space. This 3D vector visualization is, again, completed with the aid of the ParaView [95] plotting tool and figure 7.2 illustrates the plot. In order to aid the visualization, we have considered only 500 points while depicting the vector fields of $\mathbf{B}(\mathbf{r})$ and $\mathbf{A}(\mathbf{r})$. Accordingly, one can observe that $\mathbf{B}(\mathbf{r})$ (red arrows) is pointing in the negative y direction and $\mathbf{A}(\mathbf{r})$ (silver arrows) is rotating around the magnetic induction in accordance to the right hand rule. This result adheres to the basics of electromagnetism that the curl of $\mathbf{A}$ yields $\mathbf{B}$ and validates our tomography-based approach to resolve all the quantities involved in magnetism at the nanoscale length. We aim to determine the magnetic induction of NPs with non-uniform magnetization states in future. Futhermore, the next section provides a sneak peek into how we aim to resolve magnetization and demagnetization fields using the MBIR based vector tomography.

7.2 Some thoughts on resolving H and M

The magnetic vector potential, $\mathbf{A}(\mathbf{r})$, is related to the magnetization, $\mathbf{M}(\mathbf{r})$, by the following mathematical relation [61]:

$$\mathbf{A}(\mathbf{r}) = \frac{\mu_o}{4\pi} \int \mathbf{M}(\mathbf{r}') \times \frac{\mathbf{r} - \mathbf{r}'}{|\mathbf{r} - \mathbf{r}'|^3} d^3\mathbf{r}'. \tag{7.3}$$

Our collaborators at Purdue University have already carried out extensive work to tomographically invert eq. 7.3 and calculate $\mathbf{M}(\mathbf{r})$ from the reconstructed vector potential. Thus, we aim to incorporate their tomography module to reconstruct the magnetization. Once $\mathbf{M}(\mathbf{r})$ is determined, we can use the relation $\mathbf{B} = \mu_o(\mathbf{M} + \mathbf{H})$ to ascertain the demagnetization field, $\mathbf{H}(\mathbf{r})$. Since our approach is numerical in nature, we predict that this approach should resolve the demagnetization field for arbitrary shape and non-uniform magnetization. A good volume of work has, already, been done by M. Beleggia et al. [98] and S. Tandon et al. [100, 101] to determine the demagnetization tensor field of arbitrary shape with uniform magnetization. However, determination of the demagnetization field of non-uniformly magnetized particles has still been elusive due to obvious limitation of analytical computation. Thus, it will be quite fascinating to see on what level of accuracy

our numerical based vector tomography will be able to deduce the demagnetization field of known magnetization states.

Bibliography

[1] V. N. Nikiforov and E. Y. Filinova 2009. Biomedical Applications of Magnetic Nanoparticles. S. P. Gublin. In: editor. Magnetic Nanoparticles. Strauss GmbH: Morlenbach Wiley-VCH. p. 393-444.

[2] G. N. Ramachandran and A. V. Lakshminarayanan. Three-dimensional reconstruction from radiographs and electron micrographs: application of convolutions instead of Fourier transforms. *Proceedings of the National Academy of Sciences*, 68(9):2236–2240, Sept. 1971.

[3] C. A. Bouman. *Model Based Image Processing.* 2013.

[4] S. P. Gubin. 2004. Introduction. S. P. Gublin. In: editor. Magnetic Nanoparticles. Strauss GmbH: Morlenbach Wiley-VCH. p. 1-19.

[5] M. D. Ventra, S. Evoy, and J. R. Heflin. 2009. Introduction. M. D. Ventra, S. Evoy and J. R. Heflin In: editor. Introduction to Nanoscale Science and Technology. Boston (MA): Kluwer Academic Publisher. p. 1-3.

[6] P. Tartaj, S. Veintemillas-Verdaguer, C. J. Serna, and other. The preparation of magnetic nanoparticles for applications in biomedicine. *J. Phys. D: Appl. Phys.*, 36:R182 – R197, June 2003.

[7] A. Akbarzadeh, M. Samiei, and S. Davaran. Magnetic nanoparticles: preparation, physical properties, and applications in biomedicine. *Nanoscale Res. Lett*, 7:1–13, 2012.

[8] J. P. Dailey, J. P. Phillips, C. Li, and J. S. Riffle. Synthesis of silicone magnetic fluid for use in eye surgery. *J. Magn. Magn. Mater.*, 194:140–148, 1990.

[9] S. Bamrungsap, J. A. Phillips, X. Xiong, et al. Magnetically Driven Single DNA Nanomotor. *Small*, 7(5):601–605, 2011.

[10] A. Jordan, P. Wust, R. Scholz, et al. Cellular uptake of magnetic fluid particles and their effects on human adenocarcinoma cells exposed to AC magnetic fields in vitro. *Int. J. Hyperthermia*, 12(6):705–722, Dec. 1996.

[11] I. S. Neilsen, M. Horsman, and J. Overgaard. A future for hyperthermia in cancer treatment? *Eur. J. Cancer*, vol. 37, no. 13(13):1587–1589, Sep. 2001.

[12] P. Guardia, B. Batlle-Brugal, A. G. Roca, et al. Surfactant effects in magnetite nanoparticles of controlled size. *J. Magn. Magn. Mater.*, 316(2):e756–e759, Jul. 2007.

[13] A. G. Roca, M. P. Morales, K. O'Grady, and C. J. Serna. Structural and magnetic properties of uniform magnetite nanoparticles prepared by high temperature decomposition of organic precursors. *Nanotechnology*, 17:2783, May 2006.

[14] N. Pérez, F. Bartolomé, L. M. García, et al. Nanostructural origin of the spin and orbital contribution to the magnetic moment in $Fe_{3-x}O_4$ magnetite nanoparticles. *App. Phys. Lett.*, 94(9):093108–3, May 2009.

[15] S. N. Piramanayagam, M. Ranjbar, R. Sbiaa, et al. Characterization of high-density bit-patterned media using ultra-high resolution magnetic force microscopy. *Phys. Status Solidi*, 6(3):141–143, Feb. 2012.

[16] Hitachi News Release - Hitachi achieves nanotechnology milestone for quadrupling terabyte hard drive. 2007.

[17] R. A. Griffiths, A. Williams, C. Oakland, et al. Directed self-assembly of block copolymers for use in bit patterned media fabrication. *Journal of Physics D: Applied Physics*, 46(50):503001, 2013.

[18] M. D. Graef 2001. Lorentz Microscopy: Theoretical Basis and Image Simulations. M. D. Graef, and Y. Zhu In: editor. Magnetic Imaging and Its Applications to Materials. Sang Diego (CA): Academic press. p. 1-25.

[19] N. D. Jonge, Y. Lamy, K. Schoots, and T. H. Oosterkamp. High brightness electron beam from a multi-walled carbon nanotube. *Nature*, 420(6914):393–395, Nov. 2002.

[20] L. Gao, L. P. Yue, T. Yokota, et al. Focused ion beam milled CoPt magnetic force microscopy tips for high resolution domain images. *IEEE*, 40(4):2194–2196, Jul. 2004.

[21] K. Tanaka, M. Yoshimura, and K. Ueda. High-Resolution Magnetic Force Microscopy Using Carbon Nanotube Probes Fabricated Directly by Microwave Plasma-Enhanced Chemical Vapor Deposition. *J. of Nanomaterials*, vol. 2009, Article ID 147204:4 pages, Oct. 2009.

[22] R. H. Dee. Magnetic tape for data storage: an enduring technology. *IEEE*, 96(11):1775–1785, Nov. 2004.

[23] D. Wolf, H. Lichte, G. Pozzi, P. Prete, and N. Lovergine. Electron holographic tomography for mapping the three-dimensional distribution of electrostatic potential in III-V semiconductor nanowires. *Appl. Phys. Lett.*, 98:264103–3, 2011.

[24] A. Lubk, D. Wolf, P. Simon, et al. Nanoscale three-dimensional reconstruction of electric and magnetic stray fields around nanowires. *Appl. Phys. Lett.*, 105: 173110–4, 2014.

[25] M. Faraji, Y. Yamini, and M. Rezaee. Magnetic nonoparticles: synthesis, stabilization, functionalization, characterization and applications. *J. Iran. Chem. Soc.*, 7(1):1–37, Mar. 2009.

[26] Y. Acremann, C. H. Back, M. Buess, et al. Imaging precessional motion of the magnetization vector. *Science*, 290:492–495, 2000.

[27] S. B. Choe, Y. Acremann, A. Scholl, et al. Vortex core-driven magnetization dynamics. *Science*, 304:420–422, 2004.

[28] A. Wachowiak, J. Wiebe, M. Bode, et al. Direct observation of internal spin structure of magnetic vortex cores. *Science*, 298: 577–580, 2002.

[29] R. Streubel, P. Fischer, F. Kronast, et al. Magnetism in curved geometries. *Journal of Physics D: Applied Physics*, 49(36):363001, Aug. 2016.

[30] R. Streubel, F. Kronast, P. Fischer, et al. Retrieving spin textures on curved magnetic thin films with full-field soft X-ray microscopies. *Nature communications*, 6:1–11, Jul. 2015.

[31] C. Phatak. *On the Use of Phase Reconstructed Vector Field Tomography for the 3-D Study of Magnetic Materials.* Ph.D Thesis, Carnegie Mellon University, 2009.

[32] P. A. Midgley and R. E. Dunin-Borkwski. Electron tomography and holography in materials science. *Nature Materials*, 8:271–280, April 1997.

[33] M. R. McCartney, R. E. Dunnin-Borkowski, and J. D. Smith 2001. Electron Holography and Its Applications to Magnetic Materials. M. D. Graef, and Y. Zhu In: editor. Magnetic Imaging and Its Applications to Materials. Sang Diego (CA): Academic press. p. 27-67.

[34] C. Phatak, M. Beleggia, and M. D. Graef. Vector field electron tomography of magnetic materials: Theoretical development. *Ultramicroscopy*, vol. 108: 503–513, May 2008.

[35] M. D. Graef. *Introduction to convectional Transmission Electron Microscopy.* Cambridge University Press, Cambridge, UK, 2003.

[36] E. J. Kirkland. *Advanced Computing in Electron Microscopy.* Springer Science & Business Media, Ithaca, NY, 2010.

[37] L. Reimer. *Transmission Electron Microscopy.* Springer-Verlag, Berlin, 1993.

[38] J. D. Jackson. *Classical Electrodynamics.* 2nd Ed. Wiley, NY, 1975.

[39] Y. Aharonov and D. Bohm. Significance of electromagnetic potentials in the quantum theory. *The Phys. Rev.*, 115(3):485–491, August 1959.

[40] J. C. H. Spence. *Experimental High Resolution Electron Microscopy.* 2nd Ed. Oxford Univ. Press, NY, 1988.

[41] D. Paganin and K. Nugent. Noninterferometric phase imaging with partially coherent light. *Phys. Rev. Lett.*, 80(3):2586, March 1998.

[42] E. Humphrey, C. Phatak, A. K. Petford-Long, and M. D. Graef. Separation of electrostatic and magnetic phase shits using a modified transport-of-intensity equation. *Ultramicroscopy*, 139:5–12, Jan. 2014.

[43] R. Gordan. A Tutorial on ART (Algebraic Reconstruction Techniques). *IEEE Trans. on Nuclear Science*, NS-21:78–93, June 1974.

[44] L. A. Shepp and B. F. Logan. The Fourier Reconstruction of a Head Section. *IIEEE Trans. on Nuclear Science*, 21:21–43, 1974.

[45] Wikipedia. Projection-slice theorem. `https://en.wikipedia.org/wiki/Projection-slice_theorem`, November 2015.

[46] N. Gubareni (2009). *Algebraic Algorithms for Image Tomographic Reconstruction from Incomplete Projection Data.* Engineering the Computer Science and IT, Safeeullah Soomro (Ed.), ISBN: 978-953-307-012-4, InTech, DOI: 10.5772/7757, Available from: http://www.intechopen.com/books/engineering-the-computer-science-and-it/algebraic-algorithms-for-image-tomographic-reconstruction-from-incomplete-projection-data.

[47] A. C. Kak and M. Slaney. *Principles of Computerized Tomographic Imaging.* Classics in Applied Mathematics. Society for Industrial and Applied Mathematics, Reading, Massachusetts, 2009.

[48] M. Lyra and A. Ploussi. Filtering in SPECT Image Reconstruction. *International Journal of Biomedical Imaging*, vol. 2011, Article ID 693795:14 pages, April 2011.

[49] A. Kingston and I. Svalbe. 2006. Discrete Radon Tranform Formalisms. In: Perter W. Hawkes, editor. Advances in Imaging and Electron Physics. Vol. 139. California (CA): Elsevier Academic Press publications. p. 100-122.

[50] A. H. Mahnken, R. Raupach, J. E. Wildberger, et al. A New Algorithm for Metal Artifact Reduction in Computed Tomography: In Vitro and In Vivo Evaluation After Total Hip Replacement. *Investigative Radiology*, 38:769–775, Dec. 2003.

[51] S. Alenius and U. Ruotsalainen. Bayesian image reconstruction for emission tomography based on median root prior. *European Journal of Nuclear Medicine*, 24(3):258–265, March 1997.

[52] T. M. Dension and J. Gregor. Modified simultaneous iterative reconstruction technique for faster parallel computing. *IEEE Nuclear Science Symposium Conference Record*, page p. 2715, 2005.

[53] C. Phatak and D. Gürsoy. Iterative reconstruction of magnetic induction using Lorentz transmission electron tomography. *Ultramicroscopy*, 150:54–64, July 2015.

[54] T. Schuster. 20 years of imaging in vector field tomography: a review.

[55] P. Juhlin. Principles of Doppler tomography, tech. report, Center for Mathematical Sciences, Lund Institute of Technology. SE-221 00 Lund, 1992.

[56] S. J. Norton. Tomographic reconstruction of 2-D vector fields: application to flow imaging. *Geophysical Journal*, 97:161–168, 1988.

[57] S. J. Lade, D. Paganin, and M. J. Morgan. Electron tomography of electromagnetic fields, potentials and sources. *Optics Communications*, 253:392–400, April 2005.

[58] S. J. Lade, D. Paganin, and M. J. Morgan. 3-D Vector tomography of Doppler-transformed fields by filtered-backprojection. *Optics Communications*, 253:382–391, March 2005.

[59] Z. D. C. Kemp, T. C. Petersen, D. M. Paganin, et al. Analysis of noise-induced errors in vector-field electron tomography. *Phys. Rev.*, A 90:023859, August 2014.

[60] S. S. Brandt. 2006. Markerless Alignment in Electron Tomography. In: Joachim Frank, editor. Algebraic Algorithms for Image Tomographic Reconstruction from Incomplete Projection Data. Albany (NY): Springer. p. 187-216.

[61] M. Beleggia and Y. Zhu. Electron-optical phase shift of magnetic nanoparticles. I. Basic concepts. *Philosophical Magazine*, 83:1045–1057, March 2003.

[62] R. P. Yu, M. J. Morgan, and D. M. Paganin. Lorentz-electron vector tomography using two and three orthogonal tilt series. *Physical Review*, A 83:0238131–0238139, Feb. 2011.

[63] E. Humphrey and M. D. Graef. On the computation of the magnetic phase shift for magnetic nano-particles of arbitrary shape using a spherical projection model. *Ultramicroscopy*, 129: 36–41, March 2013.

[64] Wikipedia. Root-mean-square deviation. `https://en.wikipedia.org/wiki/Root-mean-square_deviation`, February 2016.

[65] C. M. Bishop. *Pattern Recognition and Machine Learning*. Information Science and Statistic. Springer, Cambridge, U.K, 2006.

[66] D. J. C. MacKay. *Information Theory, Inference and Learning Algorithms*. Cambridge University Press, Cambridge, U.K, 2005.

[67] C. Brown. An Introduction to Bayes' Theorem. `http://www.trinity.edu/cbrown/bayesweb/index.html`, March 2016.

[68] L. Wasserman. *All of Statistics: A Concise Course in Statistical Inference*. Springer, Pittsburgh, P.A, 2005.

[69] K. P. Murphy. *Machine Learning: A probabilistic Perspective*. The MIT Press, Cambridge, MA, 2012.

[70] C. Bouman and K. Sauer. A generalized Gaussian image model for edge-preserving MAP estimation. *IEEE Trans. Image Process*, 2(3):296–310, Jul. 1993.

[71] H. Derin, H. Elliot, R. Christi, and D. Geman. Bayes Smoothing Algorithms for Segmentation of Binary Images Modeled by Markov Random Fields. *IEEE Trans. Pattern Anal. and Mach. Intell.*, PAMI-6, 1984.

[72] S. Geman and D. Geman. Stochastic Relaxation, Gibbs Distributions, and the Bayesian Restoration of Images. *IEEE Trans. Pattern Anal. and Mach. Intell.*, PAMI-6(6):721–741, Nov. 1984.

[73] J. Besag. On the Statistical Analysis of Dirty Pictures. *J. Roy. Statist. Soc. B*, 48(3):259–302, 1986.

[74] H. Derin and H. Elliott. Modeling and Segmentation of Noisy and Textured Images Using Gibbs Random Fields. *IEEE Tmns. Trans. Pattern Anal. and Mach. Intell.*, PAMI-9:39–55, Jan. 1987.

[75] J. Besag. Spatial Interaction and the Statistical Analysis on Lattice Systems. *J. Roy. Statist. Soc. B*, 36:192–326, 1974.

[76] R. Kindermann and J. L. Snell. *Markov Random Fields and Their Applications.* American Mathematical Society, Providence, RI, 1980.

[77] G. T. Herman, H. Hurwitz, A. Lent, and H. P. Lung. On the Bayesian Approach to Image Reconstruction. *Info. and Cont.*, 42:60–71, 1979.

[78] K. M. Hanson and G. W. Wecksung. Bayesian Approach to Limited-Angle Reconstruction in Computed Tomography. *J. Opt. Soc. Am.*, 73(11):1501–1509, Nov. 1983.

[79] E. Levitan and G. T. Herman. A Maximum A Posteriori Probability Expectation Maximization Algorithm for Image Reconstruction in Emission Tomography. *IEEE Tmns. Med. Imag.*, MI-6(3):185–192, 1987.

[80] A. Tikhonov and V. Arsenin. *Solutions of Ill-Posed Problems.* Winston and Sons, New York, 1977.

[81] S. Boyd and L. Vandenberghe. *Convex Optimization.* Cambridge University Press, New York, 2009.

[82] Z. Yu, J. B. Thibault, C. A. Bouman, K. D. Sauer, and J. Hsieh. Fast model-based X-ray CT reconstruction using spatially non homogenous ICD optimization. *IEEE Trans. on Image Processing*, 20(1):161–175, Jan. 2011.

[83] L. Kantorovich and G. Akilov. *Functional Analysis in Normed Spaces*. Fitzmatgiz, Moscow, 1959.

[84] J. Fessler, E. Ficaro, N. Clinthorne, and K. Lange. Grouped-coodinate ascent algorithms for penalized-likelihood transmission image reconstruction. *IEEE Trans. on Image Processing*, 12(1):44–57, Mar. 2003.

[85] J. Zheng, S. S. Saquib, K. Sauer, and C. A. Bouman. Parallelizable Bayesian tomography algorithms with rapid, guaranteed convergence. *IEEE Trans. on Image Processing*, 9(10):1745–1759, Oct. 2000.

[86] C. A. Bouman. *Digital image processing laboratory: MAP image restoration*. Purdue University, West Lafayette, IN, 2010. Print.

[87] K. Sayer and C. A. Bouman. Bayesian estimation from projection with low photon dosages. *IEEE*, M6.6:2593–2596, 1991.

[88] J. B. Thibault, K. Sayer, and C. A. Bouman. Newton-style optimization for emission tomographic estimation. *Journal of Electronic Imaging*, 9(3):269–282, July 2000.

[89] A. Mohan, S. V. Venkatakrishnan, L. F. Drummy, et al. Model-Based Iterative Reconstruction for Synchrotron X-ray tomography. *in Acoustics, Speech and Signal Processing (ICASSP), 2014 IEEE International Conference on*, May 2014.

[90] K. Sayer and C. Bouman. A local update strategy for iterative reconstruction from projections. *IEEE Trans. on Signal Processing*, 41(2):534–548, Feb. 1993.

[91] T. Frese. *Multiresolution image modeling and Bayesian reconstruction algorithms with applications to emission tomography*. Ph.D Thesis, Purdue University, 2001.

[92] J. B Thibault, K. D. Sauer, C. A. Bouman, and J. Hsieh. A three-dimensional statistical approach to improved image quality for multislice helical CT. *Medical Physics*, 34(11):4526–4544, Nov. 2007.

[93] T. Elfving, P. C. Hansen, and T. Nikazad. Semi-convergence and relaxation parameters for projected SIRT Algorithms. *SIAM J. Sci. Comput.*, 34(4):A2000–17, July 2012.

[94] T. Elfving, P. C. Hansen, and T. Nikazad. Semi-convergence properties of Kaczmarz's method. *Inverse Problems*, 30:055007, May 2014.

[95] A. Henderson. Paraview Guide, A Parallel Visualization Application. Kitware Inc. http://www.paraview.org/, March 2017.

[96] C. Phatak, A. K. Petford-Long, and M. D. Graef. Three-dimensional study of the vector potential of magnetic structures. *Phys. Rev. Lett.*, vol. 104(25):253901, Feb. 2010.

[97] C. Phatak, A. K. Petford-Long, O. Heinonen, M. Tanase, and M. D. Graef. Nanoscale structure of the magnetic induction at monopole defects in artificial spin-ice lattices. *Phys. Rev.*, B 83:174431, May 2011.

[98] M. Beleggia and M. D. Graef. On the computation of the demagnetization tensor field for an arbitrary particle shape using a Fourier space approach. *Journal of magnetism and magnetic materials*, 263(1):L1–L9, Feb. 2003.

[99] M. D. Semon and J. R. Taylor. Thoughts on the magnetic vector potential. *American Journal of Physics*, 64(11):1361–1369, 1996.

[100] S. Tandon, M. Beleggia, Y. Zhu, and M. D. Graef. On the computation of the demagnetization tensor for uniformly magnetized particles of arbitrary shape. Part I: Analytical approach. *Journal of magnetism and magnetic materials*, 271(1):9–26, July 2004.

[101] S. Tandon, M. Beleggia, Y. Zhu, and M. D. Graef. On the computation of the demagnetization tensor for uniformly magnetized particles of arbitrary shape. Part

II: numerical approach. *Journal of magnetism and magnetic materials*, 271(1):27–38, July 2004.

[102] Y. LeCun, Y. Bengio, and G. Hinton. Deep Learning. *Nature*, 521:436–444, May 2013.

[103] T. M. Mitchell. *Machine Learning*. McGraw-Hill Science/Engineering/Math, Ithaca, NY, 1997.

[104] T. Zhao and Y. Wang. A Neural-Network Based Autonomous Navigation System Using Mobile Robots. *IEEE*, pages 1101–1106, March 2013.

[105] R. H. Nielsen. Theory of the backpropagation neural network. *Neural Networks*, 1(Supplement-1):445–448, 1988.

[106] A. Bevilacqua, D. Bollini, R. Campanini, N. Lanconelli, and M. Galli. A new approach to image reconstruction in positron emission tomography using artificial neural networks. *International Journal of Modern Physics C*, 9(1):71–85, Feb. 1998.

[107] J. P. Kerr and E. B. Bartlett. Neural network reconstruction of single-photon emission computed tomography images. *Journal of Digital Imaging*, 8(3):116–126, Aug. 1995.

[108] C. E. Floyd. An artificial neural network for SPECT image reconstruction. *IEEE Trans. on Med. Imag.*, 8(3):116–126, Aug. 1995.

[109] D. C. Durairaja, M. C. Krishnab, and R. Murugesan. A neural network approach for image reconstruction in electron magnetic resonance tomography. *Computers in Biology and Medicine*, 37:1492–1501, Jan. 2007.

[110] P. Paschalis, N. D. Giokaris, A. Karabarbounis, et al. Tomographic image reconstruction using artificial neural networks. *Nucl. Instrum. Meth. Phys. Res. A*, 527(1-2):211–215, July 2004.

[111] Wikipedia. Nervous system. `https://en.wikipedia.org/wiki/Nervous_system`, April 2017.

[112] D. V. D. Sompel, L. S. Sasportas, J. V. Jokerst, and S. S. Gambhir. Comparison of Deconvolution Filters for Photoacoustic Tomography. *PLoS one*, 11(3):e0152597, March 2016.

Appendix A

Proof of Fourier Slice Theorem

The Fourier Slice Theorem discussed in 3.1.2 and noted from reference [45] highlights that if:

$$F(u,v) = \mathcal{F}(f(x,y)) \ \& \ P_\theta(\rho) = \mathcal{F}(P_\theta(t)) \text{ then } P_\theta(\rho) = \mathcal{F}(\rho\cos(\theta), \rho\sin(\theta)).$$

Here, $\mathcal{F}(.)$ is a Fourier transform operator.

We begin the proof by noting that

$$P_\theta(t) = \int\limits_{-\infty}^{\infty} f(R_\theta\,(t,s))ds. \tag{A.1}$$

Likewise,

$$
\begin{aligned}
(x,y) &= R_\theta\,(t,s) \\
(t,s) &= R_\theta^{-1}\,(x,y) \\
&= R_{-\theta}\,(x,y) \\
&= \begin{bmatrix} \cos(\theta) & \sin(\theta) \\ -\sin(\theta) & \cos(\theta) \end{bmatrix} \begin{bmatrix} x \\ y \end{bmatrix} \\
&= \begin{bmatrix} x\cos(\theta) + y\sin(\theta) \\ -x\sin(\theta) + y\sin(\theta) \end{bmatrix}
\end{aligned}
\tag{A.2}
$$

Also,

$$
\begin{aligned}
dsdt &= \left| \frac{\partial(t,s)}{\partial(x,y)} \right| dxdy \\[2mm]
&= \left| \begin{array}{cc} \frac{\partial t}{\partial x} & \frac{\partial t}{\partial y} \\[2mm] \frac{\partial t}{\partial x} & \frac{\partial t}{\partial y} \end{array} \right| dxdy \\[2mm]
&= \left| \begin{array}{cc} \frac{\partial(x\cos(\theta)+y\sin(\theta))}{\partial x} & \frac{\partial(x\cos(\theta)+y\sin(\theta))}{\partial y} \\[2mm] \frac{\partial(-x\sin(\theta)+y\sin(\theta))}{\partial x} & \frac{\partial(-x\sin(\theta)+y\sin(\theta))}{\partial y} \end{array} \right| dxdy \\[2mm]
&= \left| \begin{array}{cc} \cos(\theta) & \sin(\theta) \\[2mm] -\sin(\theta) & \cos(\theta) \end{array} \right| dxdy \\[2mm]
&= dxdy \qquad\qquad\qquad\qquad\qquad\qquad\qquad\qquad\qquad (A.3)
\end{aligned}
$$

Finally,

$$
\begin{aligned}
P_\theta(\rho) &= \int_{-\infty}^{\infty} P(t)e^{-2\pi it\rho}dt \\[2mm]
&= \int_{-\infty}^{\infty} \left[\int_{-\infty}^{\infty} f\left(R_\theta \begin{bmatrix} t \\ s \end{bmatrix}\right)ds \right] e^{-2\pi it\rho}dt \qquad\qquad \text{from } (A.1) \\[2mm]
&= \int_{-\infty}^{\infty}\int_{-\infty}^{\infty} f(x,y)e^{-2\pi i\rho t}dsdt \\[2mm]
&= \int_{-\infty}^{\infty}\int_{-\infty}^{\infty} f(x,y)e^{-2\pi i\rho(x\cos(\theta)+y\sin(\theta))}dxdy \qquad\qquad \text{from } (A.2) \text{ and } (A.3) \\[2mm]
&= \mathcal{F}(\rho\cos(\theta),\rho\sin(\theta)) \qquad\qquad\qquad\qquad\qquad\qquad \square
\end{aligned}
$$

Appendix B

Neural Net based Filtered Backprojection

So far, we have described tomographic methods such as Backprojection (BP), Filtered Backprojection (FBP), Simultaneous Iterative reconstruction technique (SIRT) and Model based iterative technique (MBIR). Still there are other techniques to perform tomographic reconstruction. One such technique is Artificial Neural Network (ANN) based tomographic reconstruction.

Over the years, ANN have garnered enormous attraction in the field of machine learning where researchers have used neural networks (NN) to solve wide variety of tasks in computer vision [102], speech recognition [103], autonomous navigation system [104] etc. The power of ANN resides in networks' ability to learn difficult functions or functional relationships that are otherwise hard to evaluate [105]. Consequently, researchers have started employing ANN image diagnostics, image filtering, and PET and SPECT based tomographic image reconstruction [106, 107, 108, 109].

ANN based implementation is completed in two phases. The first phase is learning phase or network training step and the second phase is classification or prediction phase. The computational run time needed to train the network can be time consuming. However, once the network is trained, it can be re-applied to similar type of data set to yield result at a relatively fast pace [110]. Accordingly, we seek to assist the FBP approach by incorporating ANN to reduce artifacts and noise in reconstruction without the com-
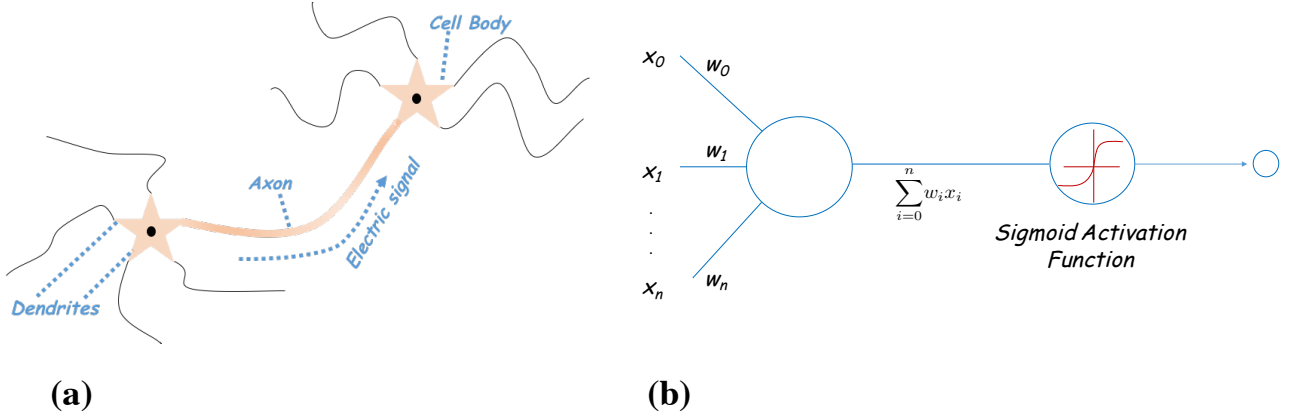
Figure B.1: An illustration of structure of a typical (a) neuron in our nervous system and (b) perceptron for binary classification tasks.

putational or algorithmic complexity of iterative techniques such as MBIR or SIRT. A detailed analysis of how we incorporate ANN to improve FBP results is provided under the headings below.

B.1   Representation of Neural Networks

Neural networks, as the name suggests, inherit mathematical representation from biological system [65]. Our nervous system functions by rapid transmission of chemicals from dendrites to cell body. The transmitted chemicals accumulate in the vicinity of the cell body and once a critical value is reached, the cell body fires output signals. These signals are transferred by axons to other cell bodies. The process of reception and transmission of signals occurs repeatedly - millions to billions times per second - to perform different bodily functions [111]. In a similar manner, a neural networks framework incorporates activation function that fires the summation of input signals once a certain threshold is reached. An illustration of a simplest form of ANN setup called perceptron and its similarity with the structure of a neuron in nervous system is provided in Figure B.1.

Typical neural networks (NN) used for tomography purposes are based on supervised, feed-forward, fully connected, back propagation scheme. The feed-forward network is analogous to forward projection part of tomography where information is learned from
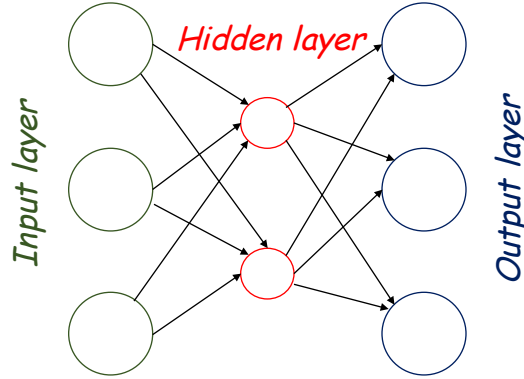
Hidden layer

Input layer

Output layer

Figure B.2: A depiction of multilayer perceptron (feed forward network) with input, hidden and output layers

a given dataset. It is also, sometimes, referred as multilayered perceptron as it is made of layers of input, hidden and output units. A depiction of multilayered perceptron is provided in figure B.2. Whereas there is just one layer of input units and one layer of output units, number of hidden layers can be varied. There is no general theory on how many hidden layers can be incorporated for a given problem [109]. Usually, one selects number of hidden layers based on prior history of implementation on similar problems. In case of tomography, a single hidden layer has been found to yield a better solution [110]. Accordingly, we employ single hidden layer in our NN based filtered back projection.

The overarching goal behind the use of NN is to learn information about the system from the labeled data set and subsequently use the information to predict solution of unknown dataset. This idea is incorporated in the NN architecture with the aid of weights. In particular, we randomly assign weights between input-hidden layers and hidden-output layers. Then based on the labeled dataset we update the weights to properly replicate the behavior of the known data set. A detailed description on how we assign and update weight in NN is provided under the subsections below.

B.1.1 Forward Propagation

Forward propagation begins with assigning weights w_{hi} between input nodes, x_i, and hidden nodes, δ_h, and weights w_{kh} between hidden nodes and output nodes, o_k. The values
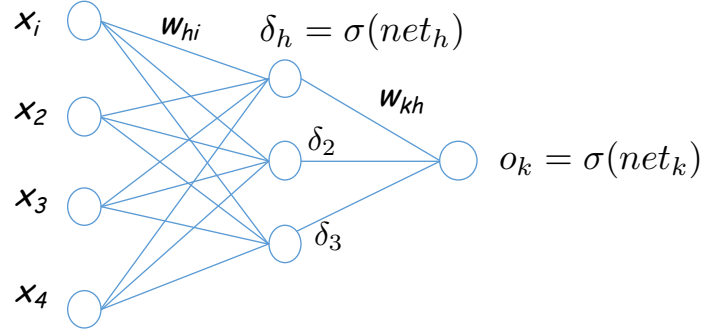
Figure B.3: A depiction of forward propagation of weights w_{hi} and w_{kh} from input to hidden and hidden to output layers respectively.

for the weights are initialized using random number generator in the range $(0.0, 0.5)$. Next, we determine net sum between the input units and their corresponding weights to each hidden unit. The net sum is transformed into output for each hidden unit using logistic sigmoid function as:

$$\delta_h = \sigma(\sum_i x_i w_{hi}) = \sigma(net_h), \tag{B.1}$$

where

$$\sigma(y) = \frac{1}{1 + e^{-y}}. \tag{B.2}$$

Similar calculations between hidden and output units yields:

$$o_k = \sigma(\sum_h \delta_h w_{kh}) = \sigma(net_k). \tag{B.3}$$

A schematic showing the forward propagation architecture is provided in figure B.3.

B.1.2 Error Backpropagation

In the backpropagation step, first we determine error between the network output and the expected output [103, 65]. Next, based on the error values the interconnected weights between the output-hidden layers and the hidden-input layers are adjusted.

In this study, we employ gradient descent approach to minimize sum-of-squared error function between the network output and the target values as:

$$E(\vec{w}) = \frac{1}{2} \sum_{k \epsilon outputs} (t_k - o_k)^2. \tag{B.4}$$

Here t_k is the target value and o_k is the network output for the training example k. Note that the weight w_{kh} can influence the rest of the network through net_k. Accordingly, the gradient of the error function in eq. B.4 with respect to w_{kh} can be written using chain rule as:

$$\begin{aligned} \frac{\partial E}{\partial w_{kh}} &= \frac{\partial E}{\partial net_k} \frac{\partial net_k}{\partial w_{kh}} \\ &= \frac{\partial E}{\partial net_k} \delta_{kh}. \end{aligned} \tag{B.5}$$

Likewise, net_k can influence the network only through o_k. Therefore, we can again use chain rule to write

$$\begin{aligned} \frac{\partial E}{\partial net_k} &= \frac{\partial E}{\partial o_k} \frac{\partial o_k}{\partial net_k} \\ &= -o_k(1 - o_k)(o_k - t_k) \\ &= e_k. \end{aligned} \tag{B.6}$$

Thus for each training example k, the weights in the outer layer can be updated as:

$$w_{kh} \leftarrow w_{kh} + \eta \frac{\partial E}{\partial w_{kh}}, \tag{B.7}$$

where η is the learning rate. It is usually chosen in the range $(0, 1)$. Substituting eqs. B.5 and B.6 in eq. B.7 we get

$$w_{kh} \leftarrow w_{kh} + \eta e_k \delta_{kh}. \tag{B.8}$$

Similarly, the strategy to deduce the update expression for w_{hi} begins by noting the fact that w_{hi} influences net_h, which then influence hidden unit δ_h and hence E. Accordingly, the gradient of error function with respect to net_h can easily be calculated to obtain:

$$\frac{\partial E}{\partial net_h} = o_h(1 - o_h) \sum w_{kh} e_k$$

$$= e_h. \tag{B.9}$$

Hence the update expression for w_{hi} can be written in the similar manner as eq. B.8 as:

$$w_{hi} \leftarrow w_{hi} + \eta e_h x_{hi}.$$

B.2   Neural Networks based Filtered Backprojection

After a brief excursion into describing the architecture of the neural networks, we now proceed to employ the technique for the tomographic reconstruction. We aim to use this technique to reconstruct electrostatic potential once it is fully robust. Our initial motivation to implement this method stems from the fact that we have a large repository of electrostatic phase data of nanoparticles with varying shapes. Accordingly, we want to check if and to what extent could we learn from the phase shift repository using the NN approach and subsequently, to what degree the learned information could be used to improve the FBP methodology.

In this initial testing stage of the NN approach for the tomographic reconstruction, we employ it to reconstruct 2D phantoms. If the implementation shows gain in reconstruction when directly compared to results from the conventional FBP approach, it will serve as proof-of-concept step. Subsequently, we can expand the model for 3D NN based FBP reconstruction.

Our NN based FBP implementation begins by formulating the training dataset. We use Shepp-Logan phantom [44] of different sizes while constructing the training dataset. These phantoms are generated using the *phantom* function in Matlab. Hence, ground truth will be known beforehand to perform error backpropagation procedure. Also, we use phantoms whose sizes are in close proximity to the one we seek to reconstruct. Here, we seek to reconstruct phantom 128. So, 14 different sized phantoms – Phantom 76 to Phantom 128 at a step size of 4 – are used to formulate the training set. A depiction of some of these phantoms is provided in figure B.4.

(a) Phantom 76

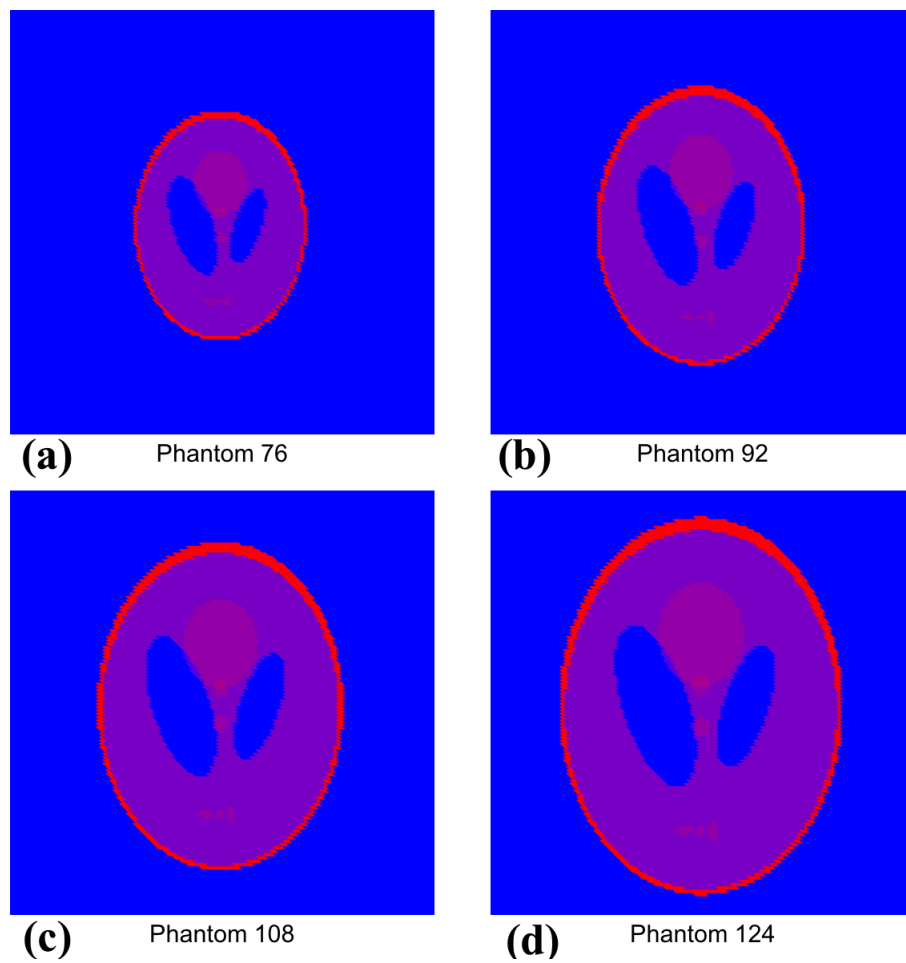**(b)** Phantom 92

(c) Phantom 108

(d) Phantom 124

Figure B.4: Shepp-logan Phantoms of varying sizes - (a) Phantom 76 (b) Phantom 92 (c) Phantom 108 (d) Phantom 124 - generated using Matlab function *phantom*. These phantoms have values in the range 0 (corresponding to blue) to 1 (corresponding to red).
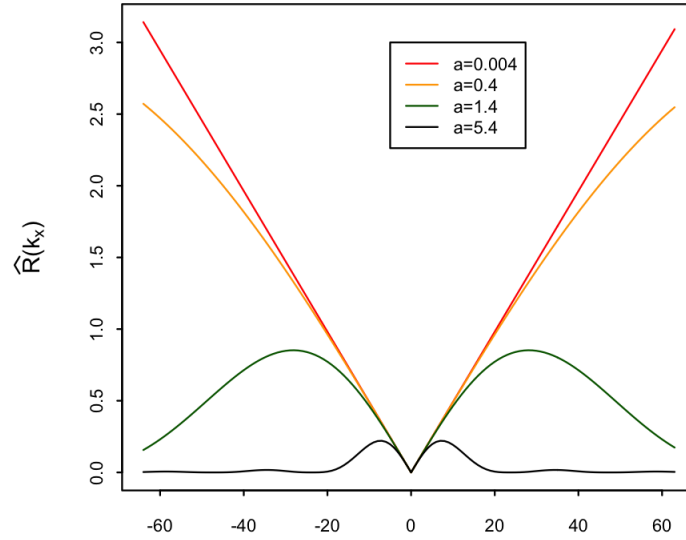
Figure B.5: An illustration of sinc filters corresponding to different cutoff frequency, a.

Next, sinogram measurements are obtained by forward projecting the 14 phantoms as described in section 3.1.1. Projections are determined at a step-size of $3°$ for angles ranging from $1°$ to $180°$. Then the FBP methodology is employed to reconstruct the phantoms. Here, we use sinc-filter as our filtering function which can be mathematically expressed as [112]:

$$\hat{R}(k_x) = \left| \frac{1}{a} \sin \left(\frac{ak_x}{2} \right) \right| \left(\text{sinc} \left(\frac{ak_x}{2} \right) \right)^2.$$

In addition, we employ the FBP approach making use of different cutoff frequency - $[0.004, 0.04, 0.4, 1.4, 2.4, 3.4, 4.4, 5.4]$ - in the filtering domain to facilitate the NN to learn weights that promote a reconstruction that is clean as well as highly resolved. An illustration of sinc-filter for different cutoff frequency is provided in figure B.5. Likewise, figure B.6 provides a depiction of the FBP results obtained using varying degree of cutoff frequency to yield reconstructions ranging from sharp to smooth resolutions.

Overall, convolution of sinogram - determined from the phantom, $\mathbf{X}$, - with a range of sinc-filters, $R_1, R_2 \ldots, R_m$, generate training files, $\mathbf{X}_1, \ldots, \mathbf{X}_m$. A schematic of this procedure is illustrated in figure B.7. To be specific, we begin with 14 different phantoms that are forward projected and subsequently, each sinogram is back projected using 8
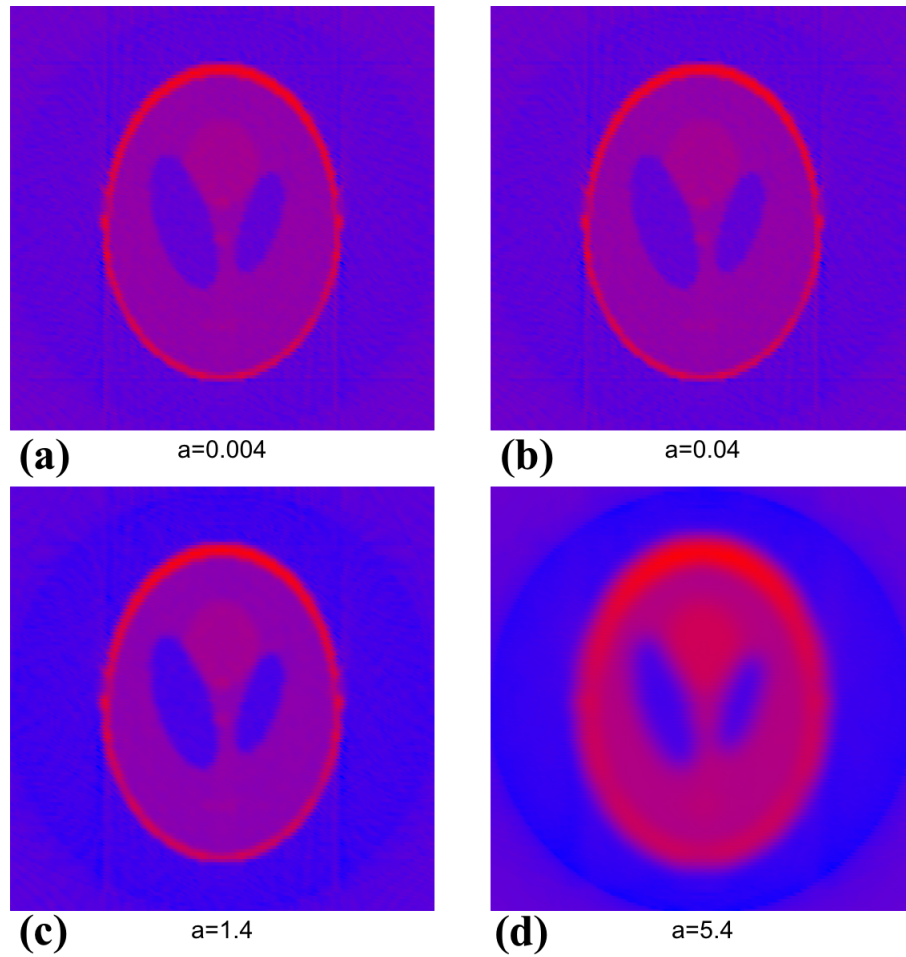
Figure B.6: FBP reconstructions obtained using sinc-filter with cutoff frequency (a) $a = 0.004$ (highly sharp) (b) $a = 0.04$ (c) $a = 1.4$ (d) $a = 5.4$ (highly smooth).
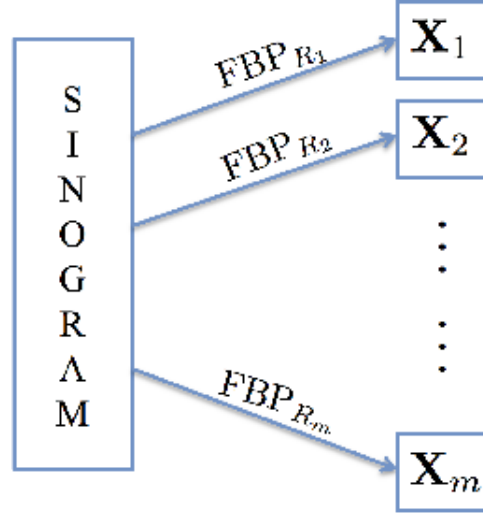
Figure B.7: An illustration data acquisition step for training .

different cutoff frequency. Consequently, we generate 112 images for the training dataset.

Each FBP based reconstruction is treated as input unit, $\mathbf{X}_i$. Further, we incorporate 8 hidden units and learning rate, η, is set as 0.1. The forward propagation and the error backpropagation steps are repeated for 500 iterations to train the weights - w_{hi} and w_{kh}. Thus trained weights are used to forward propagate regular FBP phantom 128 and consequently, we obtain NN based FBP (NN-FBP) result. Figure B.8 shows the NN based FBP result along with the results from the BP and the FBP approaches.

A thorough review of figure B.8 reveals that the NN-FBP yields the best result when compared to its counterparts from the BP and the FBP approaches. In particular, we see that the BP result is plagued by lots of white noise and the FBP result shows ring artifacts and coarseness inside the phantom. Such reconstruction flaws are ameliorated to a considerable degree in the NN-FBP result. Also, the NN-FBP result demonstrates a higher spatial resolution compared to the results from the BP method and the FBP method. Quantitative analysis by means of root mean squared error (RMSE), too, reflects the gain in reconstruction having used the NN-FBP approach. More precisely, the RMSE value reduces to about 0.105 (for the NN-FBP result) from 0.213 (for FBP result).

On the whole, this appendix elucidates a framework to employ neural networks to supplement the filtered backprojection method. We used 2D Shepp-Logan phantom to

(a) BP

(b) FBP
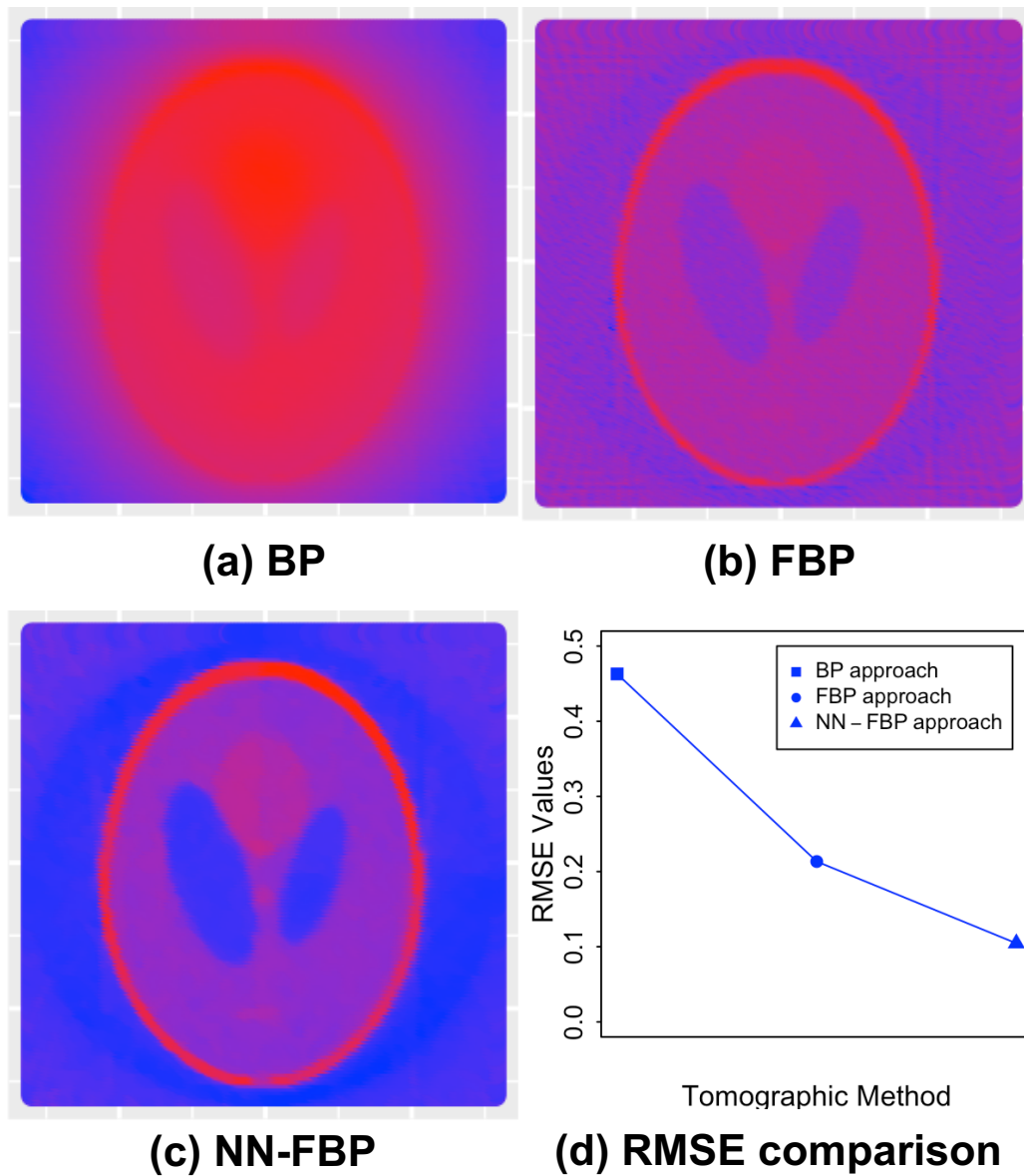
(c) NN-FBP

(d) RMSE comparison

Figure B.8: Illustration of reconstruction from different tomographic methods - (a) Back Projection (BP); (b) Filtered Back Projection (FBP); (c) Neural Networks Based Filtered Back Projection (NN-FBP). The bottom left plot, (d), depicts root mean squared error (RMSE) analysis of the tomographic methods.

develop a training dataset and subsequently, trained weights were used while reconstructing an unknown phantom. We found qualitative and quantitative gain in reconstruction having used the NN-FBP approach instead of a mere filter based FBP approach. Thereby, providing us with a concrete evidence that Neural Networks based Filter back projection can be used to learn information about target density from a set of measurements deduced from relevant geometry or shapes. Hence, it will be a sagacious decision to explore the use NN-FBP for electrostatic potential reconstruction in the future.